SLAC-106
UC-28
(EXPI.)

40-INCH HYDROGEN BUBBLE CHAMBER CONVERSION TO 70 KILOGAUSS SUPERCONDUCTING MAGNET

PROPOSAL III

JOHN ALCORN, JOSEPH BALLAM, RICHARD BLUMBERG,
HABIBO BRECHNA, HENNING PETERSEN, ARTHUR ROGERS,
STEVEN ST. LORANT, KNUT SKARPAAS, BOHDAN SUKIENNICKI

STANFORD LINEAR ACCELERATOR CENTER
STANFORD UNIVERSITY
Stanford, California

PREPARED FOR THE U.S. ATOMIC ENERGY
COMMISSION UNDER CONTRACT NO. AT(04-3)-515

September 1969

Reproduced in the USA. Available from the Clearinghouse for Federal Scientific and Technical Information, Springfield, Virginia 22151.
Price: Full size copy $3.00; microfiche copy $.65.

TABLE OF CONTENTS

LIST OF FIGURES

I. INTRODUCTION

We propose an extensive modification of the SLAC 40-inch bubble chamber magnet to provide it with 70 kilogauss magnetic field and an improved optical system. It is believed that this combination can lead to the most accurate bubble chamber yet built. Furthermore, this chamber placed at SLAC, where operation at two pulses per second while using only 1-2% of the beam is now routine, can be used for experiments that demand both statistics and resolution.

The recent history of strong interaction physics in bubble chambers where the incoming particle has energy $\gtrsim$ 6 GeV and the final state involves $\geq$ 3 bodies reveals the pressing need for such a detector, e.g., the lack of good data in the A and Q regions of pion and kaon boson resonances. There are also theoretical ideas, such as those of Gell-Mann and Zweig that predict fine structure and resonance splitting. Furthermore, there still remains the job of hyperon resonance analysis of a type that is now well started for the nucleons.

Two other features of the proposed high field chamber should also be mentioned, both leading to unique physics. The first is the possibility of doing reasonably accurate experiments with a visible hydrogen volume placed inside a neon-hydrogen mixture of high neon concentration (> 80%). This allows a detailed study of reactions involving two π^o's, a neutron and a π^o, and neutral decay modes of strange particles, where the initial interaction is guaranteed to take place with a proton. The second feature is a by-product of the restructuring of the chamber which allows for trigger and timing counters to be placed inside and outside the hydrogen volume for both time-of-flight and light triggering information. Thus, it is possible to consider experiments with counter-triggered lights involving, for example, 10 million expansions and several hundred thousand photographs.

In summary the new chamber will provide the following for events produced by incoming energies $\leq$ 12 GeV:

(a) Mass resolution of $\Delta m = \pm$ 1-2 MeV for four constraint events with effective masses $\leq$ 2 GeV.

(b) Mass resolution of $\Delta m \pm$ 3-5 MeV for one constraint events with effective masses $\leq$ 2 GeV.

(c) Mass resolution of $\Delta m = \pm$ 10 MeV for 2 π^o events produced in hydrogen and observed in neon. Observation efficiency ~65%.

(d) Mass resolution of $\Delta m = \pm$ 5 MeV for 1 π^o + neutron events produced in hydrogen and observed in neon. Observation efficiency ~65%.

(e) Trapped secondaries - particles of momentum $\leq$ 800 MeV/c have a very good chance of being trapped in the chamber, allowing a clean separation among $e^{\pm}$, $\mu^{\pm}$, $\pi^{\pm}$ and $K^{\pm}$ when they appear as decay particles.

(f) Measurement of magnetic moment of hyperons.

These points are further discussed in Section II.

The rapid developments in the past few years, resulting in stabilized superconducting wire being available from a relatively large number of commercial sources, put the proposed high field in the realm of practical possibility. The fact that the present coil configuration of the 40" chamber is circular makes the estimation of mechanical forces more straightforward. The required optical precision and accuracy of control of chamber conditions are improvements on an existing chamber whose performance is already of high quality.

Although the proposed work is, as already stated, extensive, much of the present chamber system can be retained. This includes the magnet steel, chamber glass, various support and clamping rings, instrumentation, vacuum system, camera, cryogenic controls, hydrogen refrigerator, expansion system, magnet separation and support system, building, crane, and control room.

New components are the superconducting coils and dewar, a helium refrigerator, a new vacuum tank, a new chamber body with a larger beam exit window, a non-conducting piston and, possibly a non-conducting omega bellows. Drawings of the proposed design are shown in Figs. 1.1 through 1.5.

Part of this proposal involves a re-examination of the optics of the chamber-glass-camera system with the aim of reducing the optical distortion errors to a level commensurate with the errors introduced by the best measuring apparatus now available. This is a very important point because the salient argument for this conversion is an order of magnitude increase in mass resolution over the present chamber. The only way to achieve this is by a combination of increased magnetic field and better optics. The camera lenses and chamber fiducials will be considered as an optical system as described in Section VIII.

The cost of the project is estimated at 1.7 million dollars, the bulk of which is in the coil and refrigeration system. Cost details are shown in Table X.1

The modified chamber would also be ready to extend the present experimental program when the accelerator increases its energy by exchanging more efficient klystrons for the ones now in use. This would affect the K_2^o and annihilation gamma experiments linearly so that these will go up from 7 GeV/c to 9 GeV/c and from 7.5 to 10 GeV, respectively. The additional field will more than compensate for the increase and will make continuation experiments at the new energies even more accurate than the old ones. There is also the non-trivial point of advance of the art. Such a chamber could serve as a prototype for larger precision chambers that could be used at NAL. For example, a similar chamber, 3 meters in length, would do excellent physics in beams up to 40 GeV/c in momentum, including delineation of events with one, two, and three neutrals, as well as the radiative decays of some of the higher resonances. The same considerations apply to SLAC, should this laboratory go to 50-100 GeV electron energies.

For the reasons expressed in this introduction, as well as others that are detailed in Section II, it is felt that the high field improvement of the SLAC 40" bubble chamber would be a highly productive and imaginatively useful advance in the bubble chamber technique at this laboratory. The proposed expenditure is quite moderate and the time scale is short enough to realize the anticipated results.

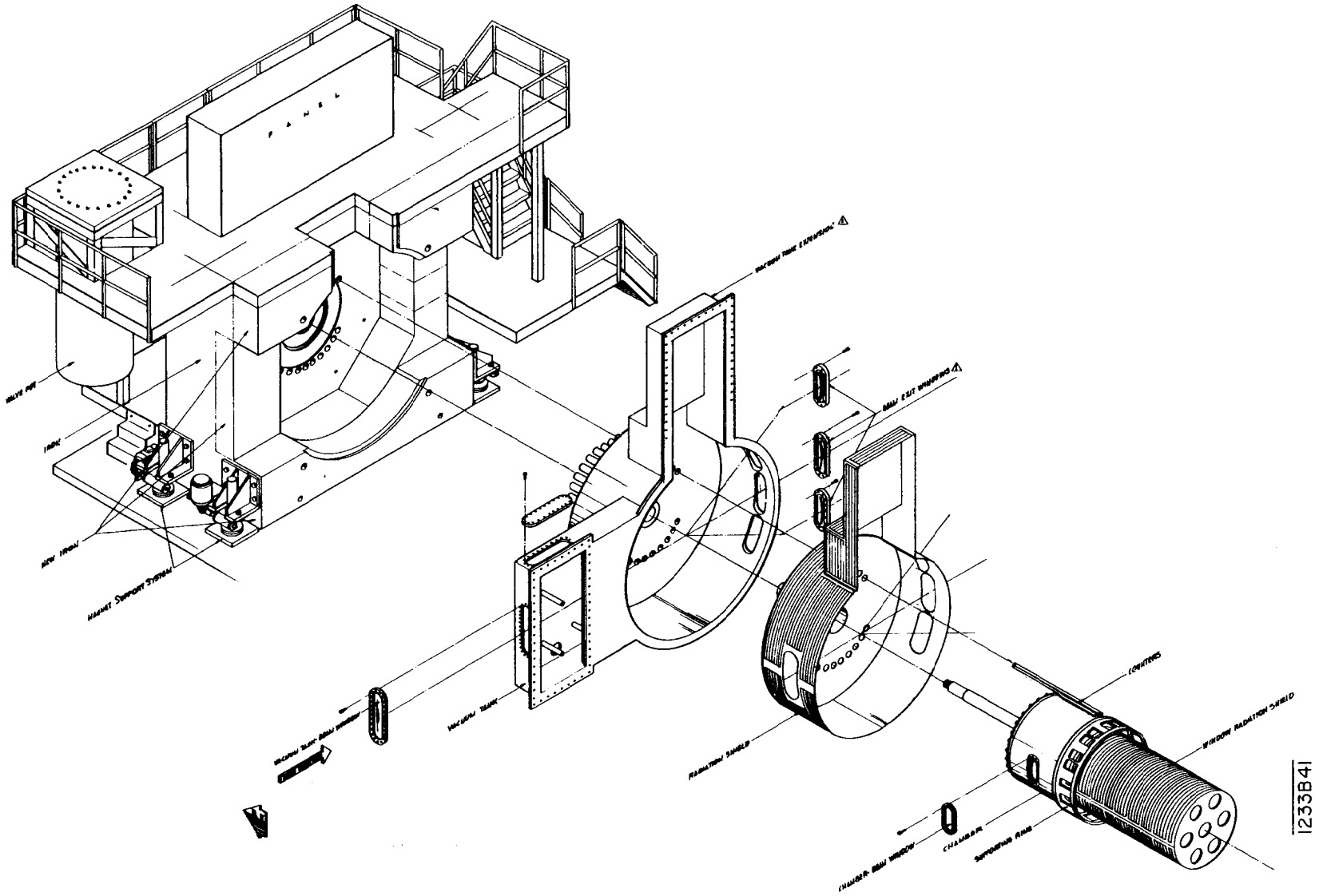

FIG. 1.1--Isometric, expansion end.

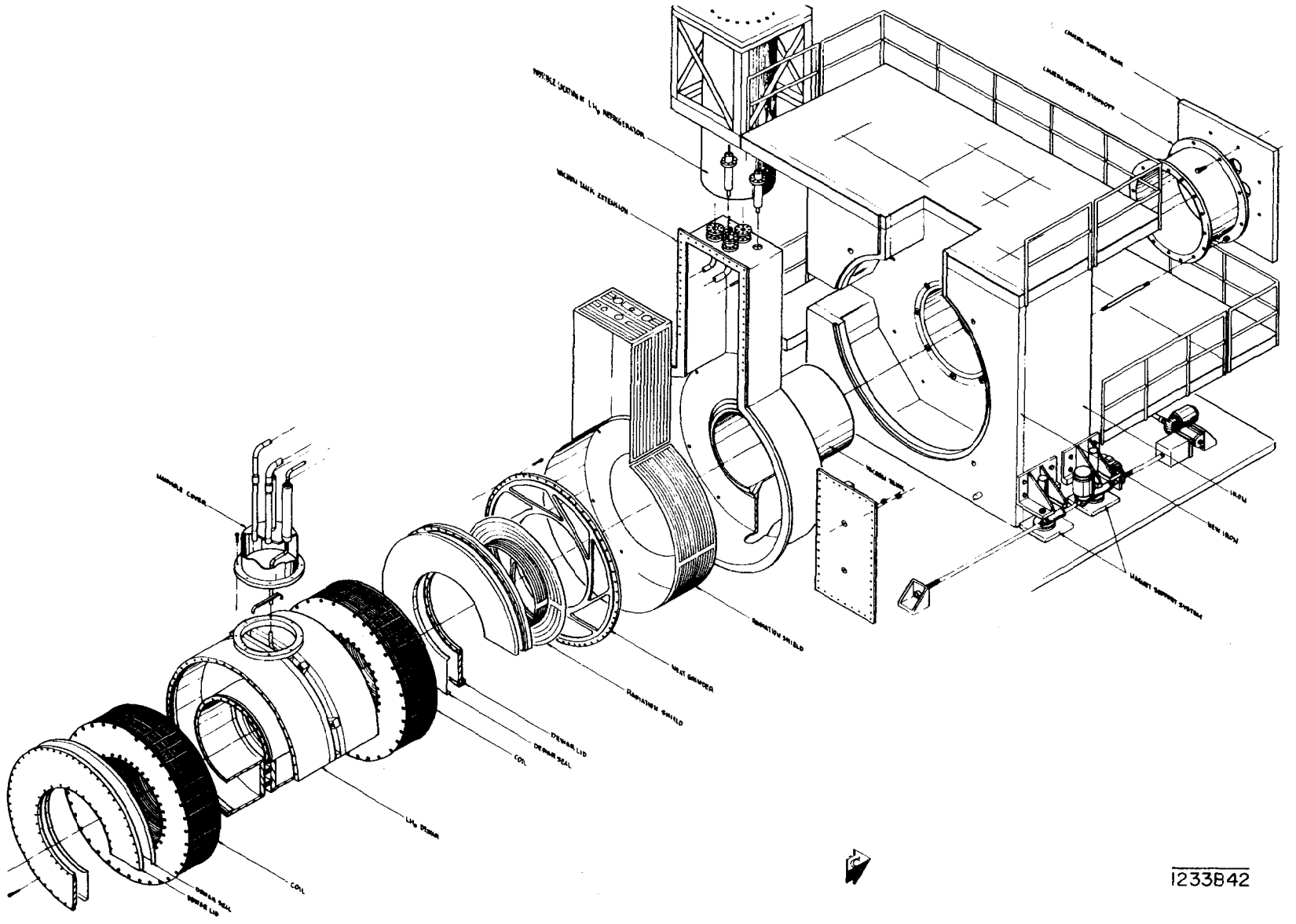

FIG. 1.2--Isometric, camera end.

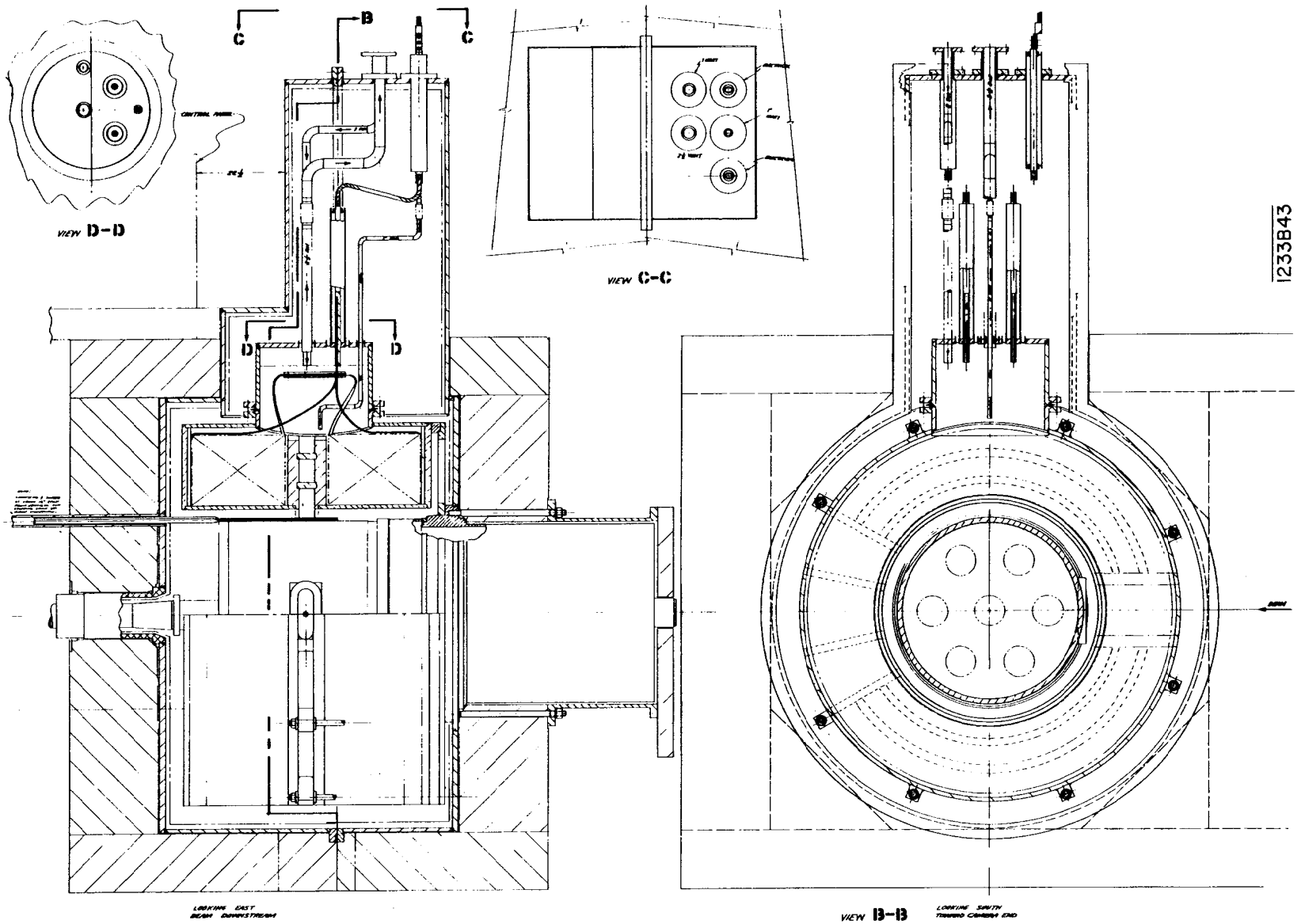

FIG. 1.3--Elevation sections – transverse and camera end.

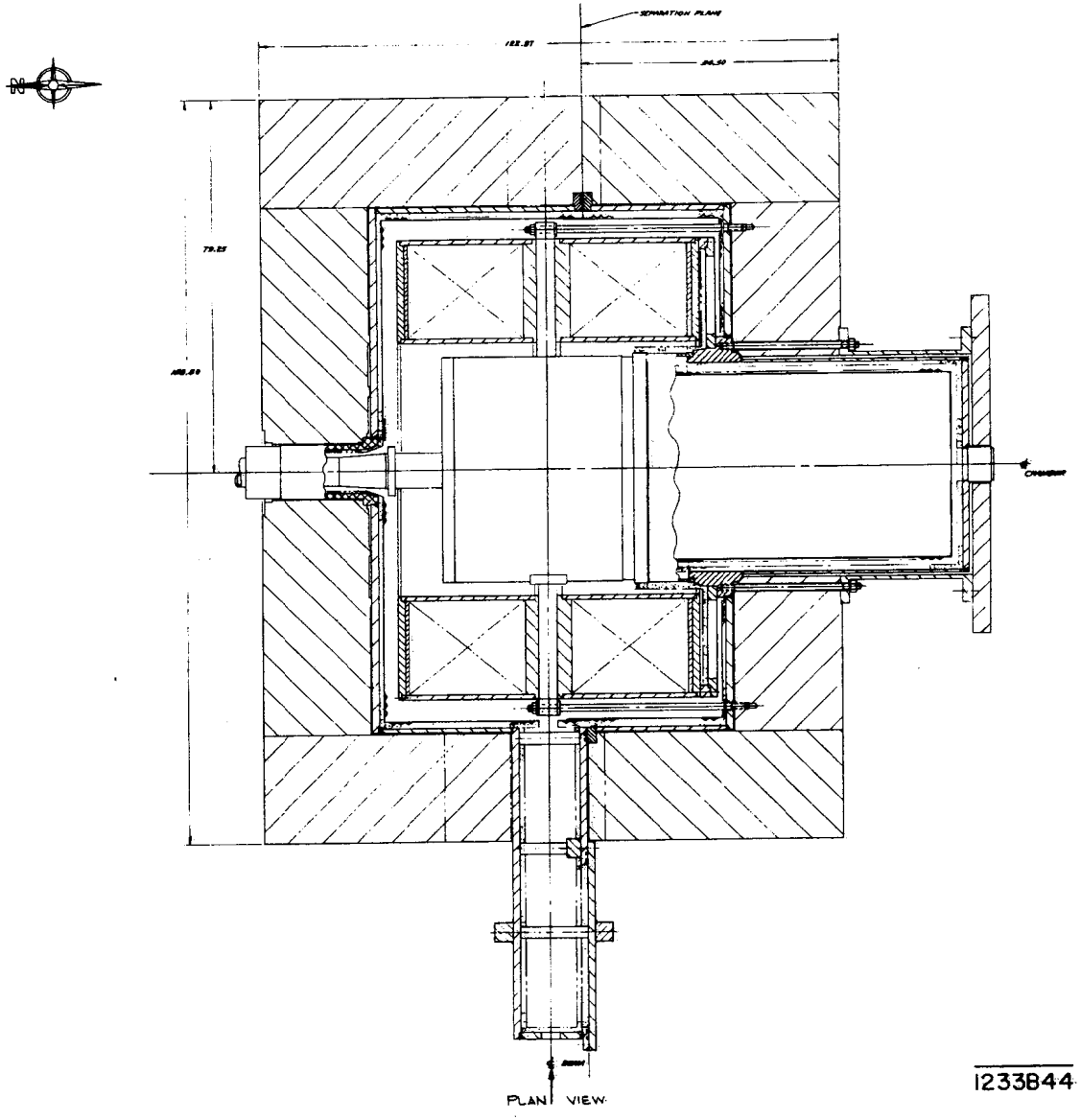

FIG. 1.4--Plan view section.

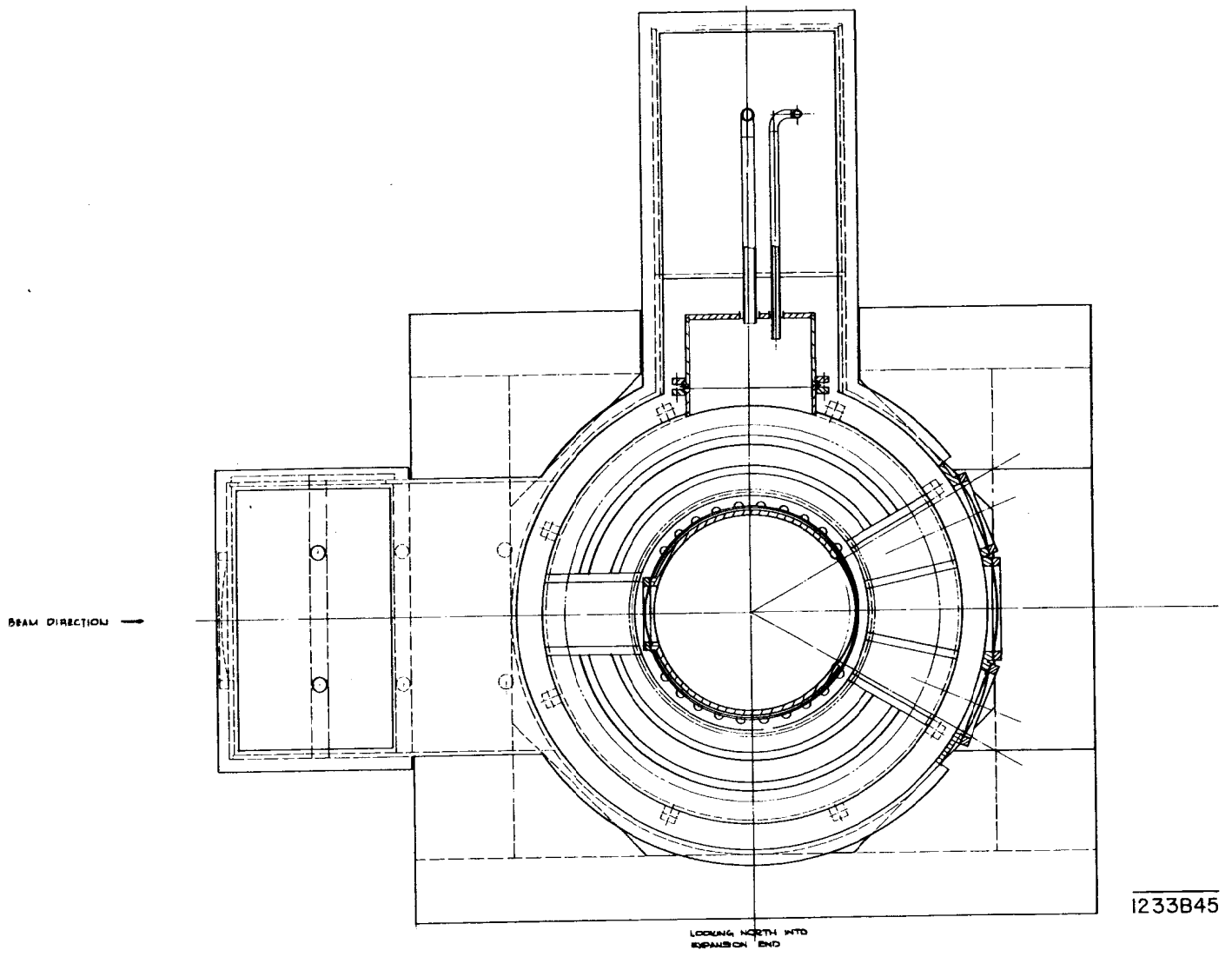

FIG. 1.5--Elevation section – expansion end.

II. PHYSICS ASPECTS

A. 70-kG Magnetic Field, 40-Inch Hydrogen Chamber

1. Increase in Measurement Precision

The total error on a bubble chamber track may be decomposed into contributions from the momentum and angle measurements. The momentum error has two parts, namely,

$$\left(\frac{\Delta p}{p}\right)^2_{\text{total}} = \left(\frac{\Delta p}{p}\right)^2_{\text{coulomb}} + \left(\frac{\Delta p}{p}\right)^2_{\text{measurement}} \qquad \text{(A.1)}$$

For hydrogen specific formulae* for each part can be expressed as[1]:

$$\left(\frac{\Delta p}{p}\right)^2_{\text{measurement}} = \frac{1.44 \cdot p^2 \epsilon^2 \cdot 10^{-4}}{H^2 L^5 \cos^3\lambda} + \frac{1.2 \cdot 10^{-5} \epsilon^2 \sin^2\lambda}{L^2 \cos\lambda} \qquad \text{(A.2)}$$

$$\left(\frac{\Delta p}{p}\right)_{\text{coulomb}} = \frac{.133\left(\ell n 4.8 \cdot p + \ell n 145 \cdot \frac{p}{MC}\right)}{H^2 L \beta^2 \cos^2\lambda} + \frac{5.0 \cdot 10^{-2} \cdot L \cdot \tan^2\lambda}{p^2 \beta^2} \qquad \text{(A.3)}$$

where

λ = dip angle in radians

L = total track length in centimeters

H = magnetic field in kilogauss

p = momentum in MeV/c

β = P/E

E = energy in MeV

M = rest mass of particle in MeV/c^2

ϵ = positional error in chamber space of the measuring device, in microns

For relatively small λ, the second terms in Eq. (A.2) and (A.3) may be neglected. The angle errors in terms of θ (track angle projected onto the front glass) and λ

*The general analysis given follows directly that of reference 1, p. 34.

(already defined) are:

$$\langle \Delta\theta \rangle^2 = \frac{3.7 \cdot 10^{-2} L}{p^2 \beta^2 \cos^2 \lambda} + \frac{3.8 \cdot 10^{-6} \cdot \epsilon^2}{L^3 \cos^3 \lambda} \qquad (A.4)$$

$$\langle \Delta\lambda \rangle^2 = \frac{1.2 \cdot 10^{-5} \cdot \epsilon^2 \cos \lambda}{L^3} + \frac{5 \cdot 10^{-2} \cdot L}{p^2 \beta^2} \qquad (A.5)$$

Typical values of ϵ for automatic measuring machines such as HPD's (Hough-Powell) are 25 microns. The dependence of the error in momentum on the momentum itself, taking the track length L fixed at 60 cm, is shown in Fig. 2.1 for various values of H and ϵ. This is appropriate to our discussion since the 40-inch chamber should have typical track lengths of 45-75 cm for high energy tracks. Clearly a setting error (ϵ) of 50-100 microns is sufficient at 70 kG to make the measurement component negligible for momenta up to 5 GeV/c^2.

Figures 2.2 and 2.3 give the functional dependence of the angular errors on track length for various momenta. They indicate that a measureable track length of 45-75 cm is more than enough to minimize the angular errors. All that remains is to minimize the Coulomb portion of the momentum error, which has the form $\frac{\Delta p}{p} \simeq \frac{1.6}{H\sqrt{L}} \simeq \frac{23\%}{H}$ for L = 50 cm. Certainly the higher the magnetic field, the smaller this Coulomb term will become; but it is sufficient to reduce it to the same magnitude as the total angular contribution, since further reduction yields diminishing returns. Unfortunately, the relative import of momentum vs angular errors depends on the mass of the resonance, its momentum, its decay products, and even the angular distribution of the decay. For a simple case of obvious interest, we consider resonances in the mass range 700-1500 MeV, which have two-body decays, and are produced with momenta in the range 0.5-5.0 GeV/c (Figs. 2.4 and 2.5). These require a magnetic field of 50-70 kG to optimize the mass error, which then has an unfitted value of 2.0-4.0 MeV. One may further

generalize and say that for resonances whose decay products have momenta of 2 GeV/c or less, the error on the mass is inversely proportional to the magnetic field. Thus 70 kG in such cases will give roughly one-third the mass error one gets from 26 kG. Under these conditions, the improvement in the missing mass spectrum is also striking (Fig. 2.6). Since the (missing mass)^2 error is small compared with $m^2_{\pi^o}$, this permits a nearly exact separation of the events with one missing π^o, γ, K^o, or neutron from each other and from events containing two or more missing neutrals.

Here it is worth noting that for tracks with momenta significantly higher than 2 GeV/c, the mass error is almost totally due to angular contributions. Although for such cases the 70-kG field represents a smaller fractional improvement on the mass error, this improvement may considerably extend the energy range of many experiments. For example, Figs. 2.7, 2.8, 2.9, and 2.10 show the effects of different beam energies (8 and 12 GeV/c) and magnetic fields (20 and 70 kG) on the analysis of events of the type $\gamma + p \longrightarrow \omega + p \longrightarrow \pi^+ + \pi^- + \pi^o + p$.[3] Here we see that the analysis power at 8 GeV/c and 20 kG is acceptable. For the same beam energy, the 70-kG field is a marked improvement. The important thing to note, however, is that at 12 GeV/c, this type of one-constraint physics becomes virtually impossible with a 20-kG field, whereas 70 kG and 12 GeV/c are roughly equivalent in resolution to 20 kG and 8 GeV/c. Thus for events in this class, a 70-kG field will extend the energy range from 8 GeV/c to 12 GeV/c.

2. Proposed Experiments

A system which will resolve resonances with a fitted error of 1-3 MeV, which we can safely expect with a 70-kG field, has the following experimental advantages:

(a) better identification of events with one missing neutral (one-constraint fits)

(b) identification by capture of secondaries

(c) opportunity of observing resonances too narrow (and too weak) to be resolved with present chambers

(d) improved resolution of fine structure in existing resonances, and

(e) measurement of magnetic moments.

The following experiments are presented for illustrative purposes with the understanding that current problems in strong interaction physics may or may not still be of interest two years hence. To our best judgment the same kinds of problems will still be very much in evidence however.

(1) An important area of investigation made possible by greater mass resolution is the search for new resonances. At present there are no fewer than 14 accepted and four disputed nonstrange mesons in the mass interval 700-1500 MeV alone. Eight of these (accepted) have widths of the order of 100 MeV. Thus a resonance which is weakly produced or which has only a small fraction of decays into detectable charged tracks might easily be obscured by the tails of more prominent neighbors. Also a narrow resonance will be spread to such a degree by present resolving power as to be lost completely or smeared with others into one peak. To quote from a theoretical paper by Mitra and Ross[5]: "At present, the sensitivity of experiments is such that many of the resonances will be unobserved. Many states have very small width and/or high inelasticity or are very broad, such that they may not be observed for some time." We have every reason, from a theoretical standpoint, to expect several new resonances in precisely this region. In particular, the quark model[6] requires three or four in its simplest form, and a dozen or so in some of the newer modifications. The success or failure of such theories depends directly on finding these resonances. There are two ways in which the proposed magnet will facilitate this search. First, the increased resolution will make possible accurate binning of 5 MeV or less on

the spectrum of resonant masses. Such sharp definition should be sufficient to locate new narrow resonances, as well as better resolving three already established: the X^o, ϕ, and $\delta(965, T = 1)$, which have widths of < 4 MeV, $3.4 \pm .8$ MeV, and < 5 MeV, respectively. Second, the ability to separate states with one missing neutral from those missing two or more, and a missing-mass resolution of $\Delta m <$ 10 MeV should allow detection of decay channels in both broad and narrow resonances which were previously lost. For example the η^o decays 75% into neutrals. As a final point, merely detecting a $\pi^{\pm}\pi^o$ decay of the δ in a bubble chamber experiment has numerous practical (as well as the obvious theoretical) advantages. At present, the $\pi^+\pi^-$ decay mode of the K_s^o and the $\pi^+\pi^-\pi^o$ decay of the ω^o are used as "calibration standards" to determine experimental resolution and systematic errors or biases. Unfortunately, there is no narrow resonance presently available which decays into $\pi^{\pm}\pi^o$. It is possible that the δ^o may fill this gap.

(2) It is now reasonably well established[6-8] that the A_2 peak is split, with a gap of some 30 MeV right in the center. The experiment of Chikovani et al.[7] used a missing mass spectrometer to study the interaction $\pi^- p \longrightarrow pA_2^-$. Their (full width) experimental mass resolution was 16 ± 3 MeV, but owing to the enormous statistics (4000 events), they were able to bin their data in 5 MeV intervals. The fitted width of the hole was found to be 30 ± 3 MeV. Assuming the A_2 to be one peak, two independent peaks or a "dipole" (interference) gave fits with probabilities of .1%, 15%, and 70% respectively. Commenting on this experiment, Lassila and Ruuskanen[10] suggested several theoretical explanations of relatively far-reaching significance, namely that this could be another resonance with the same quantum numbers as the A_2, which, within the quark system, may require invoking four quark ($\bar{q}\bar{q}qq$) meson states, and if so the Regge trajectory classifications may have to be modified. Furthermore Harari[6] has pointed out that if the A_2 is split,

symmetry arguments would predict that the K** (1420) should also be split. To resolve the numerous theoretical possibilities will require an experiment which can measure the masses of the A_2^+, A_2^o, and A_2^- (all three could be different!) for different decay modes to an accuracy of 5 MeV binning. This clearly requires a bubble chamber. The experiment of Crennell et al.,[9] however, points out the difficulties of attempting such a measurement without inherently better resolution. By studying events of the class $\pi^- p \longrightarrow p\pi^-$ + (MM) where the proton stops, they were able to reduce the experimental (full width) error on the M(π^-MM) to about 10 MeV. From this spectrum, they observed that the A_2 is split: $A_2^L = 1269 \pm 5$, $A_2^H = 1315 \pm 5$. Then an investigation of the $K_1^o K_1^o$ spectrum ($T_{exp} \simeq 5$ MeV, from $\pi^- p \longrightarrow n K_1^o K_1^o$) showed only one peak, at 1311 ± 5 MeV. This led them to conclude that the $K_1^o K_1^o$ is the decay of the A_2^H, and that A_2^L and A_2^H are separate resonances with different quantum numbers. Now, the problems with this experiment are numerous:

a) Requiring a stopping proton introduces a T-cut into the charged A_2 sample, which can have various effects — including biasing the mass. This cut was not applied to the neutral $A_2 \longrightarrow K_1^o K_1^o$ sample.

b) The T-cut reduced the statistics so that the 10-MeV binning results in an average of 7-8 A_2's in each of the eight bins of the A_2 region. Consequently their 2-peak fit is not significantly better than a 1-peak fit to this area.

c) What is needed is a comparison of different decay modes for the charged A_2, or the neutral A_2. Comparing the spectrum of $A_2^- \longrightarrow \pi^-$ + (MM) with that of $A_2^o \longrightarrow K_1^o K_1^o$ is rather weak, since there may easily be 10 MeV or more mass difference between A_2^- and A_2^o. Unfortunately, the selection on stopping protons made it impossible to observe the

neutral equivalent of $A_2^- \longrightarrow \pi^- + (MM)$, and the limited number of $pK^-K_1^o$ events keeps one from using the charged equivalent of $A_2^o \rightarrow K_1^oK_1^o$.

d) In the end, the question is still open as to whether the $K_1^oK_1^o$ resonance coincides with A_2^H or the central gap. They admit that interference fits are better than 2-peak fits, though again there is the question of statistical significance of the fits. The fact that the $K_1^oK_1^o$ is separated from the hole in the charged distribution by 14 ± 8 MeV is hardly conclusive, especially since the neutral and charged distributions may be shifted by this amount with respect to each other.

This list of faults should not be construed as an attack on the experiment of Crennell et al. — with present chambers, this is no better way to get the required resolution, and this is the price one has to pay.

(3) With a 70-kG field, events with one missing neutral (n, π^o, γ, and K_2^o) can be analyzed for resonances with a $\Delta m_{res} \simeq 8$ MeV (one-constraint fit). Furthermore, events with "missing mass" (two or more neutrals) will have an error in the "missing mass," $\Delta m < 10$ MeV. This analyzing power is sufficient to resolve any given set of charged final states from that set plus a missing π^o, as well as distinguishing most final states with two missing neutrals, one of which is a K^o (e.g., $\Sigma^+\pi^+K^o$ vs $\Sigma^+\pi^+K^o\pi^o$, where the K^o escapes). It would also accurately separate Λ^o from Σ^o events. These ambiguities have introduced uncertainties and bias into a broad spectrum of measurements which could be resolved if the experiments were performed with the expected improvement in resolution.

(4) Present bubble chamber studies of leptonic decays are severely limited by the difficulties in identifying such decays against a background of nonleptonic decays which are usually 10^3 times more frequent. This is especially true in

hyperon decays, and requires drastic cuts in the decay spectrum. Courant et al.,[4] studying Σ^- decays, found that electrons could only be identified below 60 MeV/c, making only 10% of the $ne^-\nu$ spectrum accessible. Similarly, the requirement that μ's stop in the chamber (to distinguish them from pions) limited their study to 15% of the $n\mu^-\nu$ events.

Investigations of K_2^0 decay modes, electromagnetic decays (e.g., $\eta \longrightarrow \pi e^+e^-$, or η, η', $X^0 \longrightarrow e^+e^-\gamma$ for pion resonances, and $\Sigma^+ \longrightarrow pe^+e^-$, $\Xi^- \longrightarrow \Sigma^- e^+e^-$, etc., for baryon resonances), and $\Delta Q \neq \Delta S$ decays have all encountered similar difficulties. These problems would be solved by the proposed increase in magnetic field, which would trap decay secondaries with momenta up to 800 MeV/c. This would permit unique identification over the entire spectrum for decays mentioned above, as well as polarized hyperons produced by K^- and π^- beams of selected momenta.

(5) Finally we consider a class of experiments peripheral to usual bubble chamber measurements — the determination of hyperon magnetic moments. Given a 40-inch chamber in a 70-kG field, a half-million picture exposure with 15 beam tracks per picture of 390 MeV/c K^- particles should resolve the μ_{Σ^+} and μ_{Λ^0} to $\pm$ .07 nuclear magnetons.[1] Similarly, the same exposure with a 2 GeV/c K^- beam should measure μ_{Ξ^-} to an accuracy of $\pm$ .7 nuclear magnetons. At present, the μ_{Ξ^-} is unmeasured; μ_{Σ^+} and μ_{Λ^0} are measured at 2.4 $\pm$ .6 nm and -.73 $\pm$ .16 nm, respectively. An accurate knowledge of these moments is of great theoretical importance in distinguishing various models: for example, pure SU(6) predicts 2.79, -.93, and -.93 nm for μ_{Σ^+}, μ_{Λ^0}, and μ_{Ξ^-} respectively whereas the theory of Beg and Pais predicts 2.20, -0.78 and -.66 nm respectively. A measurement of the accuracy indicated above for the 70-kG chamber could easily resolve these two models. Although a hydrogen bubble chamber is not ideally suited for this

work, the absence of geometric biases and other systematic errors inherent in the usual measurements makes it strongly competitive at 70 kG.

B. Installation of Counters Around the Chamber Body

1. Introduction

Counter control of hydrogen bubble chambers is one of the major developments in the HBC field. The main disadvantage of present systems is the small solid angle accepted by the counters. In general, the presence and geometry of the field magnet makes improvement of this situation rather difficult.

We are currently installing a very large acceptance hodoscopy counter system on the SLAC 40" HBC.[17] To overcome the problem of solid angle, the counters are being mounted around the outside wall of the liquid hydrogen chamber and inside the vacuum chamber. Light from the scintillators is then piped to the photomultiplier tubes in a low field region. This system will allow counter control of the HBC flash, better identification of event topology, determination of particle momenta via time-of-flight measurement, and detection of the presence of π^0's by the materialization of the decay photons in the hydrogen chamber body. For best efficiency the present magnet geometry needs modification.

The construction of a new magnet will make it possible to "build in" a far more elaborate and complete counter array (a proposed system shown in Fig. 2.11) than could be achieved by modifying the present magnet. Furthermore, for historical reasons, the present chamber has an entrance window of 26" × 7" in size and an exit window 8" in diameter. The new chamber can be made with a larger exit window in order to allow further triggering by counters and/or hodoscopes placed directly behind the chamber. For certain peripheral types of reactions with fast forward particles, this represents a distinct advantage over our present arrangement.

2. Physics Information

We consider the utility of the proposed fine mesh counter hodoscope in several different applications:

(1) Time-of-flight. In experiments with neutral beams (e.g., neutron, K_2^o), the counter hodoscope may be used to measure the flight time of the beam particle from the production target to its interaction in the HBC. For beam energies up to 3.5 BeV/c for K^o's and 7 BeV/c for neutrons, this measure of the incident momentum is accurate enough to be used in the kinematic fitting process — which would allow final states with one missing neutral particle to be identified.

(2) Event selection. The scintillation counter signals can be used in a fast logic system to determine the event topology and decide whether to take the photograph. Thus pictures could be limited to a specified event configuration. This would allow bubble chamber experiments to more efficiently study interactions which occur infrequently, reducing the scanning time and waste of film.

(3) Missing neutral identification. During analysis of the film, information from the counters may be used to extract events with multiple neutrals, which could then be separately processed. Such events would be identified by multiple counter firing within the event gate, but no visible charged particles observed going towards the triggered counters in the picture. Since over half of the cross section at energies in excess of 5 BeV/c result in final states with multiple neutrals, such a facility would greatly reduce computer analysis time, the number of ambiguous events, and increase the yield of analyzable events.

(4) Control of measuring machines. When automatic measuring machines become a reality, the counter tape may be used to guide the machine in selecting frames containing events of a desired type. Also the counter coordinates may be used as a starting point for each track, in a tracking/filtering mode. This use is likely to be more important in coming years.

C. 70 kG-Magnetic Field, Hydrogen Target, Neon-Hydrogen Mixture in Chamber

1. Detection of π^o's

By filling the 40-inch chamber with a mixture of neon and hydrogen which is approximately 90% neon by volume, we can realize a radiation length of one-third of a meter. This, coupled with a liquid hydrogen target occupying roughly the initial third of the chamber,[11] would result in an average distance of two radiation lengths for conversion of γ's originating in the target region. Referring to the discussion by Leutz[12] at the Heidelberg conference, this corresponds to detecting

(a) for 1 π^o events, 63% as 2 γ's and 32% as 1 γ

(b) for 2 π^o events, 38% as 4 γ's and 30% as 3 γ's

(c) for 3 π^o events, 25% as 6 γ's and 20% as 5 γ's.

To use this feature best the chamber field should be increased to provide better pair energy measurement. The following discussion outlines the problem.

The momentum error on an electron track has the following dependence:

$$\left(\frac{\Delta p}{p}\right)^2_{\text{electron}} = \frac{\alpha}{L} + \delta L + \frac{\gamma p^2}{L^n} \qquad \text{C.1}$$

where

$$\alpha = \frac{2}{3}\left(\frac{E_s}{.3\,B\beta}\right)^2 \frac{1}{X_0 \cos^2\lambda} = \text{multiple scattering "MS"} \qquad \text{C.2}$$

with

E_s = 0.021 BeV

B = magnetic field in kG

β = electron velocity/c

X_0 = radiation length in cm

λ = dip angle

p = momentum in GeV/c

and

$$\delta = \frac{y_0^2}{6X_0 \ell n 2} = \text{bremsstrahlung fluctuation "BS"} \qquad \text{C.3}$$

$$\gamma = \left(\frac{8\epsilon}{.3B}\right)^2 \qquad \text{C.4}$$

ϵ = mean setting error in space ($\lesssim 50\,\mu$)

y_0 is defined by $y_0 = -\ell n(1-x)$ where x is the minimum fractional energy loss due to a single bremsstrahlung event. It is assumed that the measurement stops at the point when such an event occurs. The minimal fractional loss is the smallest that can be detected accurately. Typically, in heavy liquid chamber with $\sim$ 23 kG fields, the limit is roughly a 50% energy loss, which gives $y = \ell n 2 = 0.69$. In the 40" chamber with a 70 kG field and $\epsilon \leq 50\,\mu$, it should be possible to detect a 30% loss, so $y_0 = 0.4$.

For this discussion, we will assume $n \simeq 5$ in Eq. (C.1) (see footnote 2, Section II). Let us first investigate how the momentum error varies as a function of magnetic field, electron momentum, and track length (assuming a fixed radiation length of 32 cm). The MS and MP terms in Eq. (C.1) decrease as $1/\sqrt{L}$ and $1/L^{2.5}$, respectively, while the BS term increases as $\sqrt{L}$. Thus there is an optimum length L_0 for electron momentum measurements given by

$$\delta L_0^6 - \alpha L_0^4 - 5\gamma p^2 = 0. \qquad \text{C.5}$$

For momenta of 200 MeV/c or less, the MP error becomes negligible and $L_0 = \sqrt{\alpha/\delta}$, which varies as $(1/By_0)$ in this range, independent of momentum or radiation length, and is about 5 cm for 70 kG and 9 cm for 23 kG. In this region, the momentum error is proportional to $\sqrt{y_0/B}$; that is, $\left(\frac{\Delta p}{p}\right)^2 \sim \sqrt{\alpha\delta} \sim y_0/B$. At higher momenta, the MP error cannot be neglected, which implies a higher value of L_0. This in turn makes the MS error negligible, so $L_0 = \left(\frac{5\gamma p^2}{\delta}\right)^{1/6}$, which varies as $\left(\frac{p}{By_0}\right)^{1/3}$ and $\left(\epsilon^2 X_0\right)^{1/6}$, and is roughly 13 cm for p = 1 GeV/c, B = 70 kG,

$\epsilon = 25 - 50\,\mu$, $X_0 = 32$ cm, and $y_0 = \ell n\ 3/2$. Thus, as B increases, the optimum length decreases only slowly so that the typical electron in neon would be measured optimally over a length from 5 to 15 cm. In this limit, however, the momentum error is proportional to $\left(y_0^5/B\right)^{1/6}$. Over the momentum range of greatest concern to us, the factor of 3 gain in magnetic field and 1.7 reduction in y_0 result in a reduction factor of ~ 2 in $\left(\frac{\Delta p}{p}\right)$ electron.

Table 2.1

B	p	L_0	$\Delta p/p$
23 kG	100 MeV/c	9 cm	15%
70 kG	100 MeV/c	5 cm	7%
23 kG	1000 MeV/c	15 cm	21%
70 kG	1000 MeV/c	13 cm	11%

It is important to realize that the reduction in y_0 and hence in the bremsstrahlung error Eq. (C.3) is a direct result of the increase in magnetic field. For a given momentum electron and a given fractional energy loss via bremsstrahlung, the visibility of the change in momentum will vary directly with the magnetic field. Using the 1000-MeV case as an example, we have assumed that in a 23-kG field, the minimum detectable energy loss is 50%, or 500 MeV. This corresponds to a change in the radius of curvature from about 150 to 75 cm, detected within less than the 15 cm of track to be measured. For the 70-kG field, the change is from 50 to 25 cm, with some 13 cm of track being measured and with the final electron being captured into a spiral. Thus our assumption that tripling the magnetic field should reduce the minimum detectable bremsstrahlung fluctuation from $\sim 50\%$ to $\sim 33\%$ is actually quite conservative.[13] Figures 2.12 through 2.17[14] show the variation with L of each of the three terms in Eq. (C.1) and their total, assuming B = 70 kG, $\epsilon = 50\mu$, $X_0 = 32$ or 38 cm, $y_0 = \ell n\ 3/2$, and p = .5, 1.0, and 2.0 GeV/c.

The angle errors on an individual electron are quite large, on the order of a few degrees in our case. However, they do not contribute to the error on the gamma direction, since that direction is typically defined to better than a milliradian by the line connecting the primary interaction point with the gamma "nose." The main effect of the electron angle errors is to permit ambiguity among possible γ origins. Here one gains the full factor of three from the magnetic field increase, since showers are rotated through three times the angle to reduce the most important source of such ambiguity, namely that between the primary origin and bremsstrahlung origin from γ's upstream of the given ambiguous γ. Use of an H_2 target also helps by allowing the γ's flight path in the hydrogen to get spacially separated before making showers in the neon mix, i.e., the ambiguities will be reduced by reducing the degree to which the showers overlap. In general, we should expect fewer than 1% ambiguities of this class.

Since the direction errors are essentially negligible once γ's have been assigned to an interaction vertex, the momentum errors are completely dominant. Therefore, we expect to gain at least a factor of two (Table 2.1) in the mass resolution of $\gamma\gamma$ pairs — or equivalently in the efficiency of the 1-c π^0 fit to reduce background and correctly pair γ's. To see just what this will mean in terms of mass errors on resonances, we can extrapolate the results of B. Daugeras et al.[15] on the Ecole Polytechnique 1-meter heavy liquid chamber. Their conditions were: B = 17 kG, X_0 = 25 cm, $\epsilon \simeq$ 50 microns, and a beam momentum of 16 GeB/c, which reduces to p = 1-2 GeV/c for electrons from $\pi^0 \rightarrow 2\gamma \rightarrow e^+e^-$, e^+e^- decays. Putting these values into Eq. (C.1), we predict $(\Delta p/p)$ electron ~26%, whereas the observed value was ~ 30% (which is quite consistent). Thus we would expect mass errors roughly one-third as large as they experienced. Qualitatively, they found that the error contribution from a π^0 (reconstructed from 2γ's by a 1-c fit) was roughly

the same as from a charged pion. Three-body pion resonances typically had errors of: $\pi^- 2\pi^0 \longrightarrow \pm 40$ MeV, $\pi^+ 2\pi^- \longrightarrow \pm 30$ MeV, $\pi^+\pi^-\pi^0 \longrightarrow \pm 25$ MeV, which should reduce, in our case, to 12-15 MeV, 9-12 MeV, and 7-10 MeV, respectively.[16]

Finally, there are two other sources of ambiguity which should be considered: (a) incorrect pairing and (b) "cascade" — that is, missing two or three γ's and, as a result, placing an N π^0 event in the (N - 1) π^0 class. The first will gain by a factor of 2-3 over conventional magnets by the reliability of the 1-c fit at the π^0 to discriminate against incorrect pairs, so we may expect less than 5% ambiguities from this source in the major class of events, i.e., $2\pi^0$'s detected as 3 or 4 γ's. Ambiguities from "cascade" will depend somewhat on the type of interaction and energy range one chooses to investigate. In any case, the reduction in missing mass error (again by a factor of 2-3) enables one to distinguish quite well between $2\,\pi^0$ and $1\,\pi^0$ events, and reasonably well between $3\,\pi^0$ and $2\,\pi^0$ events. We can expect < 3% ambiguities from the former cascade, and < 10% ambiguities from the latter.

Returning to the three classes of events (1, 2, and $3\,\pi^0$) that one might investigate with such a system, we consider just how well each class can be analyzed.

$1\,\pi^0$

(a) If the π^0 is the only missing neutral, this class may be studied equally well with pure H_2 or with the target and mixture combination. In pure H_2, one has a one-vertex, 1-c fit, and $\Delta m \simeq 8$ MeV, even though no γ's are detected. For the H_2 target and Ne-H_2 mix, there are two vertices: (1) If both γ's are detected (63% of the events), one has either two single vertex fits (1 c at the π decay, 4 c at the interaction) or a multivertex fit (5 c, 2 vertices), giving $\Delta m \simeq 6$-8 MeV. (2) If only one γ is detected (32% of the events), one has a multivertex fit (2 c, 2 vertices), giving $\Delta m \simeq 10$-12 MeV.

(b) For a wide class of interesting events, the π^o will be coupled with another missing neutral (principally the neutron). In pure H_2, the events can only be analyzed for the total missing mass, with $\Delta m \simeq 10$ MeV. This isn't even especially useful, since one will generally be interested in the resonance of the π^o with particles in the final state other than the neutron — and this information is unobtainable. With the target and mix arrangement, in the 63% of events where both γ's are detected (one γ will not give a fit), one has either two single vertex fits (1 c at each) or a multivertex fit (2 c, 2 vertices), giving $\Delta m \simeq 10$-12 MeV for neutron resonances and $\Delta m \simeq 8$ MeV for resonances involving the π^o.

$2\,\pi^o$

This is a very important class, which can only be studied as a missing mass in a pure H_2 chamber. In the proposed NeH_2 mix, the analysis may be grouped as follows:

(a) If all four γ's are detected (38%) each of the π^o's can be reconstructed with a 1-c fit at its decay. Resonances involving 1 π^o will have $\Delta m \simeq 7$-10 MeV; those with both π^o's will have $\Delta m \simeq 12$-15 MeV. One may even study this set of events in the presence of another missing neutral (e.g., a neutron), and resonances involving that neutral will have $\Delta m \simeq 15$ MeV.

(b) For events in which 3 γ's are detected (30%), two will pair to give a π^o (whose resonances will have $\Delta m \simeq 7$-10 MeV). The "odd" γ must be analyzed in a multivertex fit with the main interaction, and the π^o constructed from this fit will produce $\Delta m \simeq 12$-15 MeV for effective masses. This set cannot be analyzed if another neutral is missing (although a total missing mass can be calculated).

(c) Finally, there are 28% of the events in which only two γ's are detected. In one-third of these cases (i.e., 9% of the total), both γ's will come from the same π^o. For these events, essentially the same considerations apply as in (b).

$3\ \pi^o$

The main difficulty with this class lies in correctly pairing the γ's. With four γ's, as in the $2\ \pi^o$ case, there are only three possible ways to arrange the pairs. For $3\ \pi^o$'s, the six γ's can be arranged as pairs in 15 different ways. The most that one can hope is that both γ's from one of the $3\ \pi^o$'s will be measured accurately enough to give a good 1-c fit at that decay. Then the 6, 5, and 4 γ cases reduce to essentially the same as 4, 3, and 2 γ's with $2\ \pi^o$'s. We estimate 20-30% of the total $3\ \pi^o$ sample may be separated and analyzed in this manner.

2. Proposed Experiments

(1) Check on the validity of chiral SU(2) × SU(2). One of the more exacting predictions of this system is that the A_1 should have a strong $\pi + \epsilon$ decay mode with a width of roughly 50 MeV and that the ϵ - meson is approximately degenerate with the ρ (Harari[6]). This latter aspect of the σ makes $\pi + \epsilon$ and $\pi + \rho$ decays virtually indistinguishable, with one exception. Since the Clebsch-Gordan coefficient for an I-spin state of (1, 0) going into two similar states is zero, the A_1^o is forbidden to decay into $\rho^o + \pi^o$, but the $\epsilon^o + \pi^o$ decay is allowed. Hence, if one finds a $\pi^+\pi^-\pi^o$ resonance in the A_1 mass range, and the $\pi^+\pi^-$ combinations peak between 700 and 800 MeV, this would not only confirm the theory but also establish the existence of the σ-meson. Similarly, one could accomplish the same thing by looking for the A_1^o decay into $\pi^o\pi^o\pi^o$, if the statistics on the $3\ \pi^o$ events are good enough.

(2) Accurate determination of the $(\eta\pi)$ and $(\omega\pi)$ spectra up to masses of 1600 MeV or greater. All mesons decaying into $(\eta\pi)$ have $J = 1$ and spin-parity assignments of 0^+, 1^-, 2^+, etc. The $\eta^0\pi^0$ state has positive charge conjugation. Those decaying to $(\omega\pi)$ have negative charge conjugation, and any J^P except 0^+. With the proposed detection system, it would be possible to analyze:

(a) Practically all of the $(\eta\pi)^\pm$ and $(\omega\pi)^\pm$ decays. About 70% of the η's decay into $\gamma\gamma$, $\pi^+\pi^-\pi^0$, or $\pi^+\pi^-\gamma$, and as we saw in the discussion of 1 π^0 events, all of these can be resolved with $\Delta m \leq$ 8-12 MeV. The remaining 30% decay into 3 π^0 or $\pi^0\gamma\gamma$, so roughly half of these will be detected with a $\Delta m \leq 15$ MeV. 86% of the ω's decay into $\pi^+\pi^-\pi^0$, so these can practically all be resolved to $\Delta m \leq$ 8-12 MeV — the remainder go mainly into $\pi^0\gamma$, so greater than three-fourths of them will be detected with $\Delta m \simeq$ 10-15 MeV.

(b) The majority of the neutral $(\eta\pi)$ and $(\omega\pi)$ decays. That 70% of the η's which result in only 2 γ's is now coupled to the second π^0, hence we expect better than 60% detection of 4 γ events with $\Delta m \simeq$ 10-12 MeV. The same holds for the 86% of ω's decaying into $\pi^+\pi^-\pi^0$. Approximately 10-20% of the η's which decay into π^0 2 γ and 30-50% of the ω's decaying to $\pi^0\gamma$ will also be detected in the presence of a second π^0.

An accurate knowledge of these two spectra would resolve numerous difficulties:

(a) The $A_1(1080)$ has a 1^+ assignment at present, as required by the quark model. If any fraction is found to decay into $(\eta\pi)$, this assignment must be rejected.

(b) The $\delta(960)$ must exist and have a J^{PC} assignment of 0^{++} to satisfy the quark model. With this assignment, it must decay into $(\eta\pi)$;

finding it in that spectrum would confirm its existence and exactly fix its quantum numbers.

(c) Some resonances may be "Deck effect," large scattering length, or various combinations of initial or final state scatterings and reflections of established resonances in other channels. The η_V (1050), π_V(1003) and A_1(1080) have been questioned on these counts, and several other possible resonances, such as the $K_S K_S$(1440) are presently excluded for such reasons. If these are true resonances, the best proof is to show that they appear in several decay channels. For example, the π_V(1003) has so far been seen only as a $K\bar{K}$ enhancement in $p\bar{p}$ annihilations at rest. If it is more than just a large scattering length, it must decay into $(\eta\pi)$.

(d) We know that the A_2 decays into $(\eta\pi)$. The shape of the spectrum in that region should help resolve the question of the two A_2 peaks.

(e) The new Gell-Mann-Zweig Model predicts no less than 5 new nonets with masses below 1.5 BeV (Harari[6]). In their I =1 states, four of these nonets could decay into $(\eta\pi)$ or $(\omega\pi)$. Certainly, if there are additional T = 1 resonances at these energies, they are most likely to be found in those decay channels which have been least explored.

(f) Finally, one of the recent successes claimed by Regge theory is the 3^- g-meson as a resonance on the ρ trajectory. If this resonance exists and has the expected quantum numbers, it should also decay into $(\eta\pi)$.

(3) Measurement of the $(\pi^o\pi^o)$ and the $(\pi^\pm\pi^o\pi^o)$ spectra. Detection of 2 π^o's makes possible the following experiments: (a) Detection of the two states required by the quark model with I = 0, $J^{PC} = 0^{++}$. At present, these are assumed to be

the $\epsilon(720)$ and η (1050), and at least one, the ϵ, must decay into 2 π^o's. (b) The σ particle: for years there have been sporadic reports of an experimental dipion, I = 0 "bump" near 400 MeV. Again, this should appear in an accurate $(\pi^o\pi^o)$ spectrum, if it is a resonance. (c) Separation of B- and f-mesons: it has been suggested that the B- and f-mesons may be one and the same, with I = 1. This is best resolved by looking for the f in the $(\pi^o\pi^o)$ spectrum; if it appears, then it must have I = 0; if not, this would be strong evidence that the B = f hypothesis is correct. (d) If the Peierls mechanism is involved in the production of the $A_1^{\pm}$, then only $(\rho^o\pi^{\pm})$ is possible in the final state. Alternately, if the A_1 is a pure T = 1 state, the decay $(\rho^{\pm}\pi^o)$ is equally likely. Since this latter decay contains 2 π^o's, it has not been confirmed, but should appear in the $(\pi^{\pm}\pi^o\pi^o)$ spectrum.

In general the neutral channels provide restrictions on quantum numbers so the importance of systematic studies of neutral channels — either containing one meson from the set $(\pi^o\rho^o\omega^o)$ matched with a kaon, baryon, or hyperon, or two mesons from this set — can hardly be exaggerated. Table 2.2 details the quantum number specificity of some neutral two-meson channels compared with their charged counterparts where Böse symmetry is less restrictive, and a multiplicity of further experiments are suggested.

Table 2.2

State	I	J^P	G	C
$\eta^o\eta^o$	0	0^+, 2^+, etc.	+	+
$\pi^o\pi^o$	0, 2	0^+, 2^+, etc.	+	+
$\pi^o\eta^o$	1	0^+, 1^-, 2^+, 3^-, etc.	-	+
$\eta^o\omega^o$	0	only 0^+ excluded	-	-
$\pi^o\omega^o$	1	only 0^+ excluded	+	-
$\omega^o\omega^o$	0	0^+, 2^+, etc.	+	+
$\pi^+\pi^-$	0, 1, 2	0^+, 1^-, 2^+, 3^-, etc.	+	+, -

(4) Systematic studies of radiative decays. The clean separation of γ, π^o, 2 π^o and $> 2\ \pi^o$ classes makes possible a detailed study of virtually all possible radiative decays of mesons or baryons. Note that $\pi^{\pm}\gamma$, $\pi^+\pi^-\gamma$, $K\gamma$, $K\pi\gamma$, $Y^* \longrightarrow \Lambda\gamma$ or $\Sigma^{\pm}\gamma$ etc., are essentially unstudied so far. Comparison of $N^* \longrightarrow p\gamma$, $p\pi\gamma$, etc., with photoproduction should be interesting. Even measurements of η, η', $X^o \longrightarrow e^+e^-\gamma$, $\Sigma^+ \longrightarrow p\gamma$, pe^+e^-, $\Sigma^{\pm} \longrightarrow n\pi^{\pm}\gamma$, $\Xi^- \longrightarrow \Sigma^-\gamma$, etc., or $\phi \longrightarrow \eta^o\gamma$, $X^o \longrightarrow \omega^o\gamma$, $\pi^{\pm}\pi^o\gamma$, $\eta^o \longrightarrow \pi^+\pi^-\pi^o\gamma$, $N^* \longrightarrow p\pi^o\gamma$, $p\eta^o\gamma$, $p\omega^o\gamma$, $Y^* \longrightarrow \Sigma^o\gamma$, $\Lambda^o\pi^o\gamma$, $\Lambda^o\eta^o\gamma$, etc., could be improved. The ability to handle such events is enhanced by use of the counter array described in Section II. B, and by the fact that at 70 kG, the chamber would effectively trap $e^{\pm}$, $\mu^{\pm}$, and $\pi^{\pm}$ secondaries with momenta up to 800 MeV c, making possible unambiguous identification (see Section II. A, part 2).

(5) Search for missing I = 0 resonances. In the mass region between 1050 MeV and 1400 MeV, the quark model requires three I = 0 resonances which have yet to be found: (a) A 1^{++} isoscalar is predicted around 1050-1300 MeV. This could decay into 4π, $K\bar{K}\pi$, KK^*, $\pi\pi\eta$, $\pi\delta$, etc. Clearly all of these decays favor one or more missing neutrals in the final state, so it is not surprising that the resonance hasn't been detected. With the proposed system, we could certainly detect either $K^+K^-\pi^o$ or $\pi^+\pi^-\eta$, and we would probably detect $\pi^+\pi^-\pi^o\pi^o$. (b) There are two 1^{+-} isoscalars missing, with masses typically 1200 and 1400 MeV. At least one should decay to $\rho\pi$, but especially at 1200 MeV the $\rho^{\pm}\pi^{\pm}$ will be lost among the A_1 and A_2 neutral decays. To quote Harari,[6] "The 'cleanest' way of seeing this state is in the $\rho^o\pi^o$ invariant mass plot, which should not show the I = 1 states." Both 1^{+-} states should also decay to $K\bar{K}\pi$. However, two presumably stronger I = 0 resonances have the same decay mode in the same mass regions, the D(1280) and E(1410). A distinction is that the sought-after 1^{+-} states can

decay into $K_1^0 K_2^0 \pi^0$, which is not allowed for the D or E. With the proposed detection system, we can certainly get a sharp ($\rho^0 \pi^0$) invariant mass plot; as for the $K_1^0 K_2^0 \pi^0$ decay, in virtually all cases, we will be able to separate these events, and the error on the calculated mass should be $\simeq$ 12 MeV. (c) Since the I = 1 resonances go up to 2380 MeV, we might expect higher I = 0 resonances than the f*(1500). In fact, the I = 1 table would cut off around 1650 MeV if it were not for the fact that missing mass spectrometers, which only detect charged resonances, have moved that limit to 2400 MeV. The reason that bubble chambers have been unable to extend their research to higher resonant masses is quite simple — these heavier mesons necessarily have an ever greater fraction of final states containing two or more π^0's, and practically all final states with at least 1 π^0. Thus we may expect that a detection system giving strong resolution of all 1 π^0 events and moderate resolution of 60% of the $2\pi^0$ events should extend bubble chamber analysis in all three I-spin channels to masses of 2000 MeV or greater.

D. 70-kG Magnetic Field, Beam Entry

1. Entry of Charged Particles to the Bubble Chamber

Beam transport calculations indicate that charged beams with $p \geq 2.0$ GeV/c can be easily injected into the chamber through the entry slit and the window opening, which has the dimensions of 10 cm × 35 cm. The path of the beam is shown in Figs. 2.18, 2.19, and 2.20. As can be seen from the figures, the resultant trajectories and path lengths are acceptable, and the only complication involved is the need to elevate the chamber from its present position some 25 cm, with respect to the beam line, for particles with momenta in the interval of 2.0-2.5 GeV/c, to prevent their colliding with the upper boundary of the slit. This elevation is accomplished by means of lifting devices already present.

2. Beam Entry to the Chamber Using Field Counteracting Transport Magnets

Although the bulk of the physics envisioned for the bubble chamber will involve beams of greater than 2 GeV/c momenta, there are a number of interesting experiments which would require lower momentum beams. To allow for injection of such low-momentum beams, two systems of magnetic shielding were studied:

(a) A superconducting beam pipe with an elliptical useful aperture of 5 × 10 cm.

(b) A system of dipole magnets appropriately located from outside the iron yoke to the bubble chamber window.

Although the superconducting beam pipe seems attractive and field computations indicate that the field can be shielded up to 90% of the external dipole field, it is presently difficult to calculate the effect of a highly non-uniform field (which changes from +70 kG to - 18 kG over a length of ~ 1 m) on the shielding currents and their distribution. Also, the compressive forces on the tube are high enough to make the use of reinforcements necessary.

The second scheme, using a number of dipole magnets having a usable elliptical aperture of 5 × 10 cm to correct for the axial and radial field components, is much more attractive.

Each magnet generally counteracts over a certain effective length the axial and radial field components generated by the main superconducting coils. Using SLAC's "BAR" program, we calculated the field distribution within the dipole coils, maximum allowable current densities, and the forces on the conductors for each individual dipole coil. The axial fields produced by each magnet illustrated in Fig. 2.21 and -63 kG, -44 kG, -22.5 kG, and +14 kG, respectively. The maximum axial field amplitudes seen by the injected beam particles will not exceed 15 kG over a short distance of ~ 2...3 cm. The maximum deflection of the incoming beam is then reduced to a maximum of 5 cm for p = 1 GeV/c (Fig. 2.22)

and 10 cm for p = 0.5 GeV/c (Fig. 2.23). The beam of 1 GeV/c will not collide with the vacuum chamber walls, but special effort, by displacing the magnets, is needed to inject 0.5 GeV/c beams. The radial field component is reduced to less than 520 gauss as peak value, and the beam radial deflection is less than 0.5 cm.

The side view of the dipole magnet arrangement and the front view of the major 63 kG dipole magnet are shown in Fig. 2.21 schematically. Preliminary studies indicate that if dipole IV is arranged such that it can be adjusted radially according to the type of experiment required at different locations, dipole III can be eliminated. The drift space between coils IV and II can be adjusted such that the beam enters at a maximum possible entry angle in the bubble chamber and the track length is increased. The noticeable improvement in the beam trajectory within the chamber is thus realized by "pitching" the beam upwards during the last part of its entry.

REFERENCES AND FOOTNOTES

1. "Design Study for a High Magnetic Field Hydrogen Bubble Chamber for Use on Nimrod," Rutherford National Laboratory, England, (January 1967); p. 5-43.
2. The denominator of the first term in Eq. (C.1) lies somewhere between $H^2L^4\cos^2\lambda$. and $H^2L^5\cos^3\lambda$ for most practical measurement applications. The mean of the factor of $(1/L\cos\lambda)^{-1/2}$ can be incorporated into the ϵ^2 in the numerator, in which case a setting error of 25-50 microns is required at 70 kG to make the measurement error negligible up to momenta of 5 GeV/c. As we have said, this is readily attainable with automatic measuring machines.
3. W. B. Johnson and R. Yaari, Memorandum - SLAC (December 9, 1966). is the half-width; the sharpness of the missing-mass-squared distribution. Υ can be summarized roughly by the fraction of the total sample within the limits $0 < mm^2 < 2m_\pi^2$.
4. H. Courant et al., Proc, Sienna Conf. on Elementary Particles 1, 15 (1963).
5. A. N. Mitra and M. Ross, Phys. Rev. 158, 1630 (1967).
6. H. Harari, "Resonances (Theory)," Report No. SLAC-PUB-508, Stanford Linear Accelerator Center, Stanford University, Stanford, California (1968).
7. G. Chikovani et al., Phys. Letters 25B, 44 (1967).
8. B. Levrat et al., Phys. Letters 22, 714 (1966).
9. D. J. Crennell et al., Phys. Rev. Letters 20, 1318 (1968).
10. K. E. Lassila and P. V. Ruuskanen, Phys. Rev. Letters 18, 762 (1967).
11. The possibility of using a hydrogen target inside a 90% Ne - 10% H_2 mixture was suggested by R. D. Watt of SLAC who proposed that the target be a rigid container maintained at a pressure some 50 psi higher than the surrounding mix. A plate attached by a bellows mount to one end of the target and positioned by a bias pressure would then transmit the chamber expansion from the Ne-H_2 to the hydrogen inside the target.

12. H. Leutz, International Colloquium on Bubble Chambers, Heidelberg (1967); p. 49.

13. It is understood that for a given magnetic field, the minimum detectable fractional energy loss will depend on dip angle and momenta, so the presently accepted value of 50% for magnetic fields in the 20-kG range and liquids with ~30 cm radiation lengths is an over-simplified average. This value does enable one to rather successfully make calculations which match the observed error resulting from bremsstrahlung fluctuations, so it may be taken as an empirical average. Assuming all other variables remain unchanged, an increase by a factor 3 in the magnetic field may well reduce this value to ~17%, in which case the factor two reduction of momentum error in Table 2.1 becomes a full factor three. Since new measurement and reconstruction techniques are now in development, which effectively minimize y_0 for each separate track (obviously more accurate than using one average value for all), it may not be optimistic to assume that by the time the proposed magnet is in operation, we will be able to completely realize this factor of 3.

14. George E. Kalmus, Berkeley, (private communication).

15. B. Daugeras et al., Phys. Letters 27B, 332 (1968).

16. We are grateful to H. H. Bingham, Berkeley, for numerous discussions on the theoretical and practical implications of higher magnetic fields in heavy liquids.

17. SLAC, Group B Physics Note 26, July 1968, "κ^0 Experiment Counter Tests," by D. Leith and W. Smart;

SLAC, Proposal No. BC-10, "A Proposal to Investigate $\kappa_2^0 p$ Interactions with the 40-inch HBC," by B. C. Shen and D. Leith.

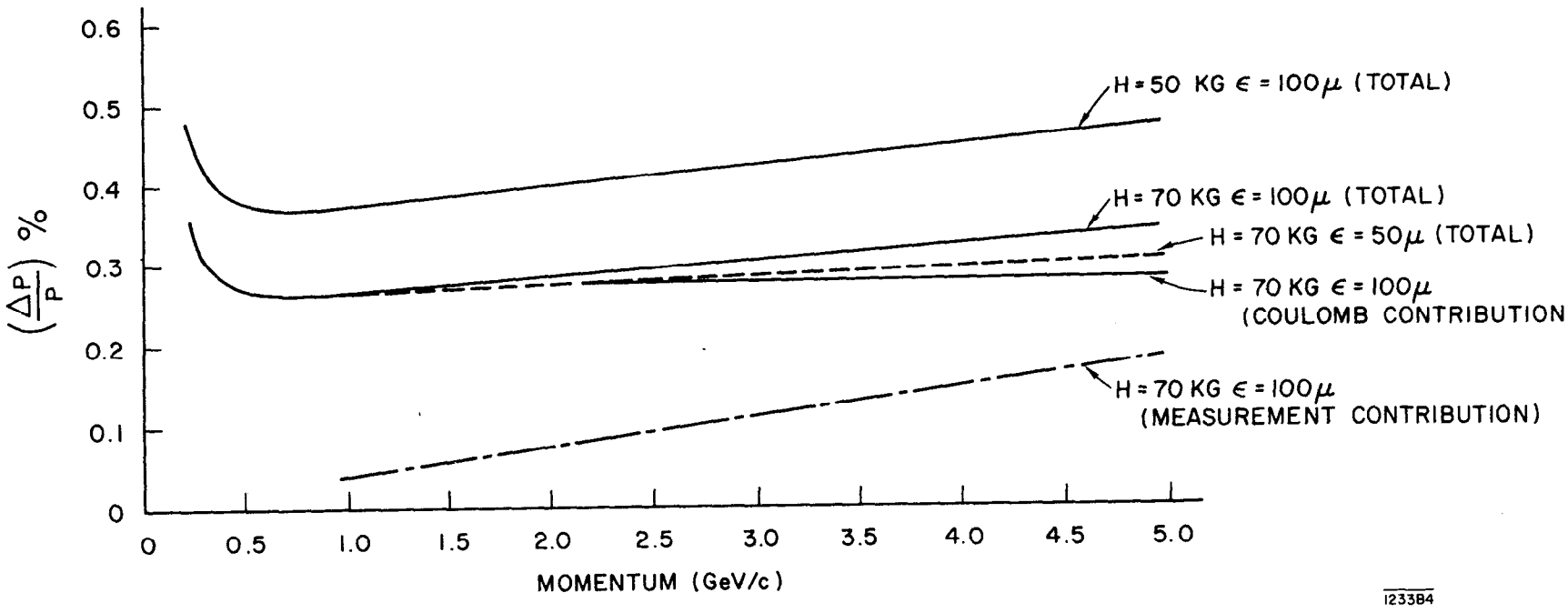

FIG. 2.1--Percentage error on a momentum measurement against momentum for L = 60 cms.

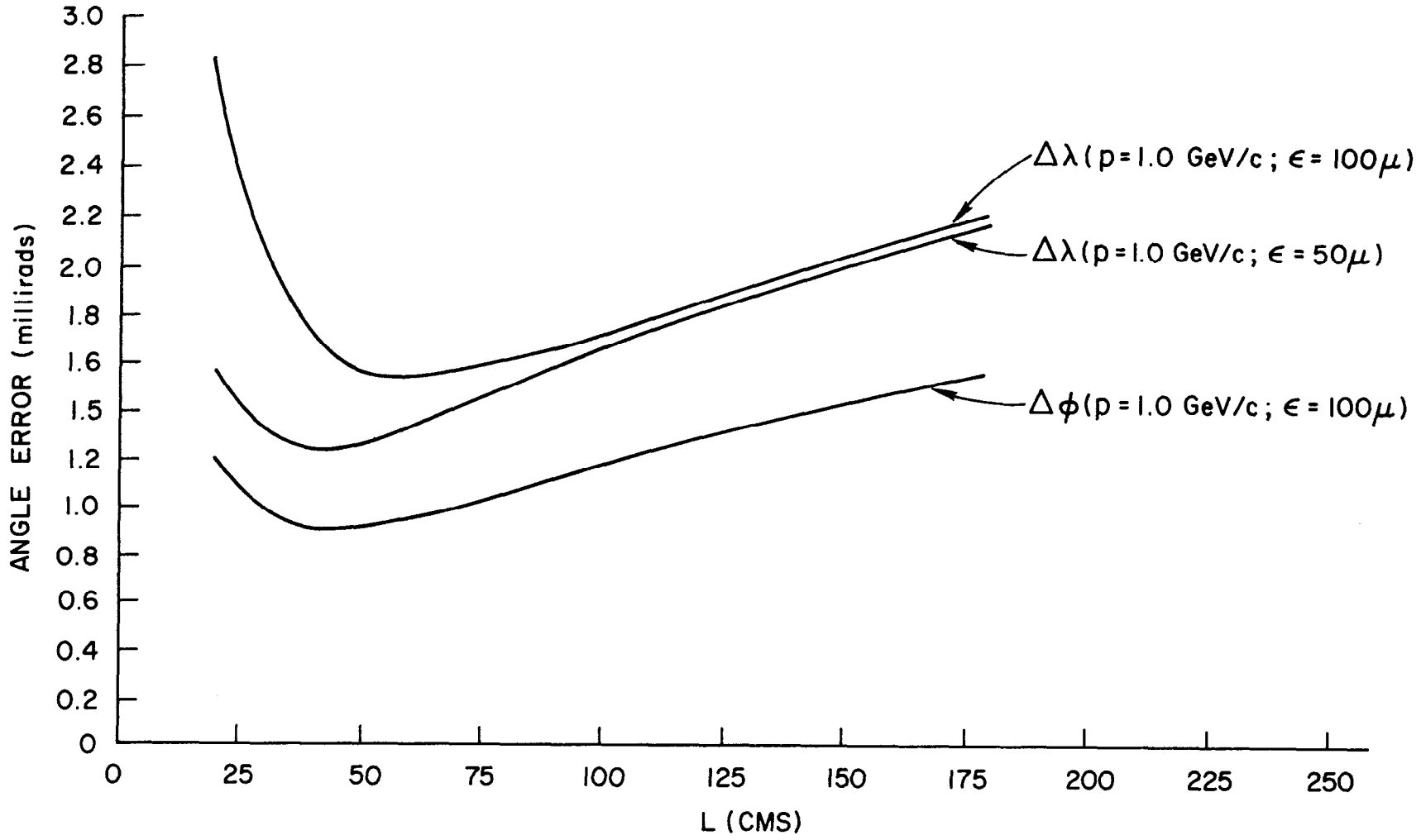

FIG. 2.2--Angle errors for 1 GeV/c track.

123385

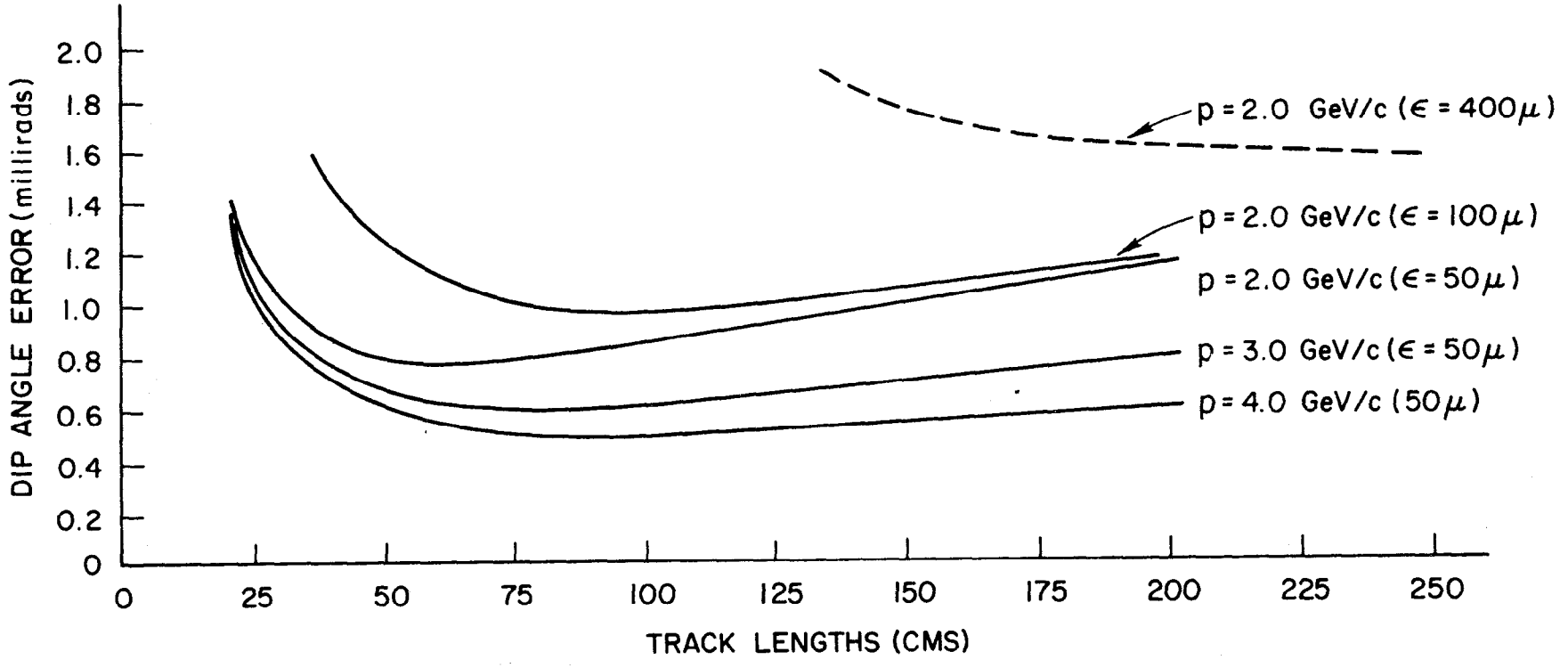

FIG. 2.3--Variation of error in dip measurement with track length for different momenta.

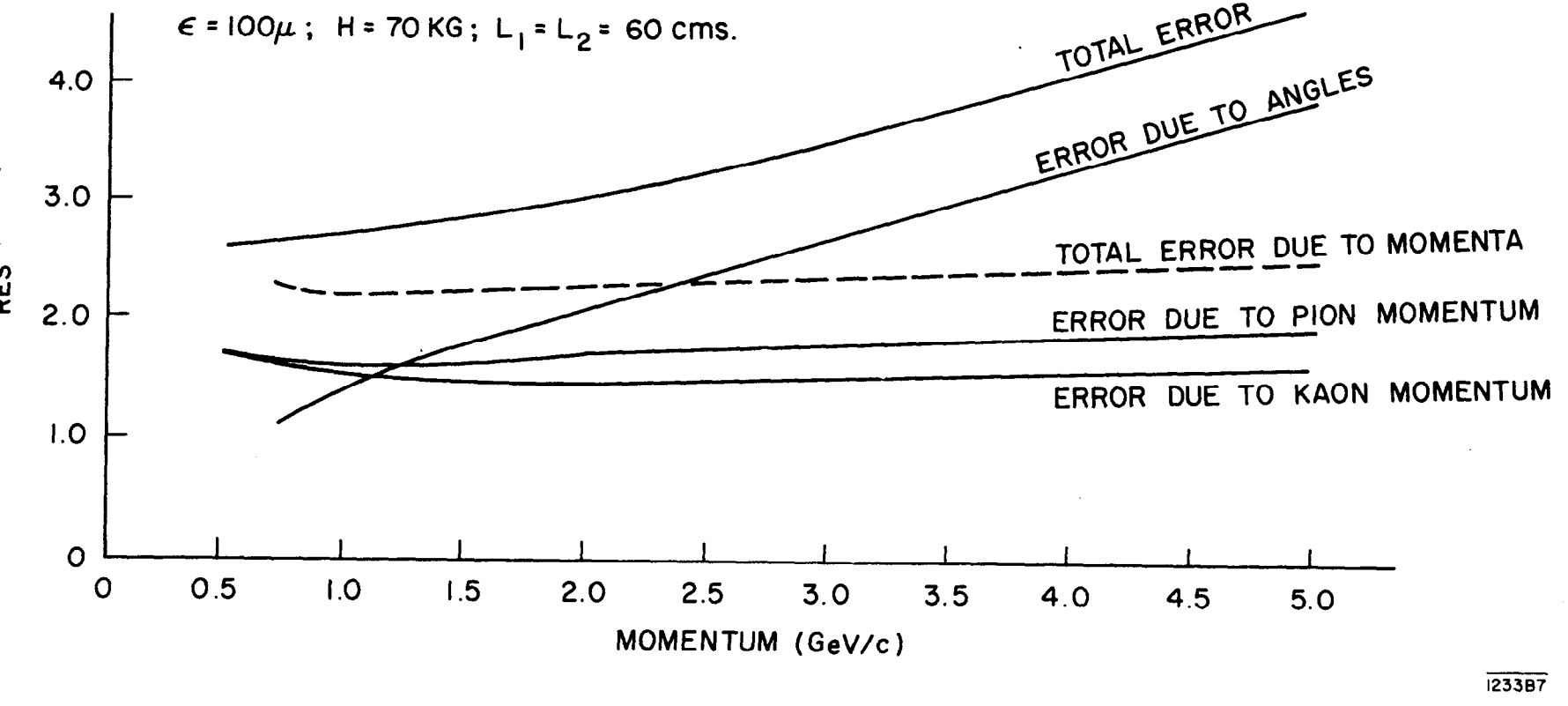

FIG. 2.4--Unfitted errors on the mass of resonance K # (1400) (decay at 90° in center-of-mass system).

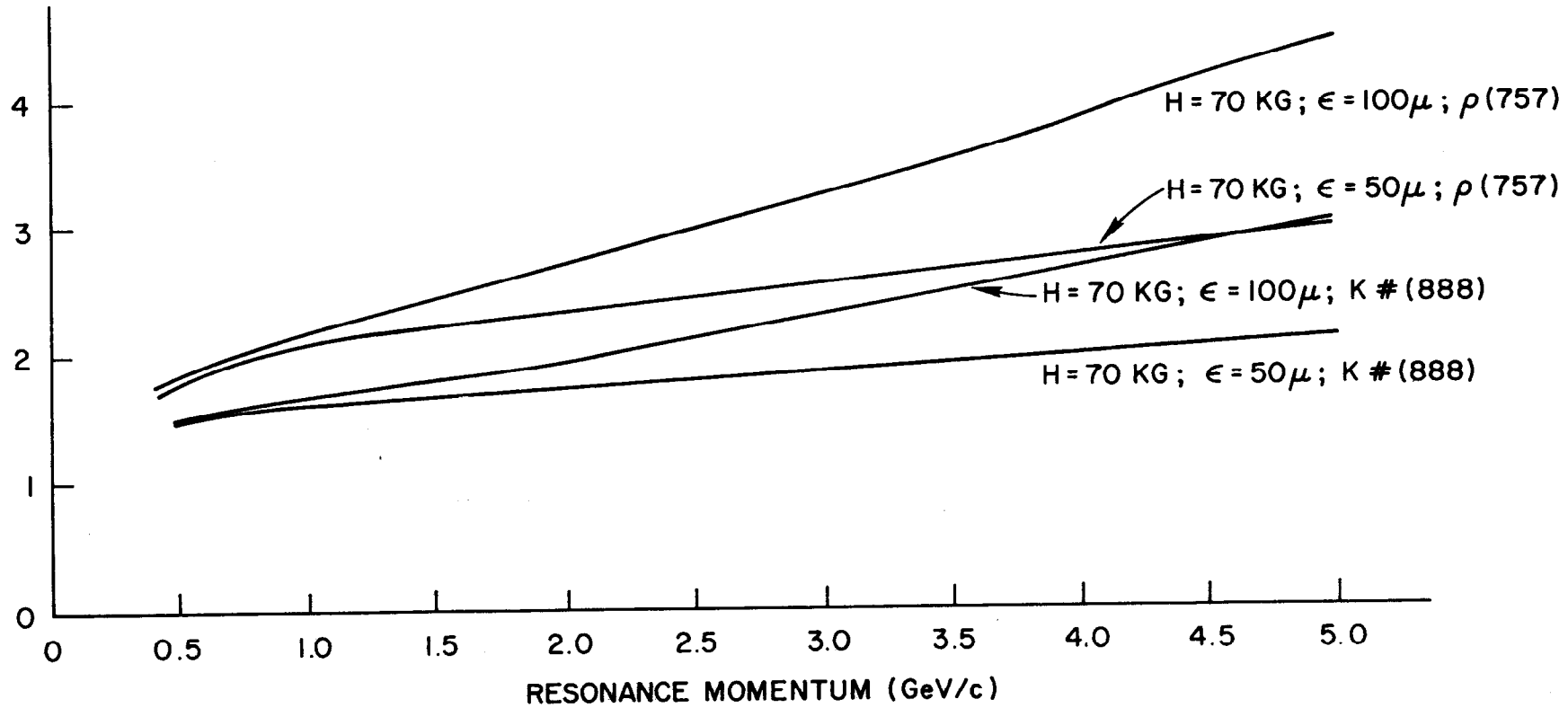

123388

FIG. 2.5--Unfitted error on two-body effective mass values.

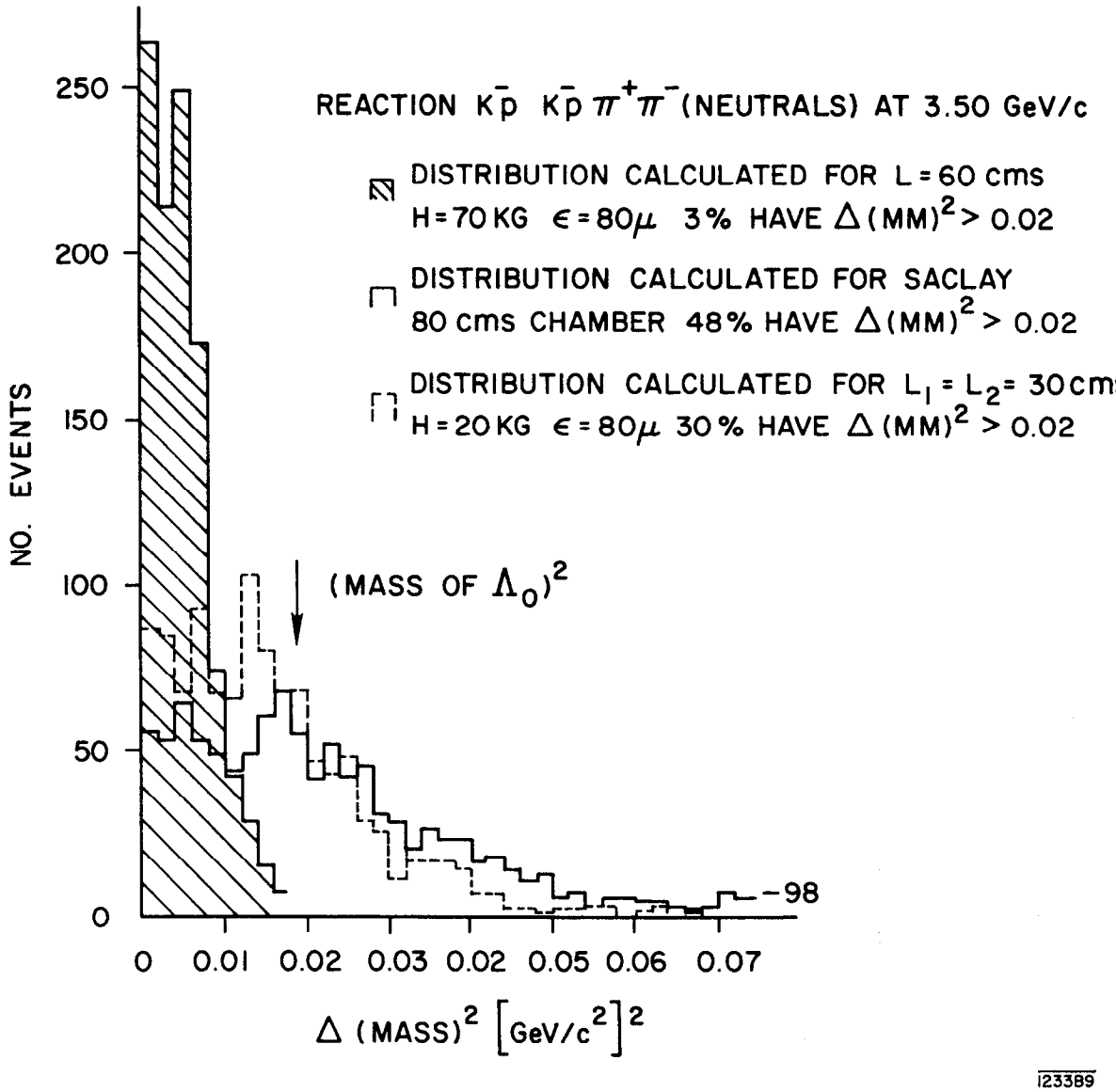

FIG. 2.6--Histogram of Δ(missing mass)^2 showing improved resolution using high field chamber.

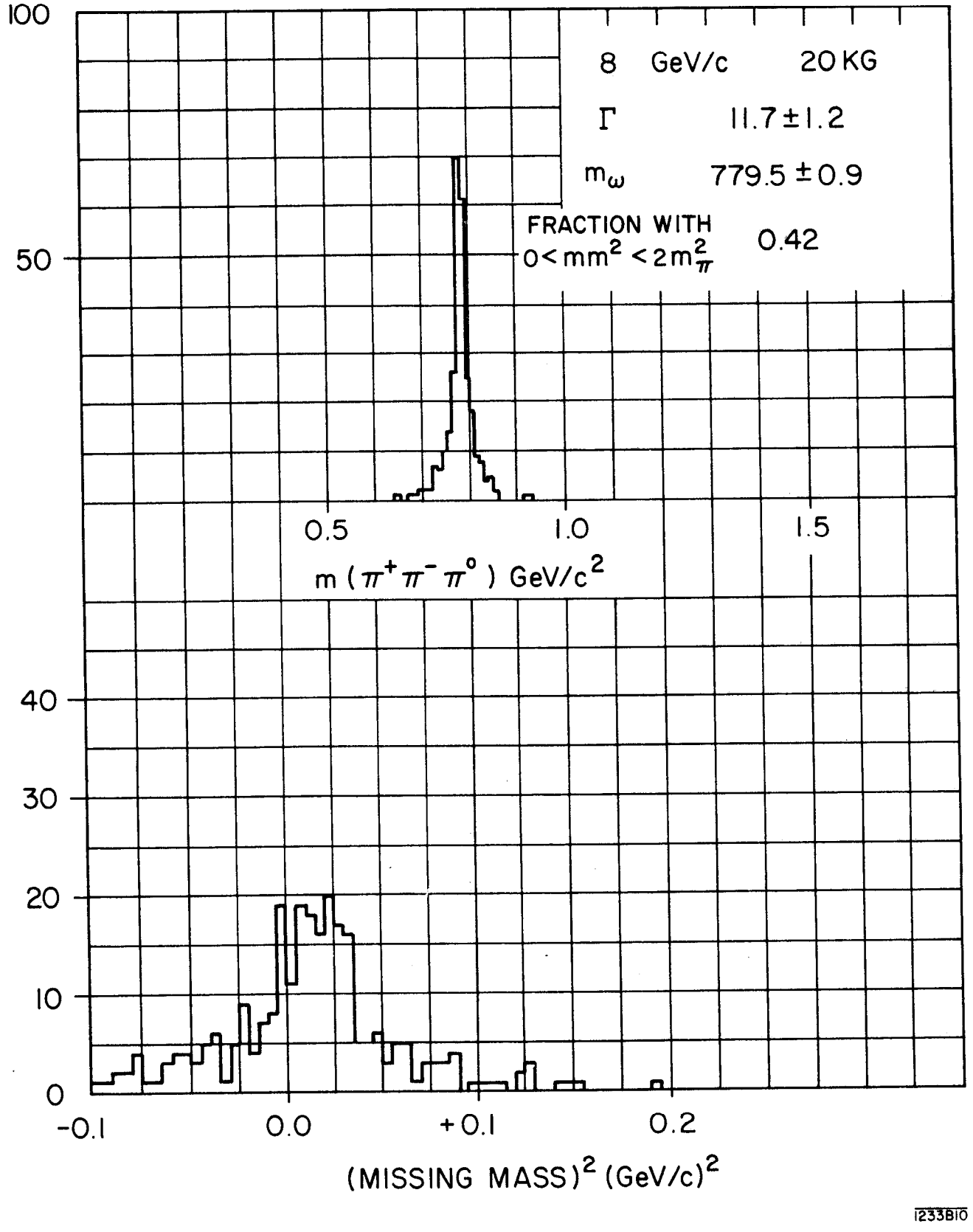

FIG. 2.7--(Missing mass)^2 (GeV/c)^2: 8 GeV/c - 20 kG.

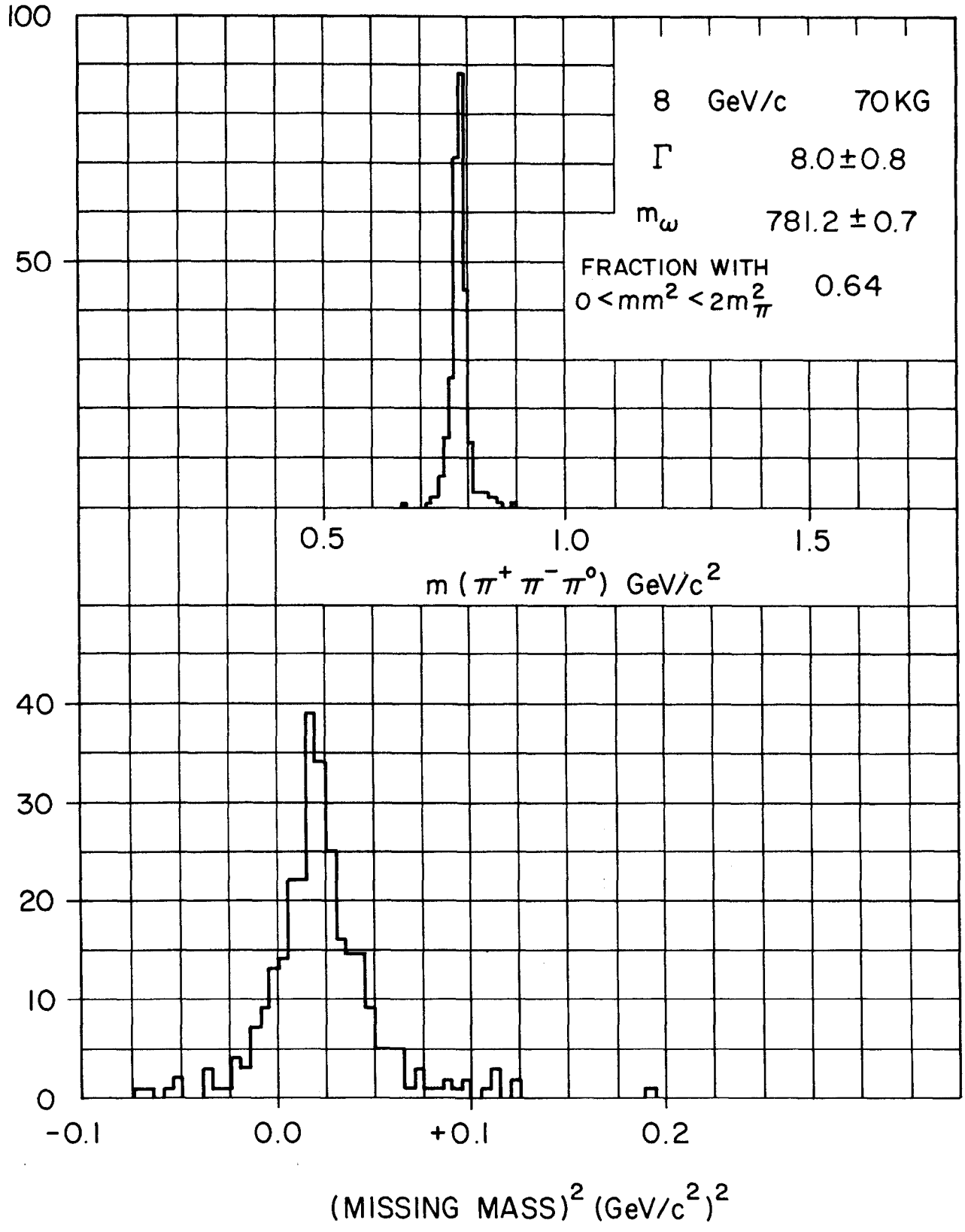

FIG. 2.8--(Missing mass)^2 (GeV/c^2)^2: 8 GeV/c - 70 kG.

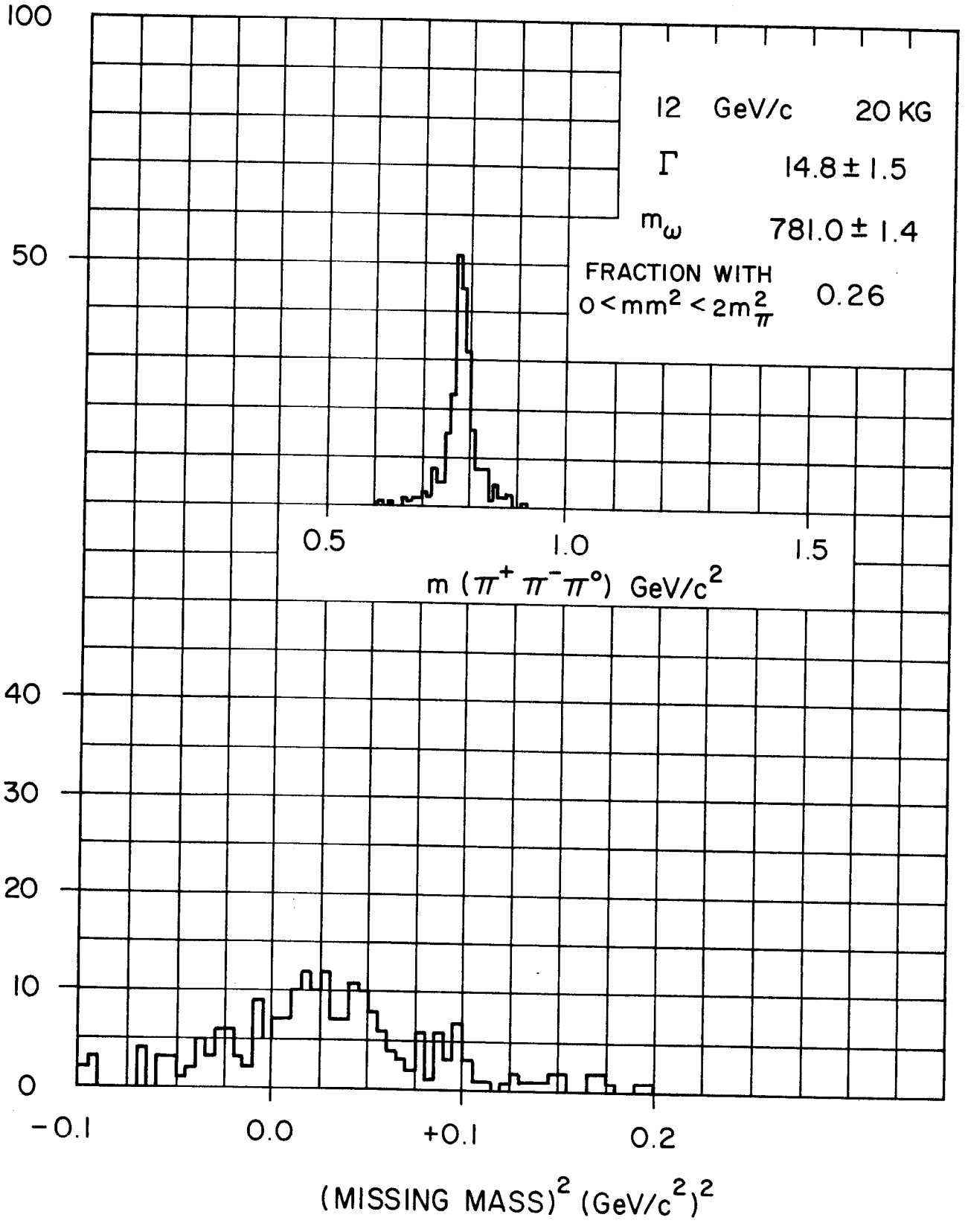

FIG. 2.9--(Missing mass)^2 (GeV/c^2)^2: 12 GeV/c - 20 kG.

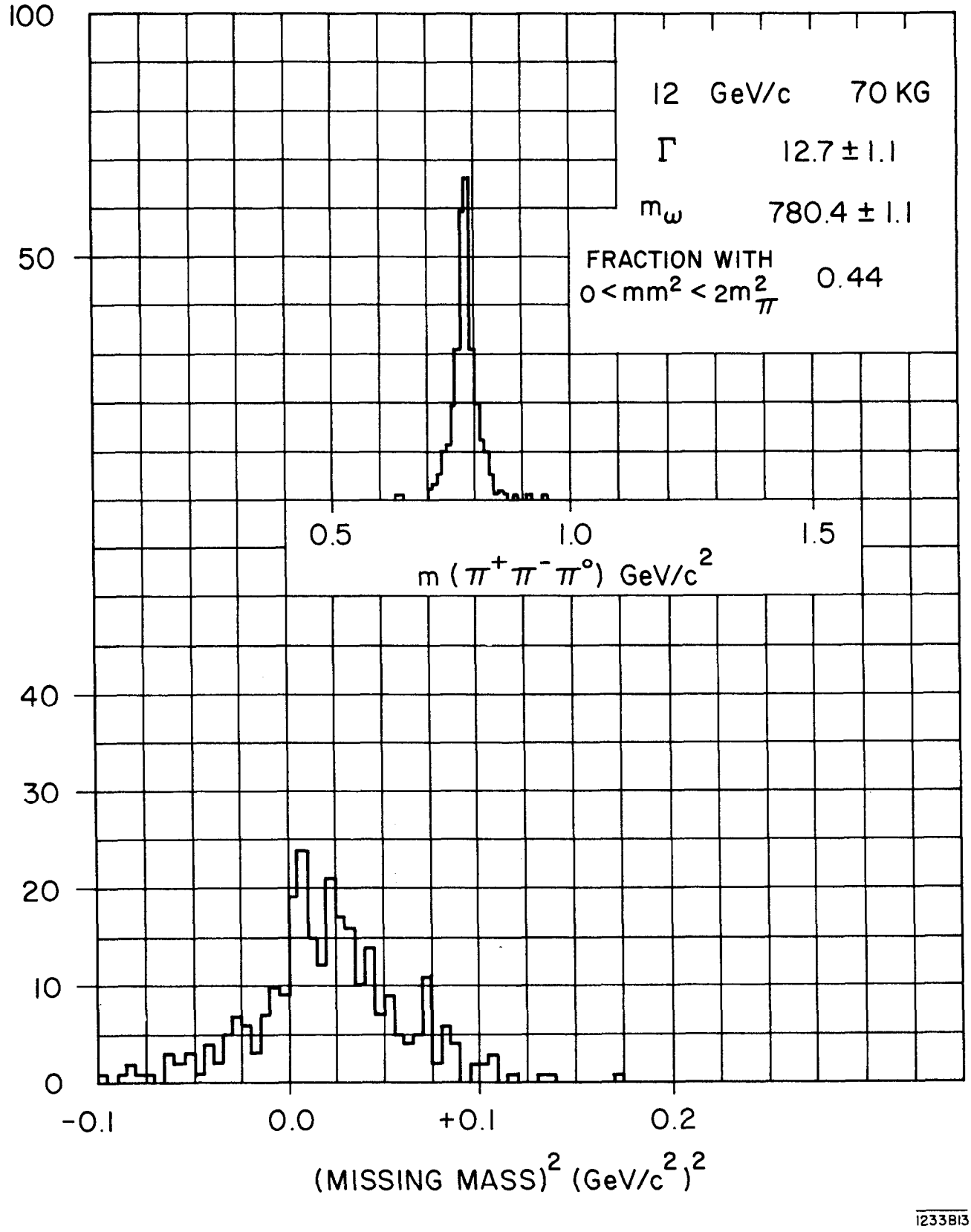

FIG. 2.10--(Missing mass)^2 (GeV/c^2)^2: 12 GeV/c - 70 kG.

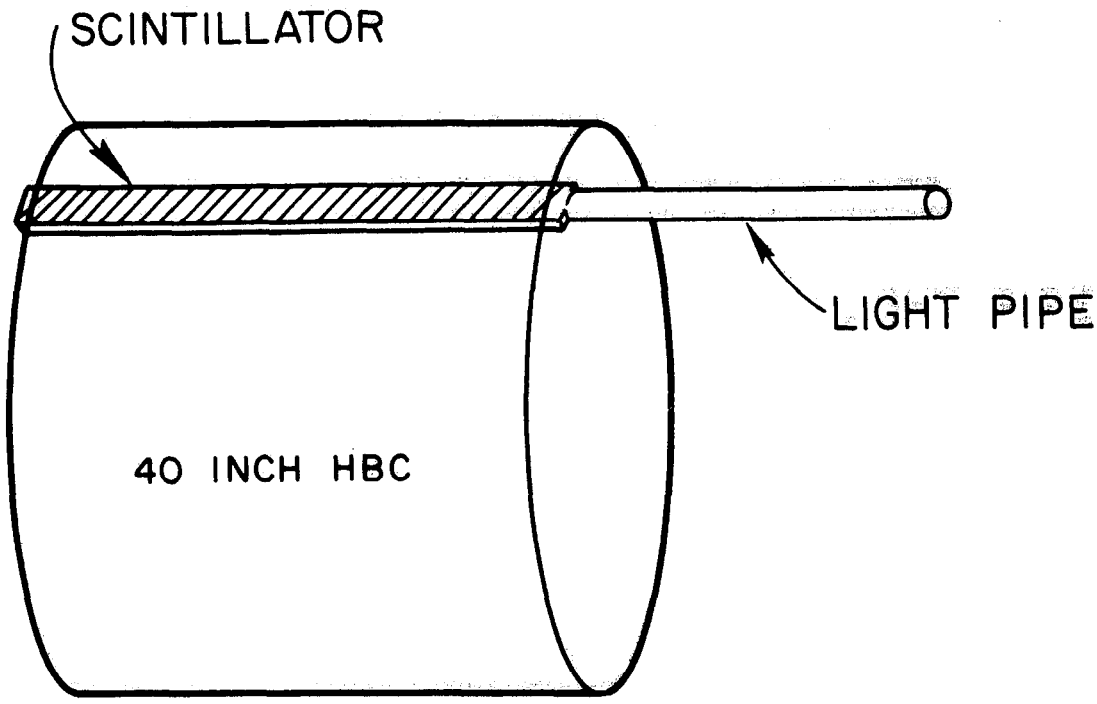

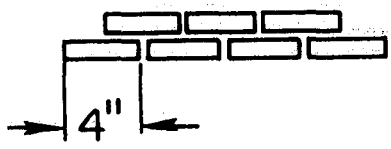

COUNTER STACKING

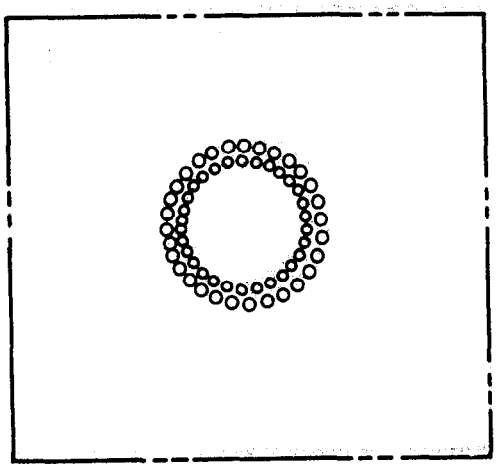

FEED THROUGH ARRANGEMENT
AT CHAMBER EXPANSION END.

1233A14

FIG. 2.11--Particle detectors.

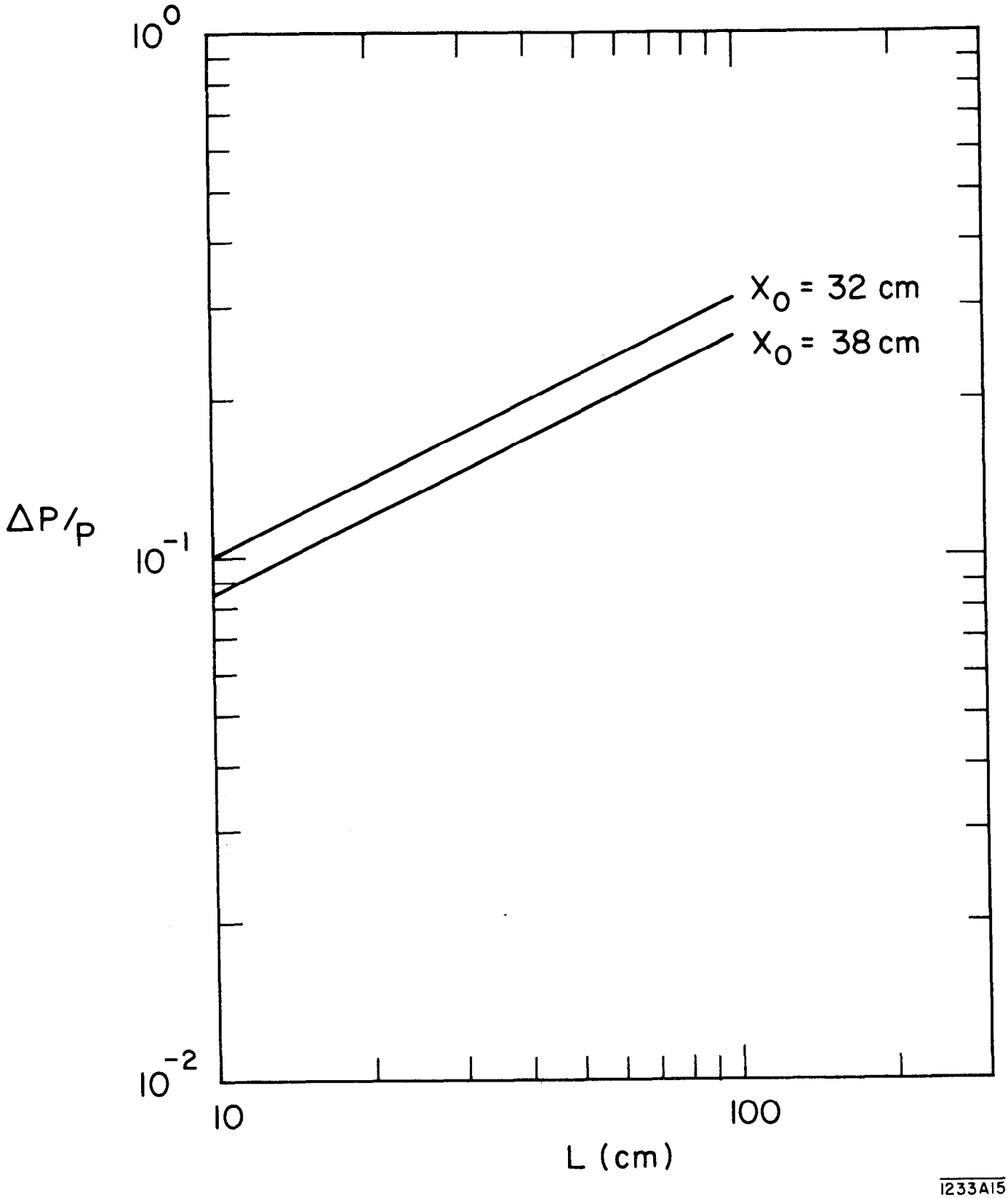

FIG. 2.12--Momentum error due to bremsstrahlung.

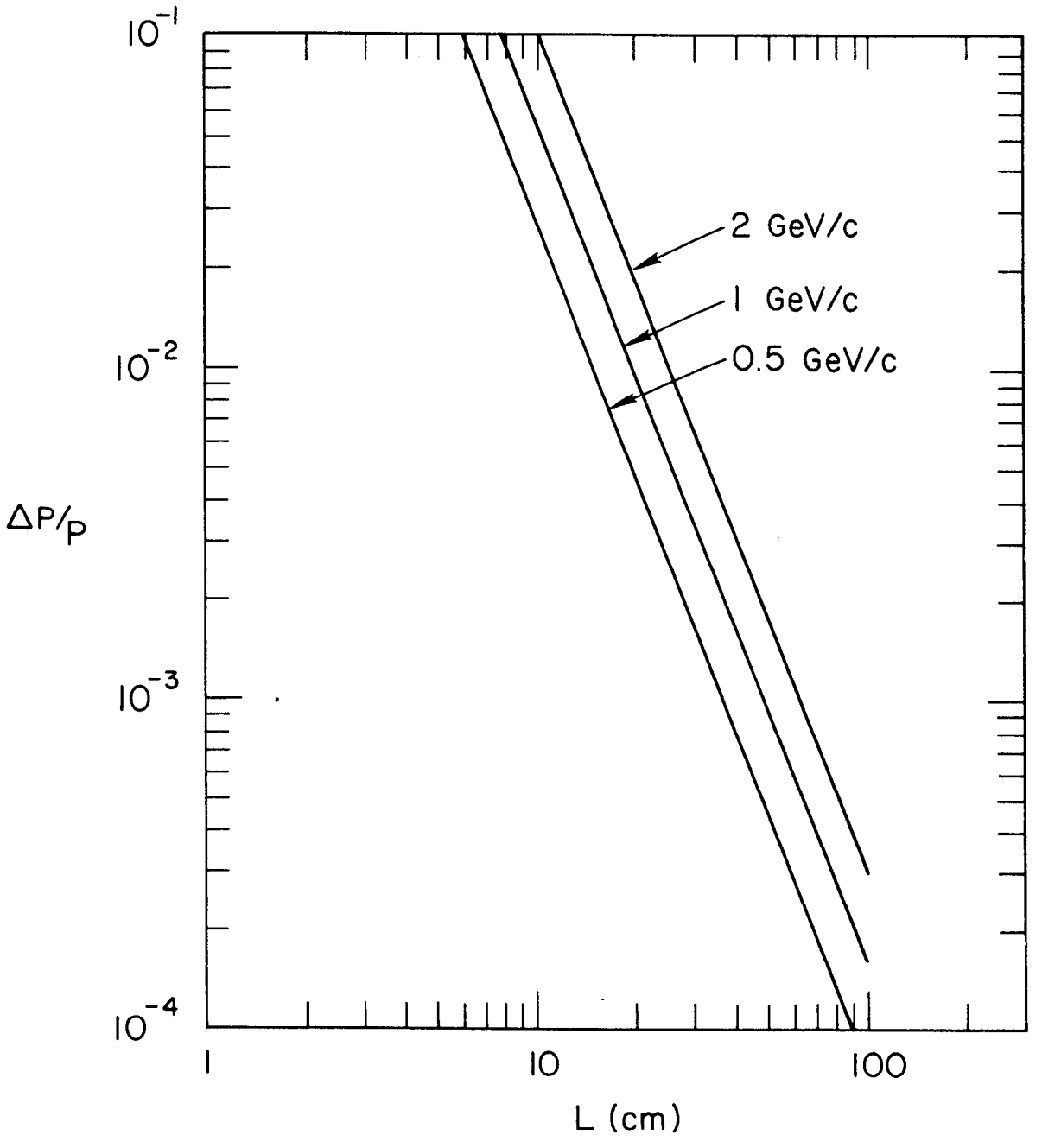

FIG. 2.13--Setting error only.

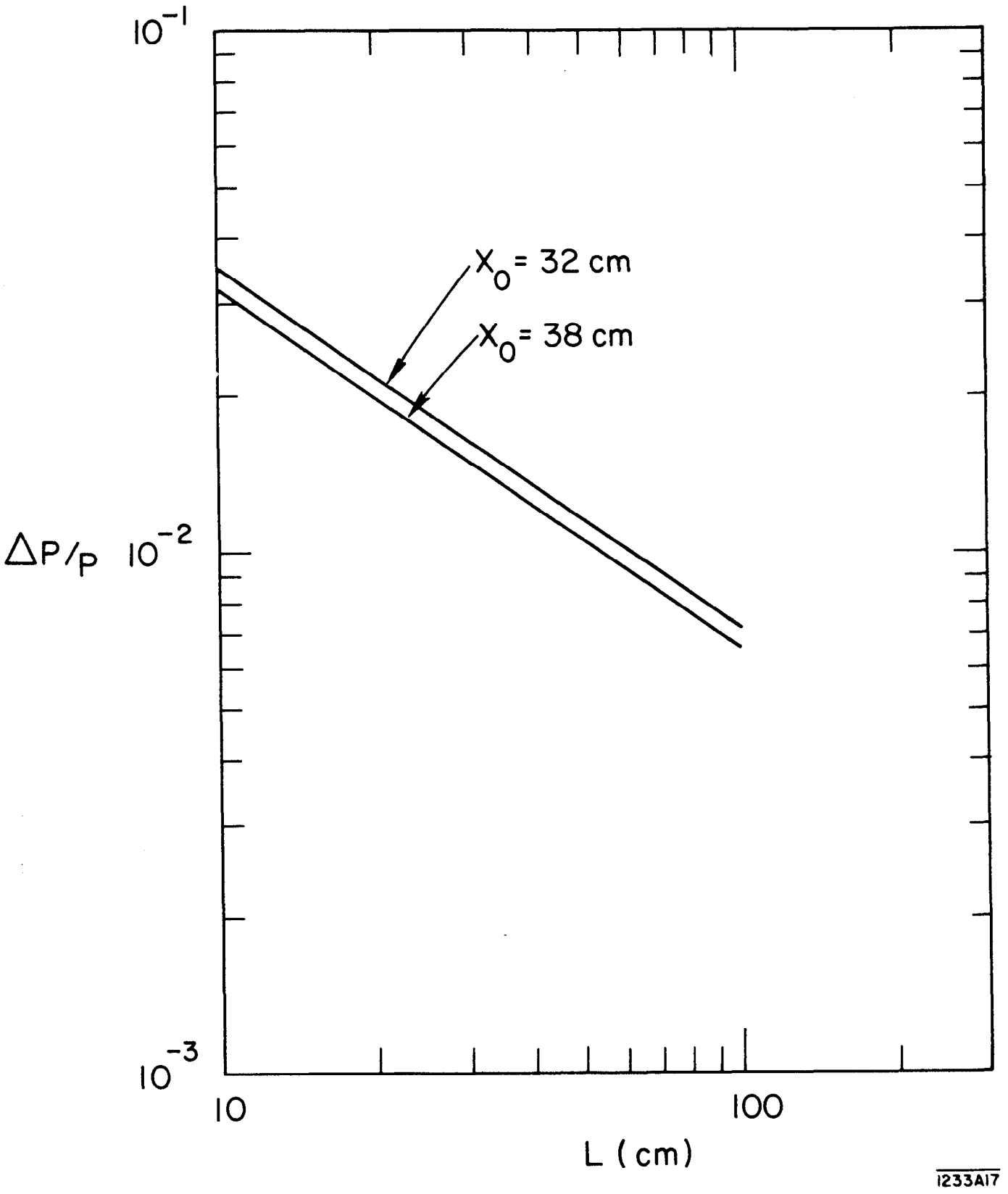

FIG. 2.14--Momentum error due to multiple scattering only (for ~ 1 GeV/c electron).

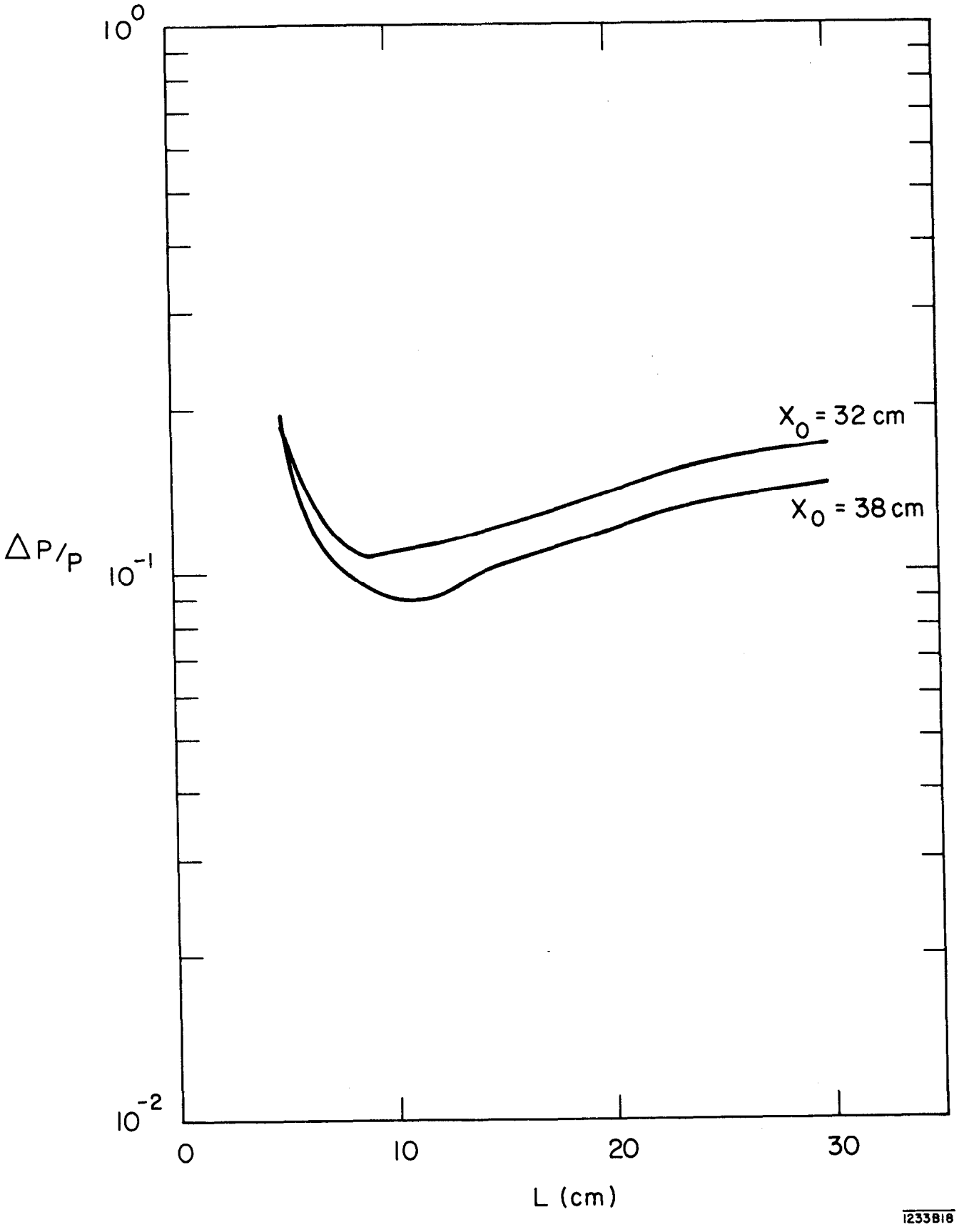

FIG. 2.15--Total error — 0.5 GeV/c.

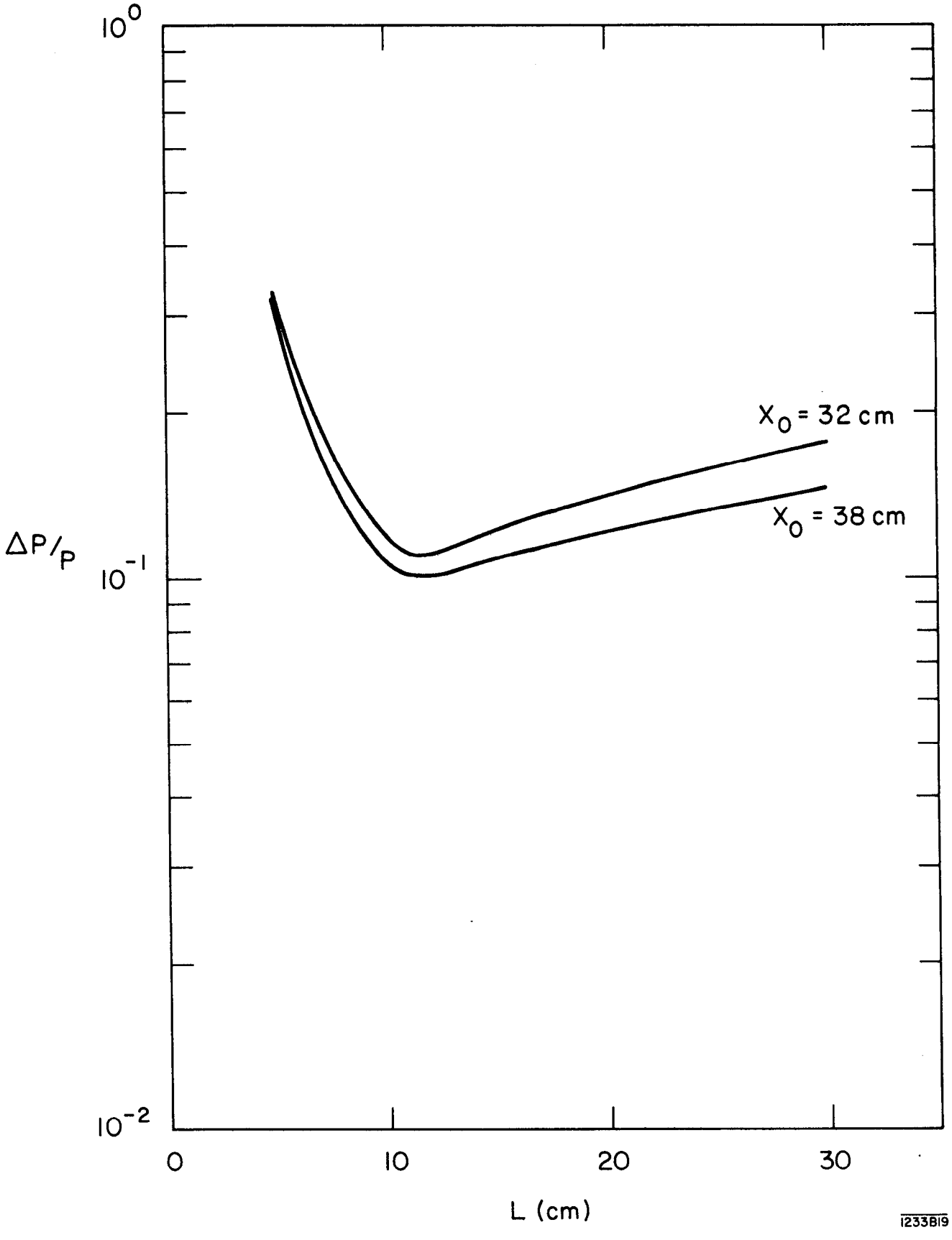

FIG. 2.16--Total error — 1 GeV/c.

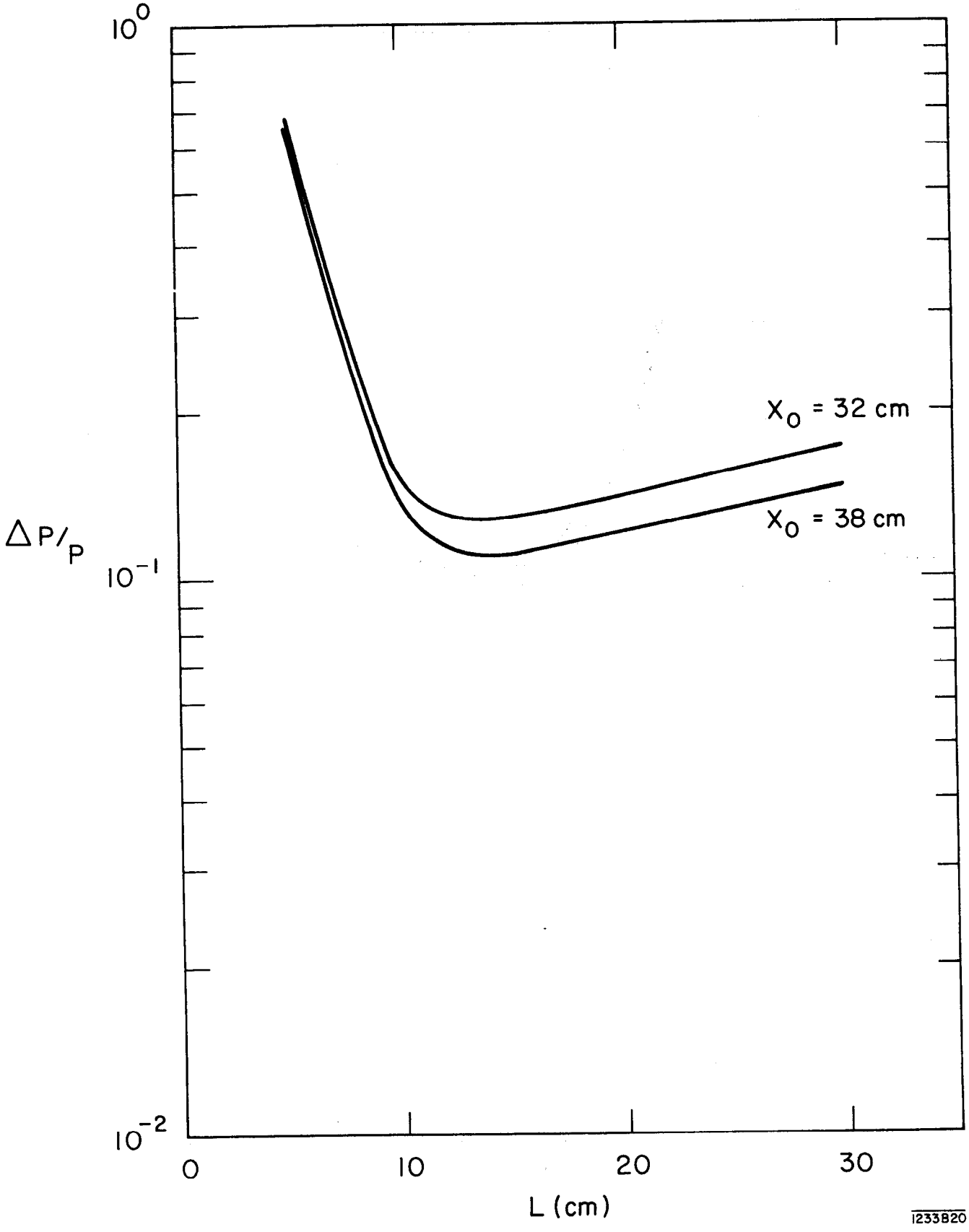

FIG. 2.17--Total error — 2 GeV/c.

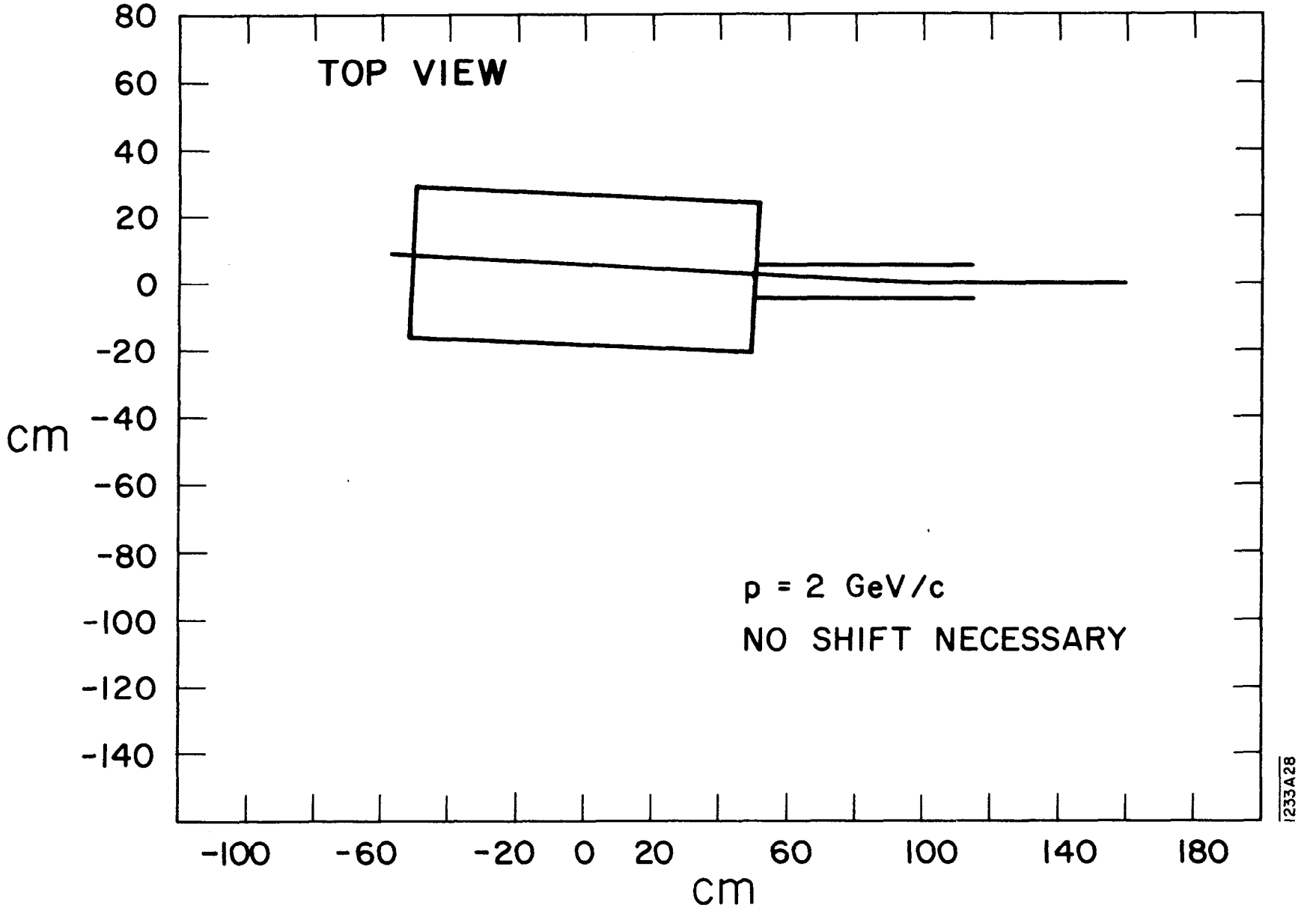

FIG. 2.18--Top view p = 2 GeV/c beam injection (no shift).

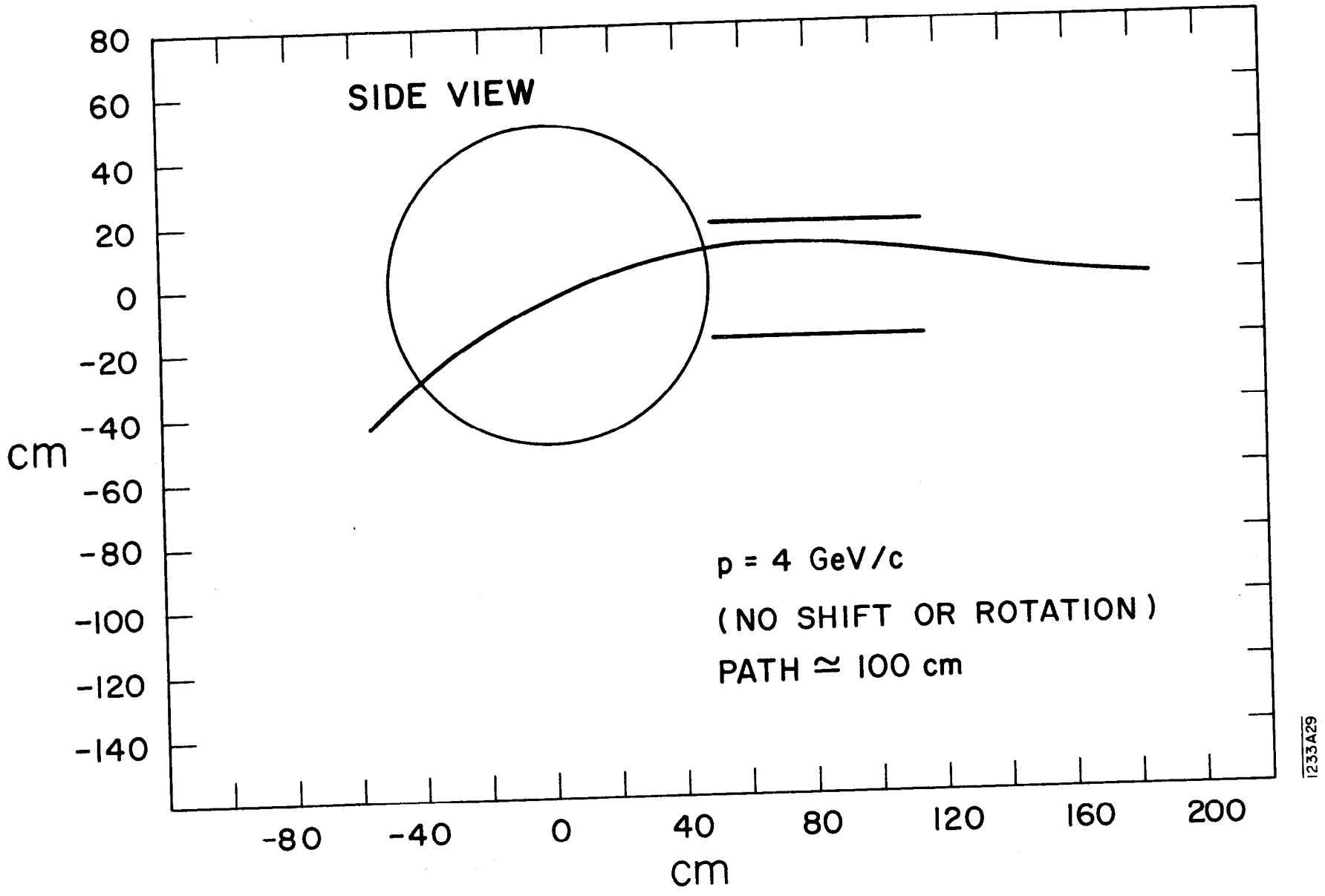

FIG. 2.19--Side view p = 4 GeV/c beam injection (no shift or rotation).

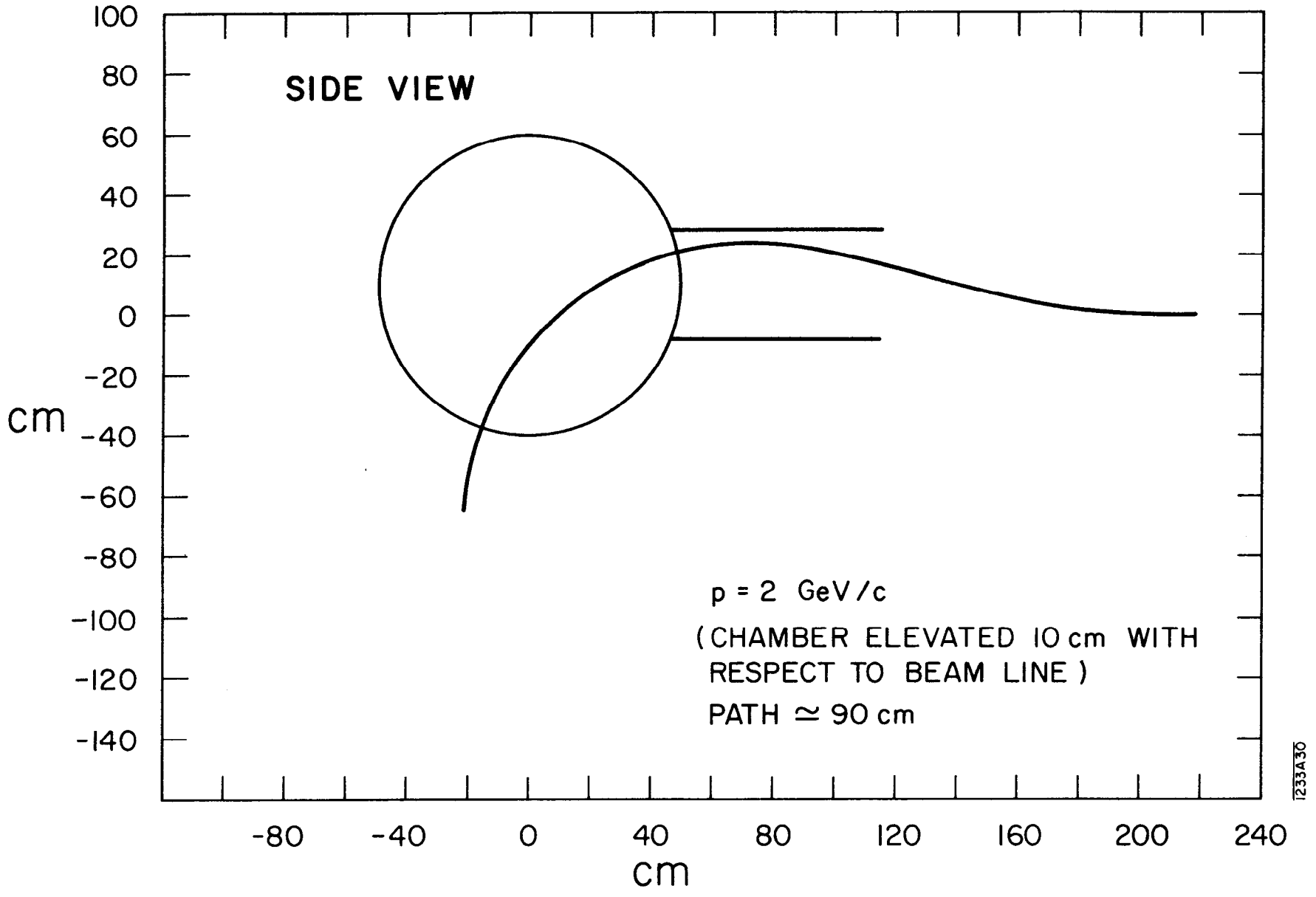

FIG. 2.20--Side view p = 2 GeV/c beam injection (chamber elevated 10 cm with respect to beam line)

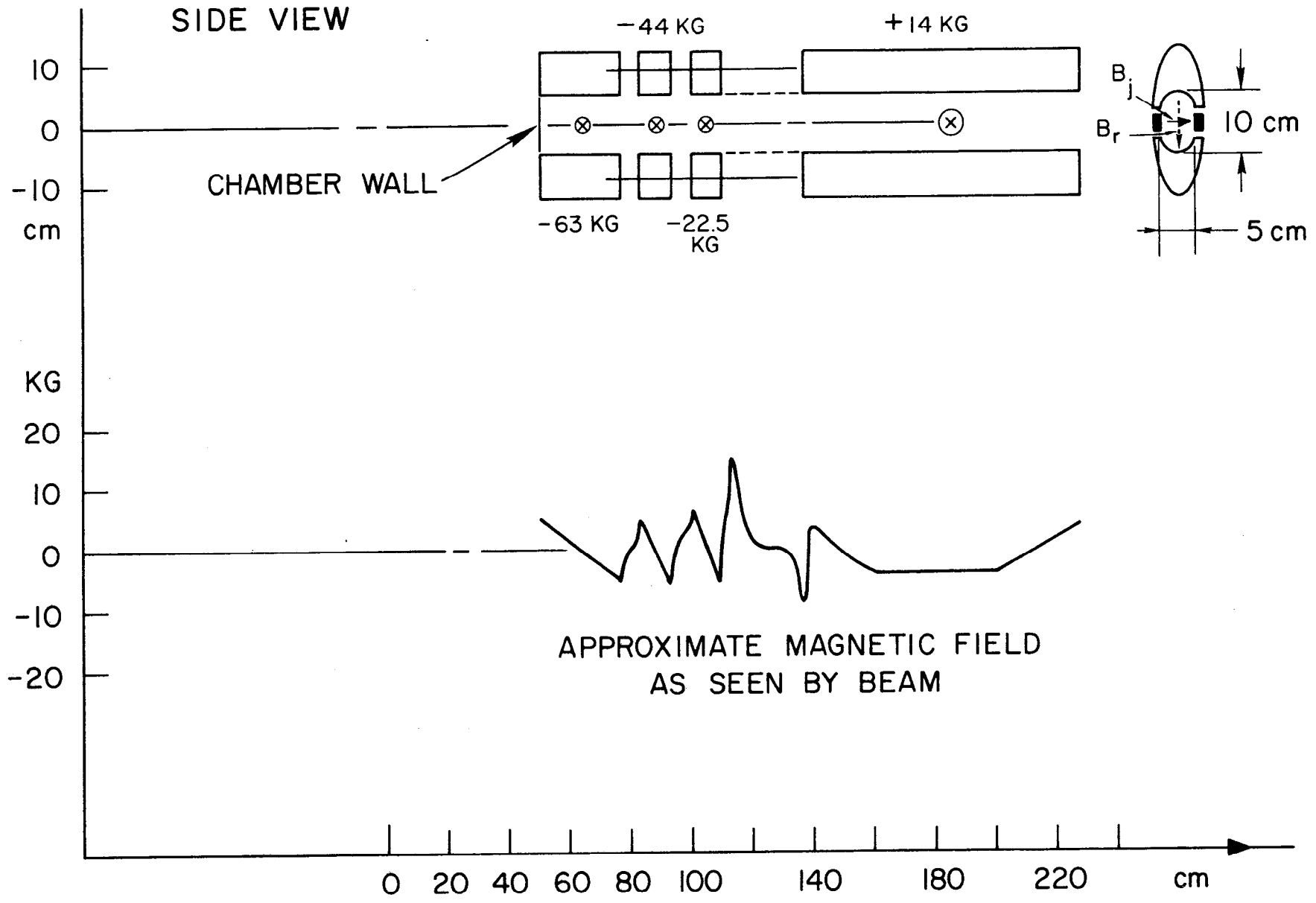

FIG. 2.21--Counteracting magnets in entry slit.

123821

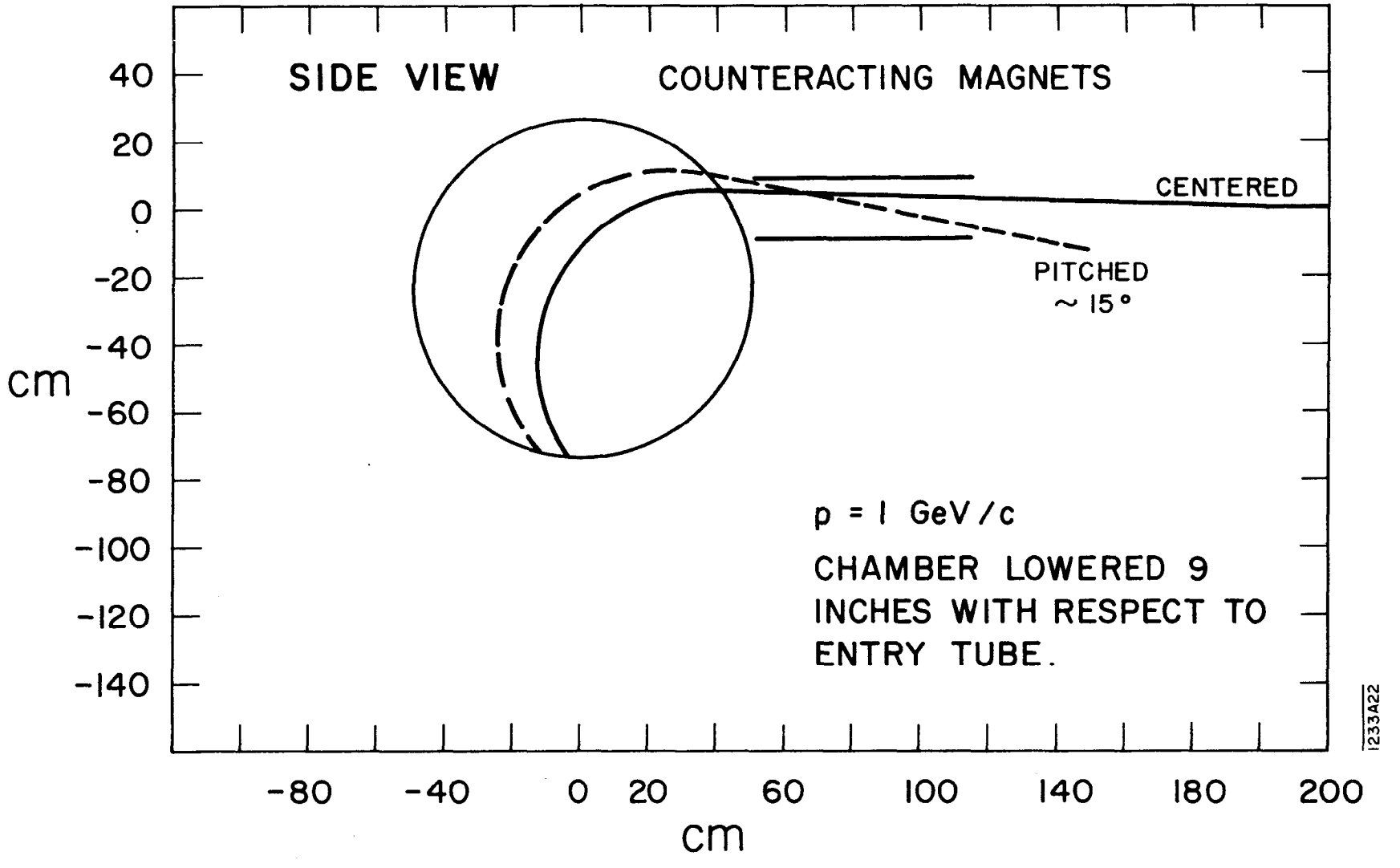

FIG. 2.22--p = 1 GeV/c – counteracting magnets (no shift).

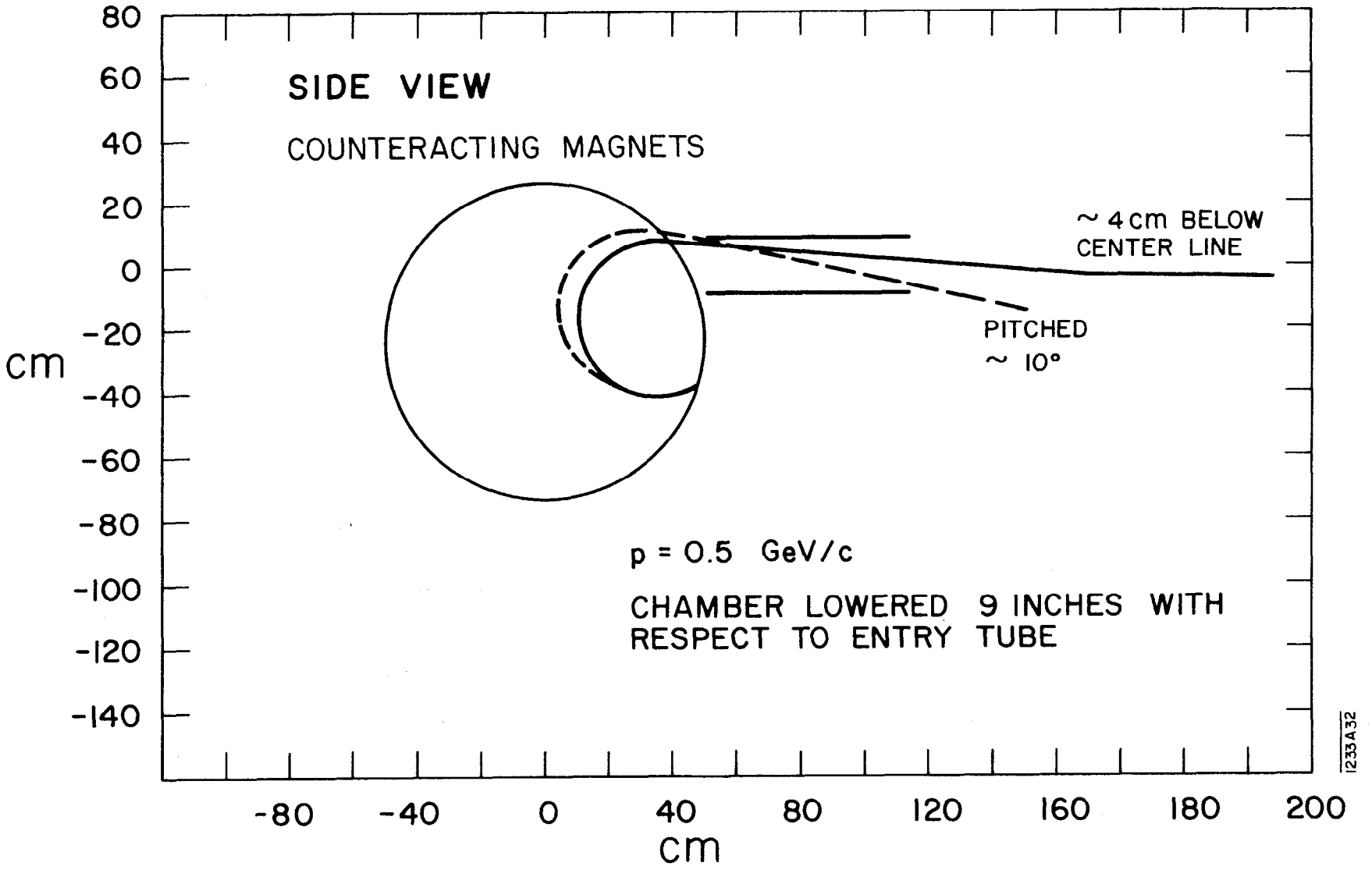

FIG. 2.23--p = .5 GeV/c – counteracting magnets (chamber lowered 9-inches with respect to entry

III. MAGNET SYSTEM

A. General Description

The magnet consists of two vertically oriented superconducting coils surrounded by the existing iron core, which has undergone certain revisions and additions. The coils are made of composite strip material, helically wound into pancakes and convectively cooled by immersion in a helium bath. The magnet has a stored field energy of about 100 megajoules at 2500 amperes. In order to reduce costs, the coil separation has been reduced from 15 inches in the existing magnet to 11 inches. This still allows an unobstructed beam access and egress width of 4". In order to provide room for the installation of particle detectors, an annular space of 3 inches has been left clear around the outside of the chamber.

The basic magnet configuration is shown in Figs. 1.1 through 1.5. Table 3.1 lists the magnet general parameters, and Table 3.2 gives a summary comparison between the existing and proposed magnets. Figures 3.6 and 3.7 show the coil details.

B. General Design Considerations

The following coil design considerations are of primary concern.

1. Internal (Magnetic) Forces

Certain coil inner diameter turns will experience a radial (hoop) force of 1570 pounds per foot due to the 82-kG axial flux component interacting with the 2500-A current. The conductor hoop stress can be maintained within tolerable limits (15,000 psi maximum) by the use of prestressed stainless steel strip interwound between turns, and by the turn-to-turn force distribution resulting from tight winding.

An axial attractive force of 14×10^6 pounds is experienced between coils due to the radial components of the magnetic field. This is supported by the heavy intercoil structure and by surface-oxidized aluminum coil interlayer spacers. These forces and their support are discussed in Section III.C below.

2. Field Uniformity

Calculations indicate that the active chamber field region is uniform within ± 2%. The axial (B_z), radial (B_r) and total (B) field contours are mapped in Figs. 3.1 through 3.4. Figure 3.3 shows the total fringing field of the magnet before, and Fig. 3.4 the field after shielding the fringing field with additional iron plates placed around the core. The field could be reduced using 3 shields from 800 G to 200 G. Further decrease of the fringing field is not required. The field calculations are further discussed in Section III. D below.

3. Coil Stability

The presence of a "region of normality" in which 2500-A current flows in the copper substrate results in a cooled surface heat flux of 0.40 W/cm^2. This heat flux must be transferred to the helium bath by the mechanism of nucleate boiling for coil recovery when the disturbance is past. Published data indicate that this condition can be met for local short-time disturbances.

The heat transfer requirements are closely related to the problem of flux-jumping within the conductor as it is being charged. In order to minimize the possibility of fluxjump instability, a conductor configuration of many fine filaments (250 filaments of 0.007-inch diameter within a conductor cross section of 1/4" × 3/8", with a conductor "twist" of 360^o per three inches of length) is specified, which is within the capability of potential suppliers. Thermal stability also depends upon the effective resistivity of the copper substrate at the temperature, field, and stress to which it is exposed. Hence OFHC copper must be specified, and the hoop stress on the conductor is limited to 15,000 psi or less.

In the event of a long-term disturbance, such as a power failure, refrigeration system breakdown, or internal short due to insulation failure, etc., the coil may quench, in which case a rapid and reliable means of external power dissipation will be provided as described in Section III.F below.

C. Coil Forces

The Lorentz forces ($\vec{F} = Id\vec{\ell} \times \vec{B}$) generated within a high-field superconducting magnet coil must be contained so as to insure structural integrity, dimensional stability and favorable electrical properties within the composite superconductor.

Resistivity vs applied stress tests for $4^{o}K$ copper indicate that below about 18,000 psi, resistivity is almost unaffected, but begins to increase beyond this point.[1] Also, 18,000 psi is about the limit in tension of fully elastic behavior for annealed — 1/4-hard copper at $4^{o}K$.[2] If this limit were exceeded, the coil would suffer creep growth with repeated cycling. Hence, 15,000 psi has been selected as the maximum allowable tensile stress.

The stresses developed within the conductor have three separate origins:

(a) Mechanical stresses during winding due to pretensioning of the stainless steel reinforcing strip.

(b) Thermomechanical stresses due to differential thermal contraction between conductor and reinforcing strip during coil cooldown.

(c) Magnetomechanical stresses due to Lorentz interaction between conductor current and magnetic field. The axial field component produces hoop tensile stress in the conductor while the radial field component produces axial compression within the coil and between the two coils.

Computer programs have been developed to evaluate these stress systems. Figure 3.5 is a plot of the hoop stresses developed within a coil pancake (for 55 turns) subjected to the axial field and reinforcing strip preload scheme indicated. The assumptions and conditions upon which the analysis is based are as follows:

(1) The axial magnetic field decreases linearly from 82 kG at the inner coil radius to -10 kG at the coil OD. This is a close approximation to the maximum peak field condition determined from the NUT-CRACKER program (see Section III.D below).

(2) The coil pancake is assumed to be composed of concentric composite rings (insulation - conductor - reinforcing strip) in intimate contact.

(3) The strengthening effect of the superconducting filaments within the conductor is assumed to result in a modulus of elasticity of $E = 20 \times 10^6$ psi.

(4) Each coil layer is wound upon a stainless steel ring of 3/4 inch effective radial thickness, in order to limit conductor compressive stress during winding, and to insure dimensional stability.

(5) A stainless steel strip pretension scheme was selected which maintains conductor operational resultant hoop stress at less than 15,000 psi, limits conductor winding prestress to less than 15,000 psi, and which results in maintenance of contact between inner ring and inner turn during operation.

The axial compressive loads developed within the coil, due to the radial component of the magnetic field, are transmitted across the layers through radially oriented aluminum-oxide-coated aluminum spacers (see Fig. 3.6). The spacer locations will be closely duplicated from layer to layer, in order that the axial loads be carried in direct bearing through the conductor, rather than generate bending stresses.

The radial field distribution is such that the plane of maximum axial coil pressure occurs about 17 layers from the inside face. Over this plane, the integrated axial pressure varies from 2120 psi at the ID to a maximum of 2600 psi at turn 25, diminishing to 1900 psi at the coil OD. For interlayer spacer bearing over one-eighth of the projected area, the resultant maximum bearing stress is 20,800 psi.

The maximum resultant hoop stress of 13,800 psi generated by the direct radial loads (Fig. 3.5) occurs at the OD , also in the region of the maximum axial pressure plane (layer 17), at which point the axial compressive stress beneath the spacers is $1900 \times 8 = 15,200$ psi. The degrading effect of this transverse bearing stress upon the copper resistivity must be investigated.

D. Magnetic Field

The magnet is designed for 1.30×10^7 ampere-turns to generate a central field of 70 kG. A maximum field of 82 kG is generated within the coils at their inner diameter.

The field data, including that for Figs. 3.1, 3.2, and 3.3 were generated by the SLAC computer code NUTCRACKER.[4] This program solves variable permeability, two-dimensional axial symmetric magnetostatic problems by solving the quasi-Poisson equation,

$$\nabla \times \frac{1}{\mu} \nabla \times \vec{A} = -J$$

where

J = current density

$\vec{A}$ = magnetic vector potential

μ = permeability

by successive over-relaxation of the magnetic vector potential $\vec{A}$ and under-relaxation of the permeability in iron.

E. Coil Stability

Coil thermal stability is a design consideration involving judicious choice of conductor properties, current density, and coil geometry, all set against the degree of stabilization considered adequate.

The radial space limitations imposed upon the coil by the existing chamber and magnet iron and by the addition of a helium dewar and particle detector space, and the magnet operation requirement of 1.30×10^7 ampere-turns are the primary factors leading to the 2500-A/cm^2 overall current density.

When a reasonable allowance is then made within the coil volume for coolant passages, stainless steel reinforcing strip, and insulation, the resultant current density within the copper conductor portion is 5370 A/cm^2. This and the maximum axial magnetic field (82 kG) then lead to selection of the minimum amount of superconductor required.

Work by Smith[5] of the Rutherford High Energy Laboratory, and others, indicates that the imbedment of many fine superconducting filaments in the copper substrate and "twist" of the filament pattern are effective means of minimizing the problem of "fluxjumping" during magnet charging or field change. For this reason, 0.007" diameter filaments (250 twisted filaments per conductor) have been selected.

The orientation of the coils within the liquid helium dewar favors the use of the vertical layer faces (conductor edges), rather than the turn-to-turn conductor horizontal sides, for convective cooling. This, plus the high radial forces to be borne by the turns, has resulted in a proposed pancake design with edge-cooling only. Hence, in order to achieve a favorable cooled surface-to-area ratio, a nearly square conductor design was chosen (3/8" wide × 1/4" high) with a

semi-circular scallop on both cooled edges. The latter feature also serves to reduce the conductor surface hidden beneath the interlayer spacers and to allow convective coolant flow across such spacers.

To determine the optimum current density, we utilize several stability criteria commonly used in superconducting magnets.

The first criterion is based on the assumption that when a local region of normality is produced within the coil, say by means of a disturbance such as a fluxjump, the current flowing through the superconductor is diverted to the normal substrate — in our case, the copper matrix. The region of normality is not spread along the conductor as long as the maximum heat flux generated by the Joule heating of the normal metal is less than the local limit of nucleate boiling. The heat flux $h\Delta T$ is given by:

$$h\Delta T = \frac{I^2 \rho_n}{A_n P} < (h\Delta T)_{NB} \qquad (W/cm^2) \qquad (E.1)$$

where:

I = conductor current = 2500 amperes maximum

ρ_n = copper resistivity at 4.3° K and maximum field expected
= 4.2×10^{-8} ohm · cm at 4.3° K and 82 kG (based upon data from Ref. 2, Figs. 3.4 and 3.5, for residual resistivity ratio of 150:1 and magneto resistance ratio of 3.6:1)

A_n = net cross section of the normal metal
= $0.466\ cm^2$

P = cooled conductor surface per unit length (or cooled perimeter of cross section). (For 25% projected area coverage of a layer face by interlayer spaces, only 1/8 of the conductor area is covered by the spacers.)
= $1.43\ cm^2/cm$

$(h\Delta T)_{NB}$ = nucleate boiling heat flux

With these data, we get

$$h\Delta T = \frac{(2500)^2 \times 4.2 \times 10^{-8}}{0.466 \times 1.43} = 0.394 \text{ W/cm}^2 \quad .$$

The open bath heat flux for cooling vertical surfaces by nucleate boiling of liquid helium is $0.6 - 0.78$ W/cm^2.

Whetstone and Boom[6] performed nucleate cooling limit tests on small coils (2" ID , and 10" × 10" cross section) using round 0.06" diameter stabilized cables. For a 0.067" conductor spacing for cooling purposes, the heat flux limit was found to be 0.63 W/cm^2. Experiments performed by Wilson at Rutherford[7] on cooling flux limits in narrow vertical channels (0.025 - 0.165 cm wide) indicate that for small channel heights (to 5 cm or so) and a 0.43-cm channel width, the critical heat flux would approach the 0.78 W/cm^2 open channel value. Hoag[8] reports a maximum nucleate boiling flux of 0.7 W/cm^2 for a 0.36-cm wide channel, 2.5 cm high.

Another criterion, the so-called minimum propagating current in a composite conductor, is reported by Williams.[9]

The minimum propagating current is given by the expression:

$$\frac{I_m}{I_c} = \frac{A_n}{2A_c} \left\{ \left(1 + \frac{8A_c}{A_n} \right)^{1/2} - 1 \right\} \qquad \text{(E.2)}$$

where

I_c = short-sample critical current = 2800 A @ 82 kG

= (based upon a critical current density (J_c) of 5×10^4 amp/cm^2)

A_c = cross section of normal material to stabilize I_c

$$A_c = \frac{I_c^2 \cdot \rho_n}{(h\Delta T) \cdot P}$$

$$= \frac{(2800)^2 \times 4.2 \times 10^{-8}}{0.4 \cdot 1.43} = 0.575 \text{ cm}^2$$

A_n = copper area of proposed conductor

$= 0.466 \text{ cm}^2$.

Thus:

$$I_m = \frac{2.8 \times 10^3 \times 0.466}{2 \times 0.575} \left[-1 + \left(1 + \frac{8 \times 0.575}{0.466}\right)^{1/2}\right]$$

$= 2600 \text{ A} > I_{\text{nominal}}$

Both of the above criteria are based upon the preservation of stability following short term local disturbances.

A third criterion for stability is the limiting of thermal excursions resulting from disturbances of sufficient power and duration to result in a localized loss of helium cooling.

In order to prevent thermal and thermal stress damage to the conductor and insulation, it is necessary to limit the temperature to some maximum value T_m. This is achieved by provision of adequate substrate material and by a protection system such as that proposed in Fig. 3.6.

Let us calculate the current density, J_{opt}, which would, in case of such an excursion, produce a temperature $T \leq T_m$ and a voltage $V \leq V_m$. Neglecting the heat conduction and taking advantage of the fact that $A_n > A_{sc}$, we have:

$$\int_0^{J_m} \frac{J_n^2 \rho_n \, dt}{\rho_n} = \int_{T_b}^{T_m} f(T) \, dT \qquad \text{(E.3)}$$

where,

$$f(T) = \frac{C_n \delta_n}{\rho_n}$$

with: T_b = bath temperature

C_n = specific heat of the copper substrate

δ_n = density of the substrate

ρ_n = resistivity of the substrate

J_n = the current density in the substrate

J_m = Im/Am .

Referring to Fig. 3.6, when a region of normality appears in the coil, a voltage will appear across the magnet terminals. If this voltage exceeds a preset voltage, the switch S_1 closes, the switch S_2 opens and the current flows through the low-ohm shunt resistance, R_1. If the terminal voltage continues to rise, indicating that R_1 is inadequate, then the switch S_1 reopens and the total energy is dissipated in R_2. Now this current decays according to a time constant

$$\tau = \sum_{i=1}^{n} L_i/R_i \qquad (i = 1, 2 \ldots) \ .$$

From Eq. (E.3), we get:

$$J_n^2 \tau/2 = \int_{T_b}^{T_m} f(T)\, dT = F(T_m) \qquad (E.4)$$

Replacing τ by the inductance L_i and the resistance R_i, and using the expressions for energy $E = \frac{1}{2} I^2 \Sigma L_i$; the voltage $V_m = I \Sigma R_i$; and inserting it into Eq. (E.4), we get:

$$J_n \left\{ \frac{F(T_m) \cdot V_m I_m}{E} \right\}^{1/2} \qquad (E.5)$$

with

$$F(T_m) = \int_{T_b}^{T_m} \frac{C_n \cdot \delta_n}{\rho_n} dT$$

The higher the $F(T_m)$, the less amount of normal metal is needed to protect the coil. Copper used for the magnet has a low heat capacity at He temperature. We chose for our magnet $T_m = 200^{\circ}$ K. Integrating $C_n \delta_n / \rho_n$ for copper, we get $F(T_m) = 1.2 \times 10^9$ amp^{2}sec/cm^4. The magnet has a field energy of 10^8 joules. We chose the shunt resistance R_2 such that $V_m \leqq 1.5 \times 10^3$ volts. Thus we get from Eq. (E.5) for $I_m = 2500$ A:

$$J_n \leqq 6.7 \times 10^3 \text{ amp/cm}^2 \quad .$$

The maximum current density in the chosen conductor is $J_n = \frac{2500}{0.466} = 5300$ amp/cm^2. To find the optimum current density in the substrate, we combine Eq. (E.5) and Eq. (E.1) in the following way:

Stabilization criterion

$$J_n^2 \leqq h\Delta T \cdot P \frac{1}{A_n} \cdot \frac{1}{\rho_n} \qquad (E.1)$$

Protection criterion

$$J_n^2 \leqq f(T_m)\, V_m \cdot \frac{I_m}{E} \qquad (E.5)$$

Combining the cooled surface per unit length P and the cross section of the normal material A_n we define f as:

$$f = \frac{\rho_n}{\sqrt{A_n}}$$

and eliminating I as an independent variable, we get

$$J_{opt} = \left(\frac{h\Delta T \cdot f}{\rho_n}\right)^{0.4} \cdot \left(F(T_m)\, V_m/E\right)^{0.2} \qquad (E.6)$$

For our conductor, $f \cong 2$; $h\Delta T = 0.4$ W/cm^2; $\rho_n = 4.2 \times 10^{-8}$ ohm · cm; $F(T_m) = 1.2 \times 10^9$ A_s^2/cm^4; $V_m = 1.5 \times 10^3$ volts; $E = 10^8$ joules, and we have

$$J_{opt} = \left(\frac{0.4 \times 2}{4.2 \times 10^{-8}}\right)^{0.4} \cdot \left(1.2 \times 10^9 \times 1.5 \times 10^3/10^8\right)^2$$

$$= 5788 \text{ amp/cm}^2$$

which is higher than the nominal current density J_n .

In order to further enhance coil performance we propose to use conductors with many fine imbedded superconducting filaments, which P. Smith[5] and others have shown to be a basic means of reducing fluxjump instability.

In fact, they have shown that an "intrinsically stable" composite superconductor can be produced if the individual superconductor filaments are of a diameter determined from the following relation (Ref. 5, Eq. 3).

$$d_f^2 < \left(T_0 \cdot \frac{k_s}{\rho_n}\right)\left(\frac{1}{J_m \cdot J_c}\right) \qquad (E.7)$$

where

$T_0 = J_c/\left(-\frac{dJ_c}{\partial T}\right)$ (usually about $T_c/2$) $\cong 5^{\circ}$K

k_s = thermal conductivity of the superconductor

$= 1.2 \times 10^{-3}$ W/cm $^{\circ}$K

J_m = overall current density in the composite conductor

$= 5360$ amp/cm^2

J_c = critical current density in the filaments

$= 5 \times 10^4$ amp/cm^2 at 82 kG

Thus:

$$d_f < 2.3 \times 10^{-2} \text{ cm}$$

Tests indicate that, in fact, "intrinsic stability" can be obtained without twist (see below) if the filament size is not greater than about .003 inches. Smith further states that intrinsic stability may also be achieved if the filament diameter

$$d < 1500/J_c \quad (d < .010 \text{ inches for our design})$$

and the conductor is twisted with a pitch (ℓ_c) where:

$$\ell_c^2 \leqq \left(10^8 \lambda J_c d_f \cdot \rho_n / \frac{dH}{dt}\right)^{1/2}$$

where:

λ = fraction of conductor parallel to the field occupied by the filaments, $\cong 0.3$

$J_c = 5 \times 10^4$ amp/cm^2

$d_f = 1.77 \times 10^{-2}$

$\frac{dH}{dt} = 10$ G/sec (total charging time of 2 hours minimum.)

Thus:

$\ell_c \cong 11$ cm

Note: The twisting is a technique for limiting the magnetization currents which will flow within and between the parallel filaments during magnet charging.

We therefore propose to specify conductor with .007-inch diameter filaments and a twist of once per three inches of conductor length in order to approach the conditions of intrinsic stability. A minimum changing time of 2 hours would be required. Alternatively, conductors with ~ .002-inch filaments and no twist would be acceptable. The final choice of filaments size and/or twist will be based upon manufacturers demonstrated capabilities.

F. Coil Protection and Instrumentation

Field or current disturbances, which may produce fluxjumps and thus local heating in the conductor, are generated externally from the current source, conductor movement due to thermal and magnetic stresses or other unforeseen reasons.

A region of normality caused by a disturbance of short duration is self-healing due to the fact that a stable superconductor has been selected for the present magnet. If, however, the disturbance is long-lasting, such as in case of power failure or if the refrigeration system is not performing adequately, or in terms of suddenly occurring internal short circuits, the region of normality may propagate along the conductor and lead to a coil quench.

With a choice of conductor and cooling scheme, the above may be improbable, but suggests that safety precautions be taken, which should:

(a) Monitor and sound alarm systems.

(b) Shut the power source off from the coil or reduce the current slowly until the superconducting stage is re-established.

(c) Dump the helium liquid or gas into external containers.

(d) Prevent, in case of a quench, the internal voltage from exceeding certain specified values.

When a coil quenches, the energy is dissipated into an external shunt connected to the coil permanently, as described by Brechna et al.[10] The external resistance is chosen such that the maximum terminal voltage does not exceed 1500 volts to ground. To eliminate surge voltages internally, double pancakes are wound with two conductors in parallel and interleaved, to reduce interturn capacity.

The reduction of current in the coil will be in two ways (Fig. 3.5):

(1) In case of a sudden quench, the switch S_1 will open within milliseconds, dissipating the entire field energy to the external shunt. With this scheme, the energy dissipation is completed within the time constant of the coil and shunt system which is a few seconds. More than 98% of the field energy is dissipated externally and not in the coolant. The temperature of the coil may rise a few degrees, but can be limited below the critical temperature of the superconductor. After the disturbance or failure has cleared,the coil can be charged within a specified time and normal operation resumed.

(2) The power supply, an SCR regulated rectifier type (3000 A, 25 V dc), is equipped with shunt diodes connected to the coil terminals. In case of a power failure, the magnetic field energy is dissipated into the external shunt slowly. The coil does not quench in this case.

To monitor disturbances, each pancake is equipped with sensing leads and the coil is equipped with a field sensor. Current is reduced or interrupted if the disturbance lasts longer than a specified time, or the voltage built up across each pancake exceeds preset values.

The liquid level in the dewars controls the refrigerator liquefaction rate in order to maintain a constant helium inventory.

The coil current leads are helium cooled. The power requirement at 6000 A is less than 30 W for both leads. Voltage drops along the leads are measured at various points to insure proper performance. The magnet current will be measured by a conventional shunt at the current supply.

Voltage across each coil section and across each joint will be measured continuously and monitored. The temperature at various points of the coil will be measured continuously and recorded.

Field probes will be located at the outer coil diameter at specified intervals to provide field symmetry information and monitor any failure.

G. Coil Fabrication

The pancake is the basic manufacturing unit of the coils. Each pancake (Fig. 3.7), with an inner conductor diameter of 58.0 inches, outer diameter of 92.5 inches, and height of 0.919 inch, consists of two toroidally-wound layers of 60 turns each. Each layer is wound upon a separate stainless steel ring (see Section III.C, above), and separated from the adjacent layers by a radial pattern of .169" thick aluminum spacers, to provide interlayer (edge) cooling. The spacers must be laid down and glued in place with a keyed metal template in order to insure that each succeeding interlayer pattern is identical.

Potential suppliers indicate that 1200 feet may be the maximum continuous length which can be supplied. The total conductor length of one pancake is 2360 feet (less leads). Therefore, in order to avoid internal splices, a bifilar winding arrangement is indicated.

Each of the two coil assemblies (Fig. 3.8) consists of 22 pancakes clamped together between two endplates by an OD and ID pattern of bolts to form a rigid and handleable unit after completion of inter-pancake splices but prior to installation into the dewar. Each stainless steel ID layer ring has a hole pattern to allow passage of the bolts. Standoff washers are provided between the rings at each bolt location in order to insure 0.169 inch interlayer spacing and to key the pancake stack axially and rotationally. The ID of each layer ring is scalloped to permit axial flow of helium, but otherwise fits snugly over the dewar inner wall in order to insure axial coil location and support.

It appears desirable to wind one entire coil assembly in situ: That is, one endplate is first laid upon the winding table and each succeeding pancake wound atop the last. Finally, the top endplate is placed on the stack and bolted to the bottom endplate before removal from the table of the 20,000-pound unit.

Figure 3.9 shows the proposed coil-winding setup, using a surplus Navy 5"/38 single gun mount base as the turntable.

H. Magnet Core

The existing 240-ton magnet core will be modified to accommodate the proposed conversion. Although most of the iron becomes saturated, it still contributes about 8% of the total field, acts as a mechanical support structure, and shields the nearby equipment and instrumentation from large stray fields.

About 16" (20 tons) of ASTM A273 forgings will be added to the magnet core stationary (expansion) half and about 4" (5 tons) of steel will be added to the magnet core moveable (camera) half.

Four new tiebolts of 3-1/4" diameter and increased length will replace the existing ones. About 24 1-1/2" diameter holes will be drilled and tapped into the magnet iron for the coil assembly and vacuum tank support bolts.

Although not indicated in the drawings, a two-layer sandwich of 2" thick steel plates will be placed over the existing iron surfaces at the camera, expansion, and beam exit ends and the top in order to reduce the fringing field. The anticipated cost of this iron and its installation, including such replumbing and relocation of other components as may be required, is given in Section X.

I. Field Mapping

The active chamber volume will be mapped on a nominal 2-inch grid spacing, using a cylindrical coordinate device capable of θ and Z motion. Approximately 10 detectors will be placed along the radial arm, instead of using a single indexed carriage.

Each detector will be an orthogonal triplet of Hall probes. Integrating coils will be included in several moving locations and a number of fixed detectors will be located in otherwise inaccessible chamber areas.

The axial shaft, capable of θ and Z manual operation, will penetrate the central vacuum tank camera port through a vacuum gland, and be supported and located radially by a bearing attached to the chamber 40" window flange by radial spokes.

A light stabilizing bearing related to the chamber fiducials will be located at the piston end of the main shaft.

The field plot will be made relative to magnet fiducials mounted on the iron outside surface.

Table 3.1

General Magnet Parameters

Central field		70 kG
Peak field at windings		82 kG
Total ampere-turns		1.3×10^7
Overall current density		2500 A/cm^2
Total stored energy		100 MJ
Total inductance		32 H
Coil inner diameter		58 in (147 cm)
Coil outer diameter		92.5 in (235.0 cm)
Coil axial separation		11 in (28 cm)
Coil current		2500 A
Number of coils		2
Number of pancakes per coil		22
Number of layers per pancake		2
Number of turns per layer		60
Layer (conductor) axial width		.375 in (.952 cm)
Layer axial separation		.169 in (.43 cm)
Turn radial height:		
Conductor	.250 in (.635 cm)	
SST strip	.025 in (.051 cm)	
Insulation	.010 in (.025 cm)	
		.285 in (.725 cm)
Total conductor length		106,000 ft (32,400 m)
Total conductor weight		38,600 lb (17,500 kG)
Coil materials:		
Conductor substrate		Copper, OFHC
Superconductor		Nb(60%)Ti in 0.007-in diameter filaments
Reinforcing strip		Stainless steel type 304
Turn insulation		B-stage epoxy-fiberglass
Layer insulation		Anodized aluminum
Number of NbTi filaments per conductor		250
Copper-to-NbTi ratio by area		7.5:1
Designed local heat flux		~ 0.4 W/cm^2
Axial compressive force between coils		14×10^6 lb
Maximum allowable conductor tensile stress		15,000 psi

Table 3.2

Comparison between main parameters
of the SLAC water-cooled and superconducting
Bubble Chamber magnet

	Existing Conventional water-cooled	Proposed Superconducting conversion
Central field	26	70
Peak field at conductor	30	82
Total ampere-turns (A)	3.52×10^6	1.30×10^7
Overall current density (A/cm^2)	4.65×10^2	2.5×10^3
Coil current (A)	10^4	2.50×10^3
Coil voltage (V)	284	25(1)
Power (W)	2.84×10^6	2.20×10^5 (2)
Coil inner diameter (m)	1.37	1.47
Coil outer diameter (m)	2.82	2.35
Axial length of each section (m)	0.378/0.66	0.61
Axial coil separation (for beam window) (m)	0.381	0.29
Field energy (Mjoules)	13	98
Axial compressive force between coil sections (kg)	1.1×10^6	6.4×10^6
Hoop stress on conductor (kg/cm^2)	2.52×10^2	1.06×10^3

(1) 25 volts dc are used for accelerating magnet charging, which can be accomplished in 24 minutes.

(2) The power requirement includes the refrigeration system outlined in Section 8.

REFERENCES

1. H. Brechna, "Materials in Electromagnets and Their Properties," (Fig. 18), Report No. SLAC-PUB-320, Stanford Linear Accelerator Center, Stanford University, Stanford, California (1967).
2. Cryogenic Materials Data Handbook, National Bureau of Standards, Cryogenic Laboratory, PB171809, Fig. F.1.a of 7-64 supplement.
3. H. Brechna et al., "A 30-cm Bore 70-kG Superconducting Helmholtz Magnet," Report No. SLAC-PUB-337, Stanford Linear Accelerator Center, Stanford University, Stanford, California (1967).
4. E. A. Burfine, L. R. Anderson, and H. Brechna, "A Computer Code for Variable Permeability Magnetostatic Field Problems," Report No. SLAC-56, Stanford Linear Accelerator Center, Stanford University, Stanford, California (1966).
5. P. F. Smith et al., "Intrinsically Stable Conductors," Report No. RHEL RPP/A43 (1968).
6. C. N. Whetstone and R. W. Boom, "Nucleate Cooling Stability for Superconductor Normal Metal Composite Conductors in Liquid Helium," Paper No. B6, Advances in Cryogenic Engineering, (Plenum Press, New York, 1968); p. 68.
7. M. N. Wilson, "Heat Transfer to Boiling Liquid Helium in Narrow Vertical Channels," Paper No. II-2, IIR Commission 1 Meeting (June 1966).
8. E. Hoag, "Experimental Investigation of Advanced Superconducting Magnets," Annual Report No. NAS 8-5279, Avco-Everett Research Laboratories, Everett, Massachusetts (1966).
9. J.E.C. Williams, Phys. Letters 19, 96 (1965).
10. H. Brechna et al., "Energy Dissipation From Large Superconducting Magnets," Report No. SLAC-TN-68-10, Stanford Linear Accelerator Center, Stanford University, Stanford, California (1968).

11. Z.J.J. Stekly, Avco Report No. AMP 271 (1968).

12. H. Brechna, "A High Field 1.3-m Superconducting Split Coil Magnet With Forced Liquid Helium Cooling," Report No. SLAC-PUB-182, Stanford Linear Accelerator Center, Stanford University, Stanford, California (1966).

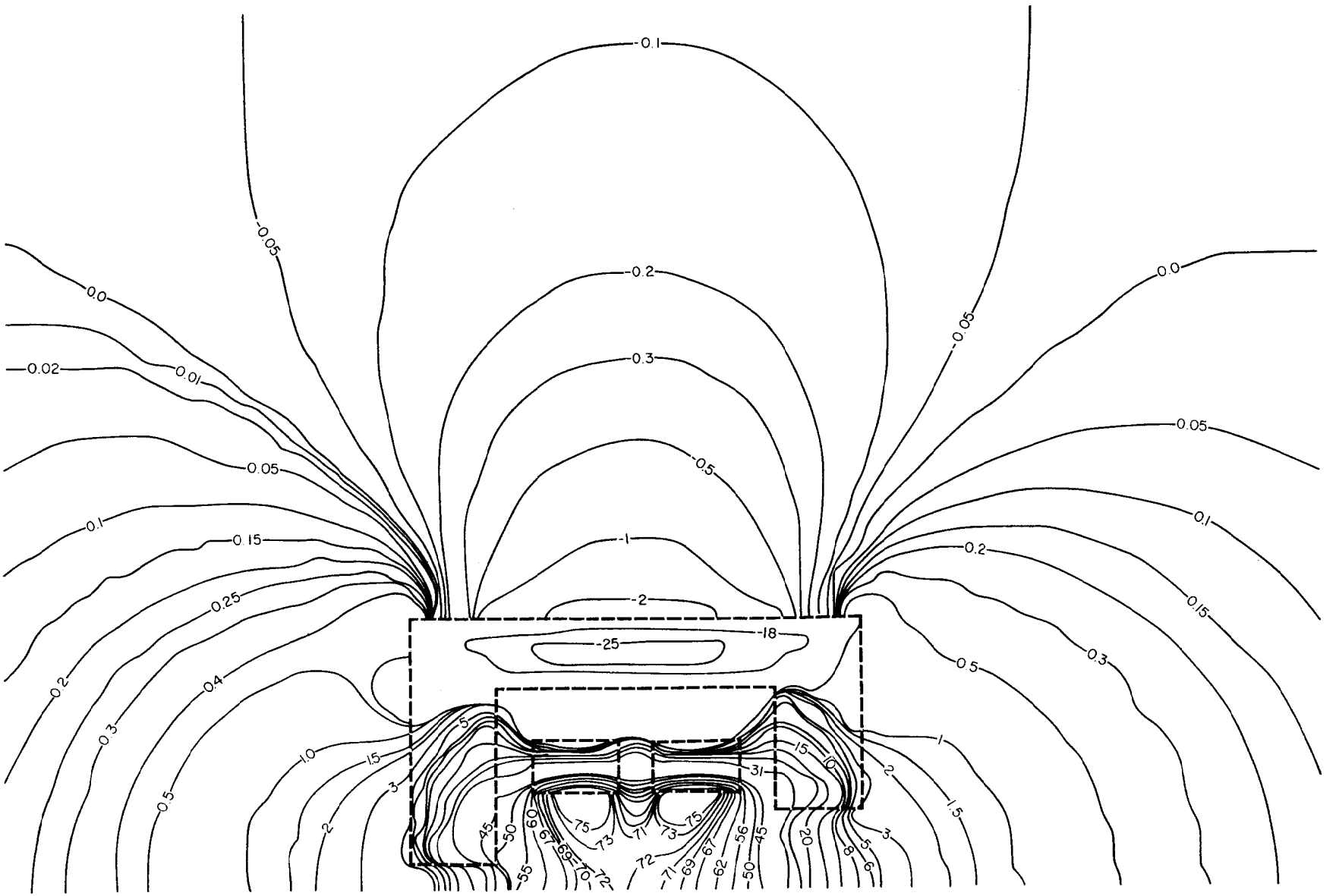

FIG. 3.1--Axial field plot (B_z) kG with no shields around the magnet.

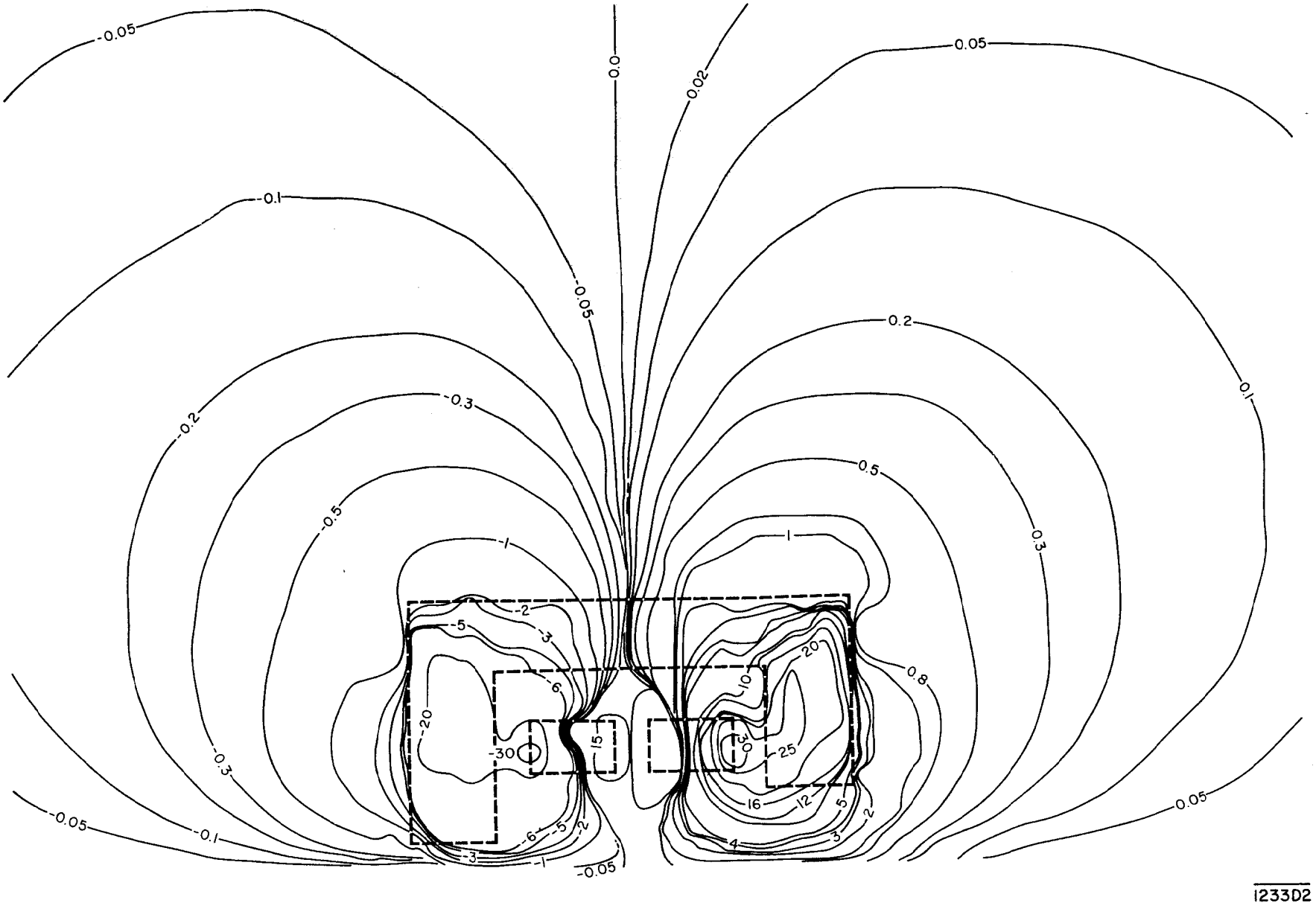

FIG. 3.2--Radial field plot (B_r) kG with no shields around the magnet.

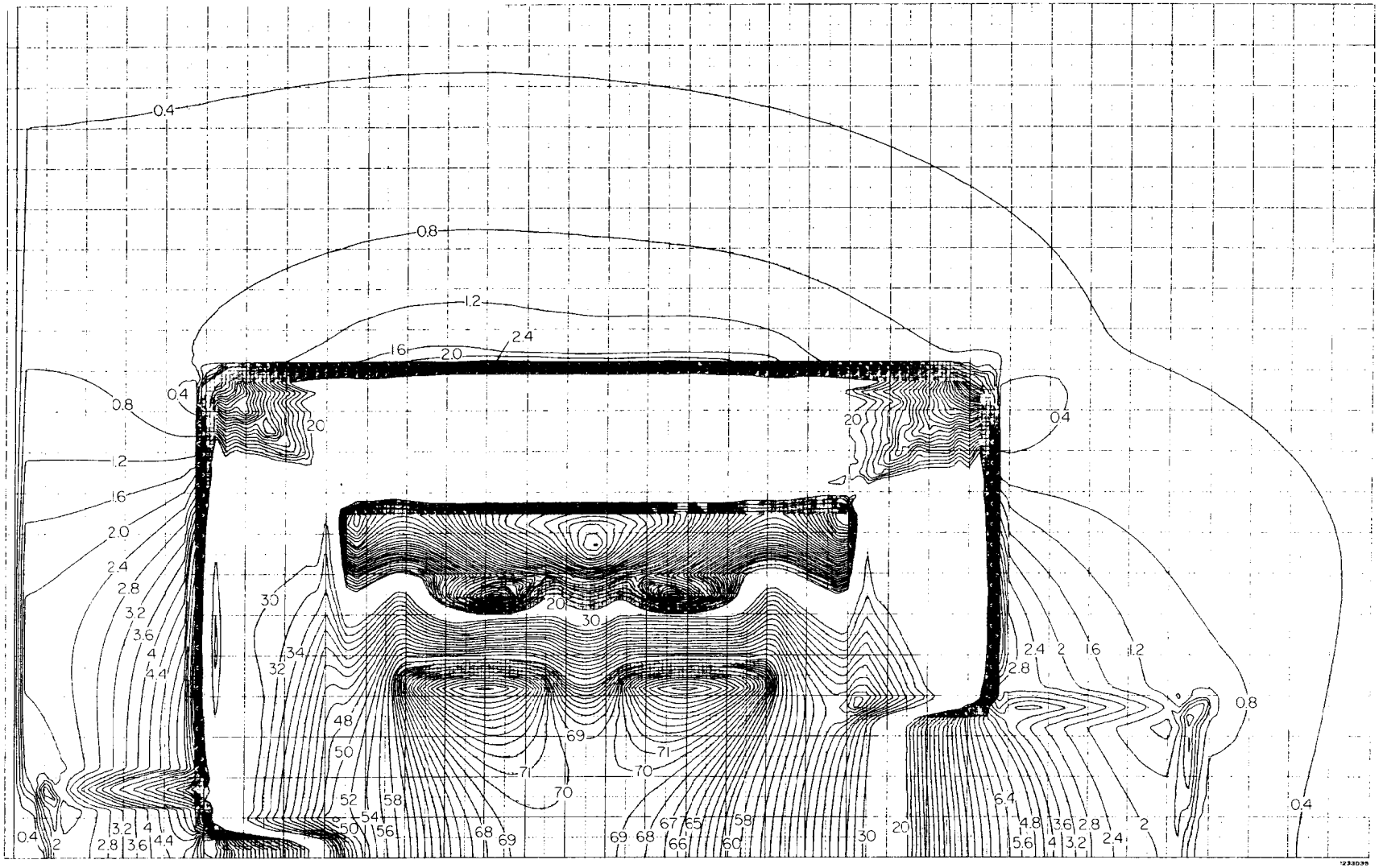

FIG. 3.3--Total field (kG) distribution without iron shields.

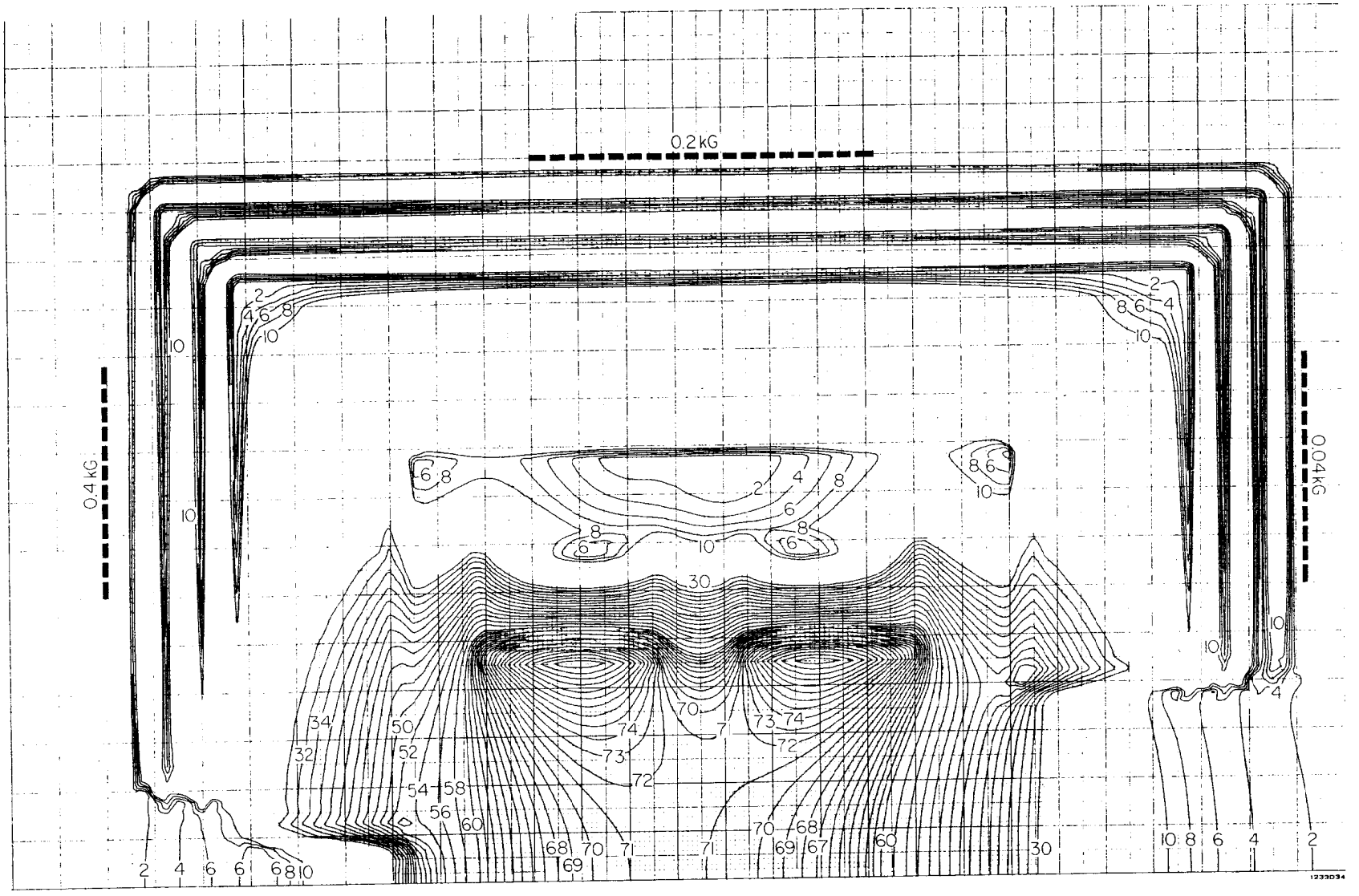

FIG. 3.4--Total field (kG) distribution having iron shields around the magnet.

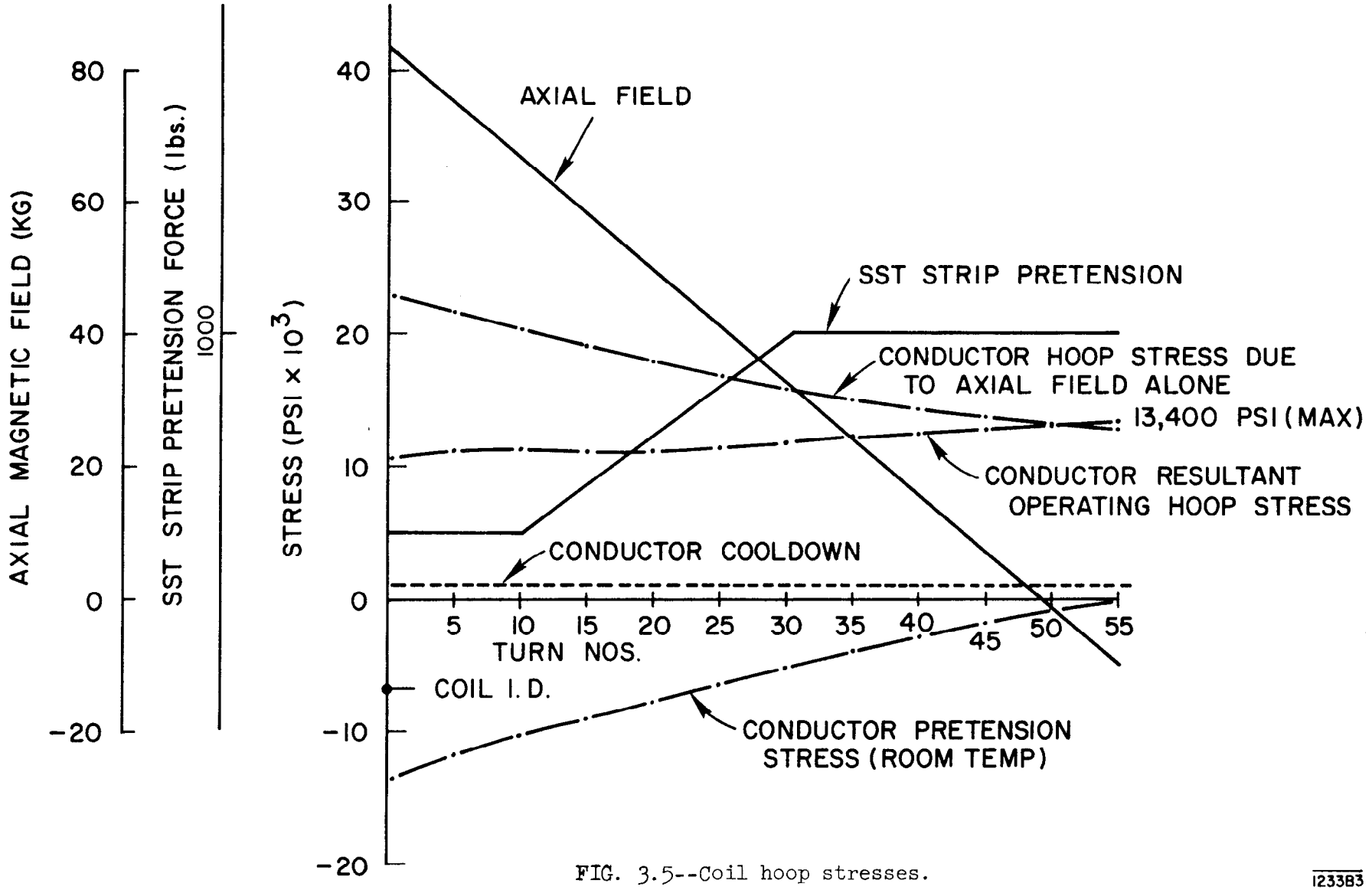

FIG. 3.5--Coil hoop stresses.

123383

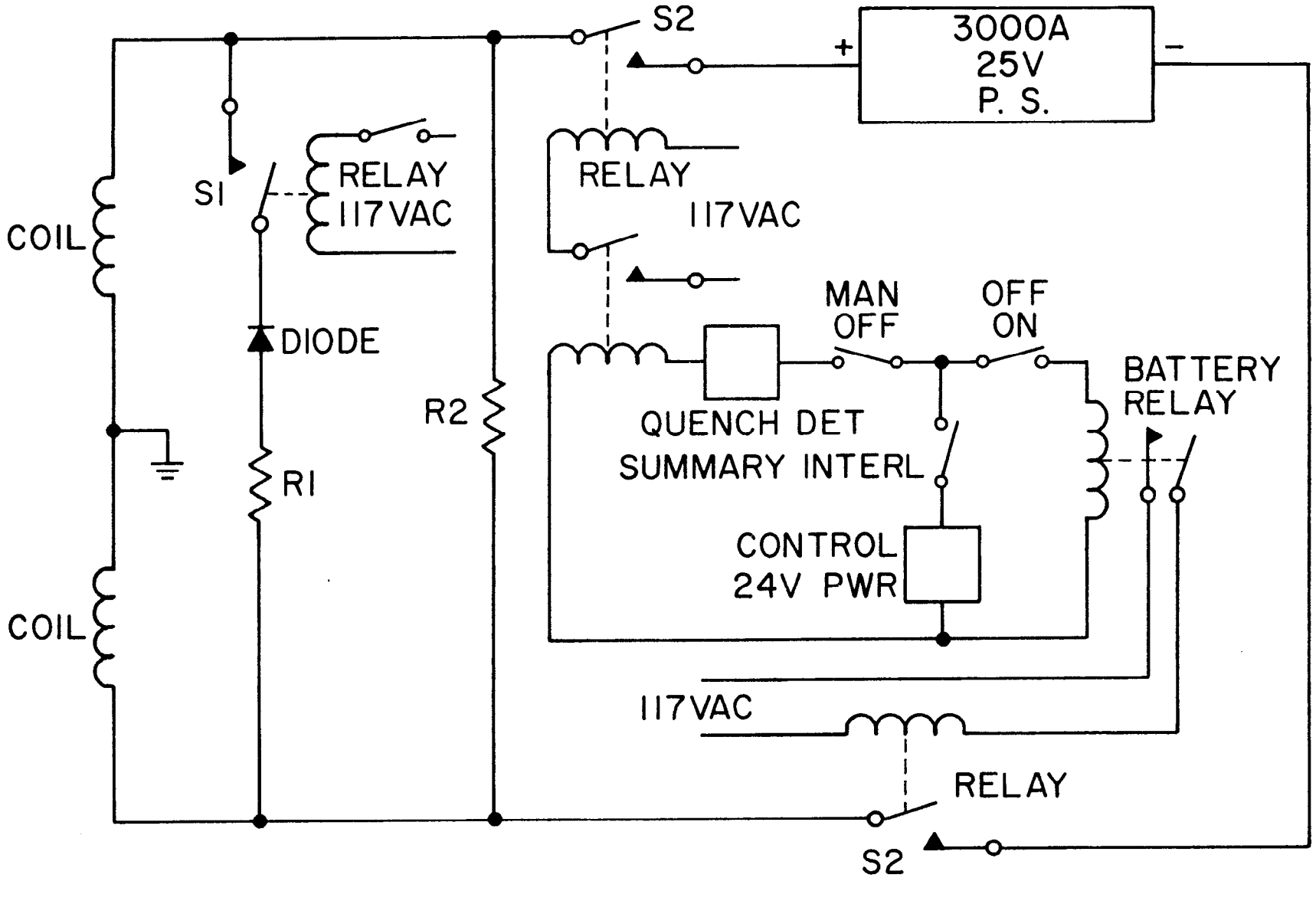

FIG. 3.6--Magnet protection system.

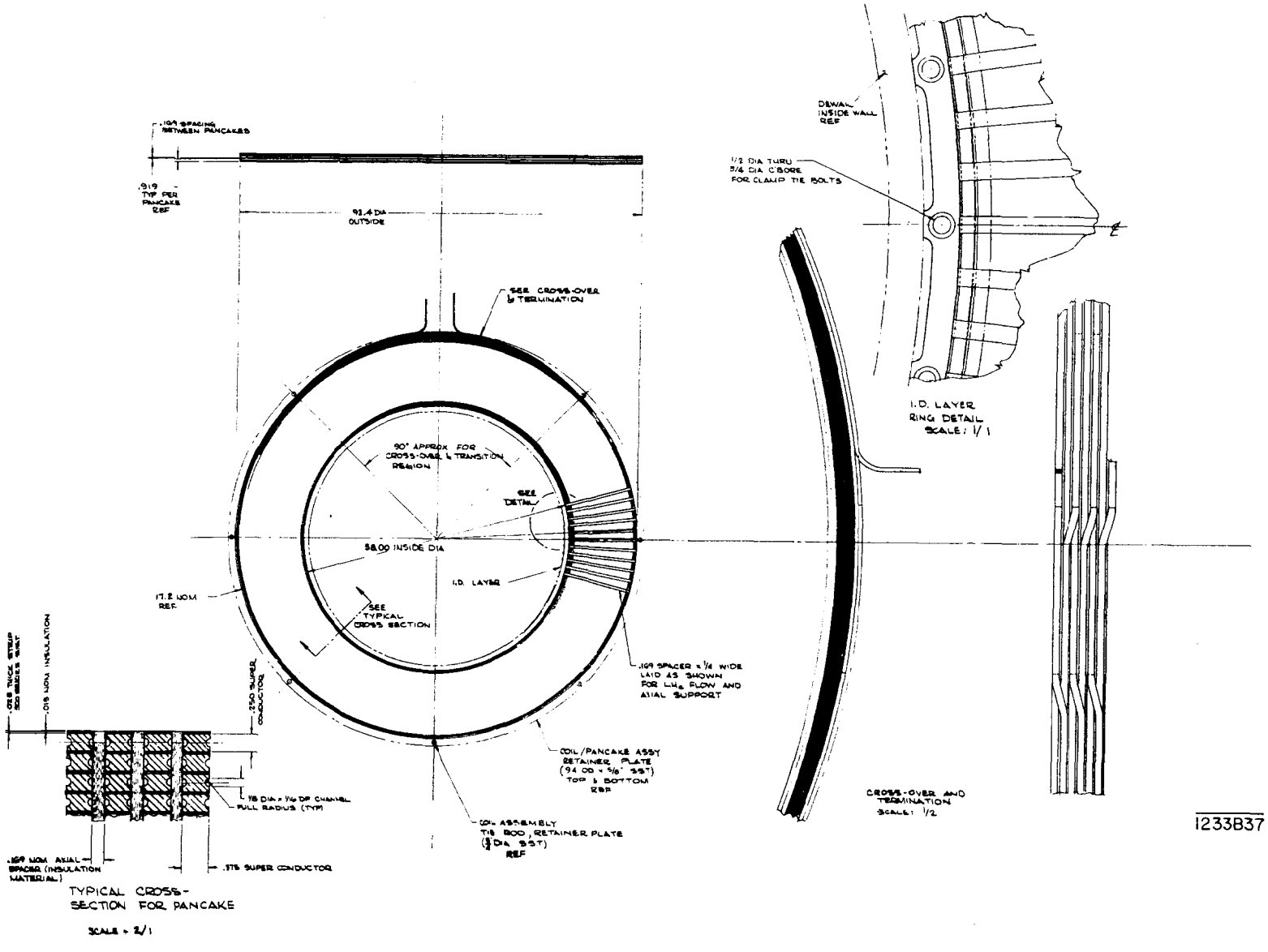

FIG. 3.7--Coil pancake detail.

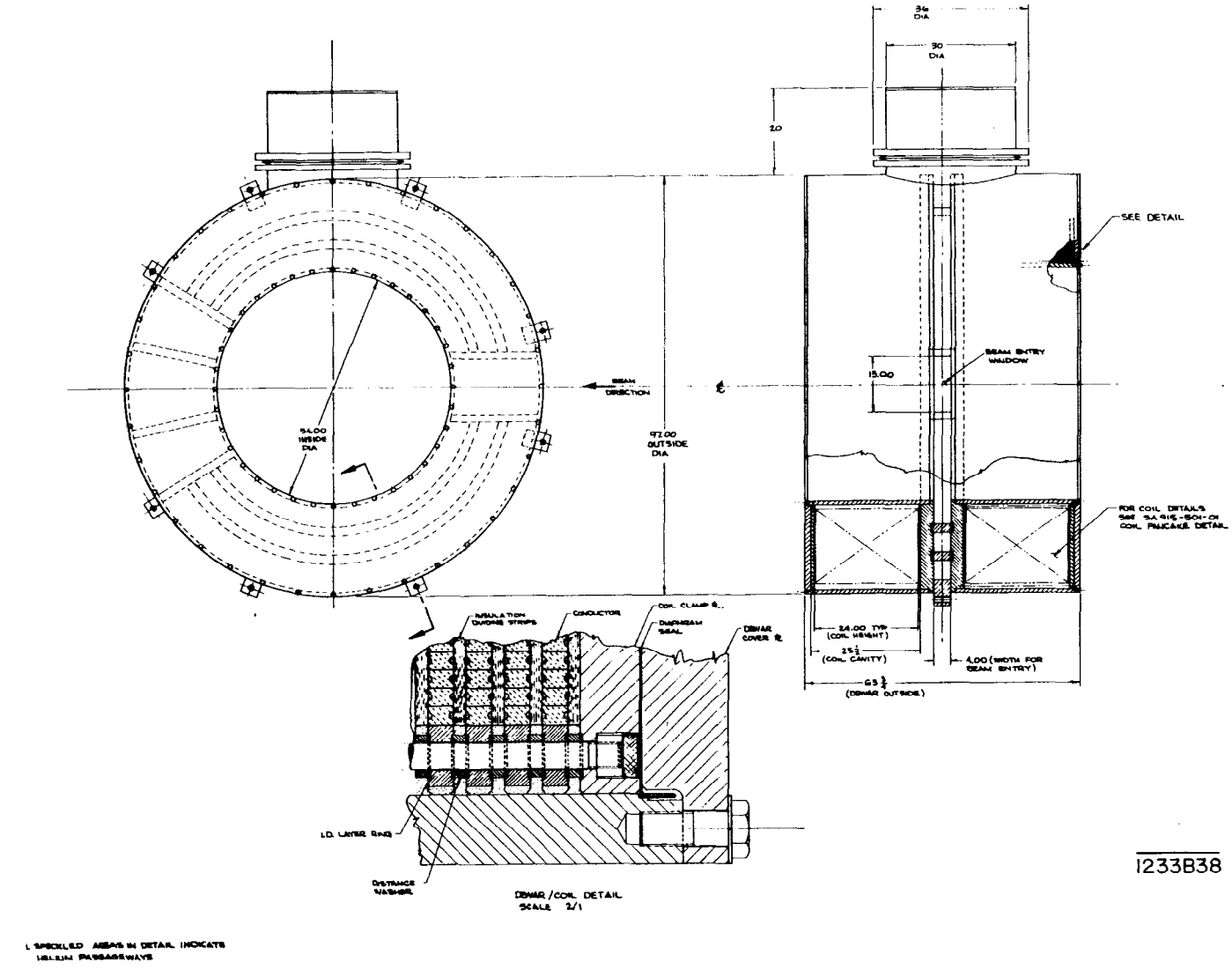

FIG. 3.8--Dewar/coil assembly.

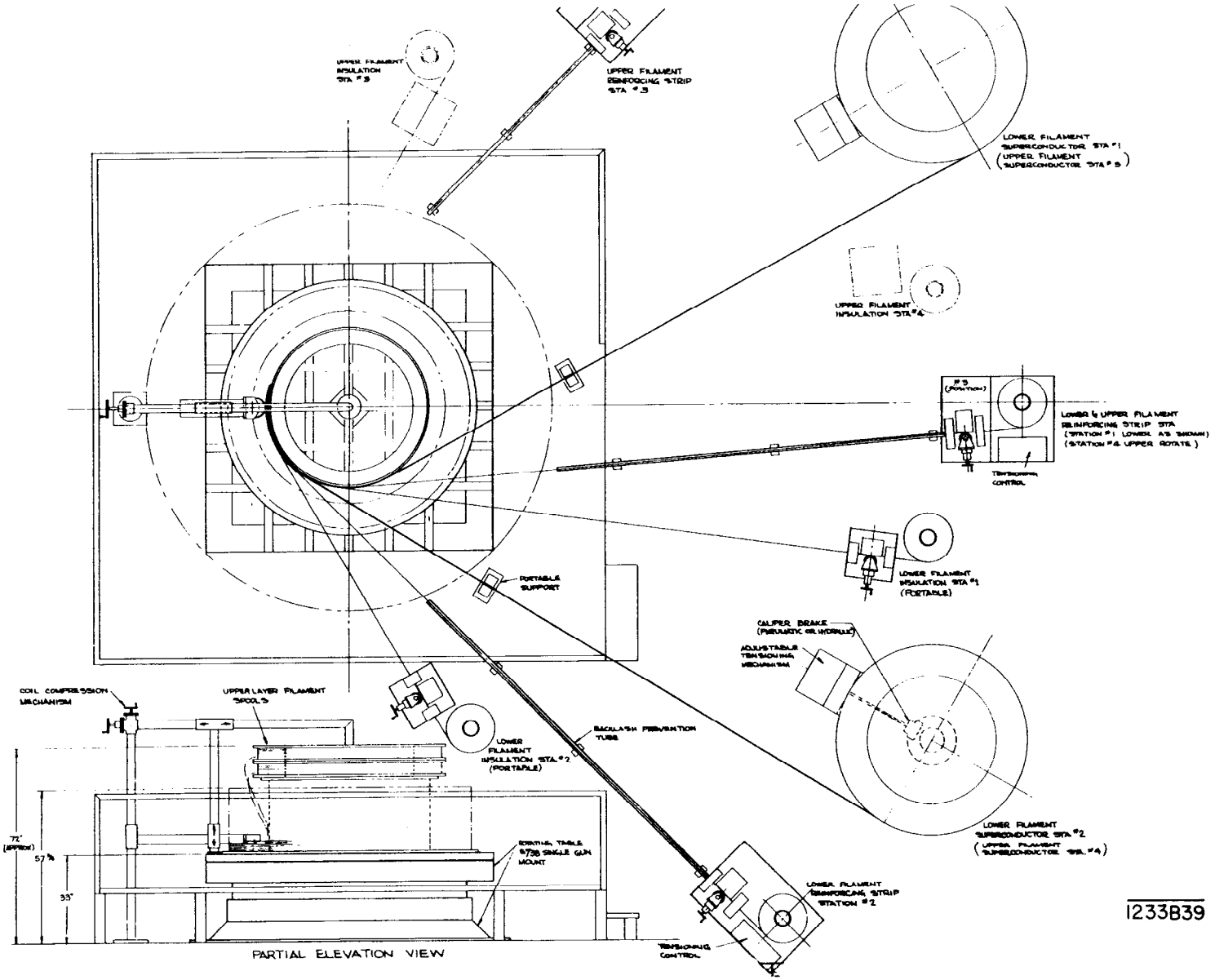

FIG. 3.9--Coil winding equipment layout.

IV. VACUUM TANK

A. Design Parameters

The design pressure of the vacuum tank is 100 psi when installed in the iron core. Supports for the chamber and coil assembly are designed to carry all loads as directly as possible by the iron core rather than by the flexible sections of the vacuum tank.

The vacuum tank is produced in two halves (see Figs. 1.1 and 1.2). Each half has a cylindrical section 110" in diameter which fits into the octagonal cavity of its magnet half. The portion of the vacuum seal which is inside the magnet core requires no bolting as it is supported on both sides by machined iron surfaces. A large beam exit window is provided.

The vacuum tank will be made from 304 stainless steel.

B. Vacuum System

As the volume of the new vacuum tank will be increased by a factor of about 2 and as the plumbing will increase, an additional pumping station is necessary. The vacuum components in current use on the chamber have proved to be very reliable under all operating conditions.

V. COIL DEWAR ASSEMBLY AND SUPPORTS

A. Assembly

Figure 3.7 shows the coil-dewar assembly, consisting of both coils installed within the helium dewar.

The dewar section between the coils carries the 14×10^6 lb axial compressive force. The 3" thick plates are required to carry the coil forces over the 13" unsupported beam entrance and exit regions.

The OD and ID cylindrical dewar sections are welded to the dewar center section. A 28" ID flanged opening is then provided at the top of this weldment for helium and electrical access.

The two coils are then installed into the dewar weldment and sealed within it by the end plate and weld lip arrangement indicated.

The coil-dewar assembly is then installed in the magnet core movable optics half, as described in Section B below.

After installation of the coil-dewar assembly into the magnet (and hence within the vacuum tank optics half), the final conductor and helium line connections are made before lowering the dewar feedthrough lid into place and making the various lip weld joints.

Although not shown, the superconductor leads and splices must be well supported within the dewar.

B. Supports for the Assembly

The support system serves to locate and support the dewar in the movable half of the magnet iron. This system must be capable of supporting the weight of the dewar in addition to axial and possibly radial magnetic forces. While the weight of the dewar (25,000 lb) and the axial force towards the expansion end (3.3×10^5 lb)

can be determined, the direction and magnitude of the radial force between the theoretically concentric dewar and magnet iron depends on the final actual eccentricity between these components, and is, therefore, difficult to estimate. However, it has been determined that if the eccentricity does not exceed 1/8 inch, the radial force, which tends to center the dewar, will not exceed 2×10^5 lb.

To minimize relative radial movements between the chamber, dewar and vacuum tank during cooldown, all supports are located and behave symmetrically about the chamber axis.

The support system consists of a large washer-shaped support ring (the "meat grinder")of Fig.1.2, the outside rim of which is mounted rigidly to the dewar, while the inside diameter locates on a hub inside the vacuum tank; see Fig. 1.4. Since the differential thermal shrinkage between the outside and the inside diameters would create an intolerably high heat transfer rate into the dewar, most of the material between the outside and inside rim has been removed, leaving spokes which are tangential to the inner rim. Differential radial shrinkage will then only result in rotation of the inside rim and raise relatively small bending stresses in the spokes. Eight tie rods complete the support system. These rods hold the axis of the dewar horizontal while the support washer carries all the radial loads.

The dewar will be made from 316L stainless steel. A 286 alloy will be used for the support washer and tie rods to minimize cross sections and hence heat transfer.

VI. REFRIGERATION

A. Introduction

The refrigeration system proposed in this section must serve the following purposes: it must provide the necessary refrigeration for the bubble chamber and it must furnish liquid helium for the coil baths. Thus several separate conditions must be satisfied by the refrigeration system. It must cool the chamber and coils to the correct operating temperature, it must provide the refrigeration necessary to condense the cryogenic fluids for filling the chamber and magnet, and it must remove the static and dynamic heat loads which arise during operation while maintaining the relevant temperatures within the specified limits ($\pm$ 0.05 ^{o}K).

The cooling system for the present chamber is currently being modified to include a hydrogen refrigerator. It could be used to cool the chamber as is, or with minor modifications, supplied with a helium cooled condenser for the hydrogen being used in the chamber cooling loops.

For the purpose of this proposal we assume the latter solution based upon the natural development of helium refrigerators and more important, by our knowledge of the thermodynamic behaviors of the existing 40" chamber.

The helium refrigerator must therefore serve three purposes: it must simultaneously cool the radiation shields at 80^{o}K, furnish the refrigeration for condensation at 25^{o}K of the hydrogen — and produce the liquid helium at 4.3^{o}K being used in the coil dewars.

Reliability is naturally of importance, particularly at 4.3^{o}K, since the magnet is wholly dependent on the presence of liquid helium for stable operation. A single engine Claude cycle with one or more Joule-Thomson stages and with liquid nitrogen precooling is now favored to furnish the necessary cooling at 4.3^{o}K,

25°K and 80°K under all conditions. Although liquid nitrogen baths are not essential for this particular cycle, there are some useful advantages in using precooling: the mass flows are reduced, the cooldown rate from 300° to 80° is essentially independent of the cold end performance of the refrigerator, and the main heat exchanger is of simpler construction.

In addition, a liquid helium storage reservoir, external to the refrigerator, is foreseen, to provide the necessary refrigeration for the magnet during the inevitable periods of power failure, compressor and/or expander trouble, and filling of the magnet dewars during non-pulsing and other standby periods. Similarly, existing 2000 liter liquid hydrogen trailer vessels are foreseen to provide refrigeration for the chamber in periods of refrigerator troubles.

B. Refrigeration Capacity Requirements

Refrigeration is required over a range of temperatures at various times. These requirements are summarized here, first for the chamber and second for the magnet.

1. Chamber

(a) Cooldown. The weight of the chamber and its associated hardware is about 5450 kg. The refrigeration required for cooldown from 300°K to 30°K at rates of 2° and 8°K per hour is shown as a function of temperature in Fig. 6.1. The maximum requirements are at room temperature, for which helium gas cooled by liquid nitrogen will be used. Below 80°K the hydrogen refrigerator will provide the chamber refrigeration.

(b) Filling. As there will always be liquid hydrogen available at SLAC, we will continue to use the bulk filling method presently used. The filling load except when using deuterium or neon will never exceed the few watts of cooling required to precool the filling lines.

(c) Static heat load. One of the fringe benefits of a common vacuum tank for the coils and chamber is the low temperature enclosure provided for the chamber. With the exception of the vacuum tank ports, parts of the support ring, and a portion of the back plate and support tube, the chamber is enclosed within 4.3°K walls. The total static load on the chamber is estimated not to exceed 25 watts.

(d) Dynamic heat load. In agreement with other sources, it has been found that 0.4 J/pulse-liter-second (600 watts for this chamber) is a realistic estimate of the dynamic load for a chamber of this volume. However, to be able to continue to pulse the chamber under unfavorable conditions, we are presently building the hydrogen refrigerator for 1200 watts, which should also be adequate for the conversion.

2. Magnet

(a) Cooldown. The total weight of the coil assembly, including radiation shields, is 30,000 kg. The refrigeration required for cooldown rates of 2° and 8°K per hour is shown as a function of temperature in Fig. 6.1. Liquid nitrogen will be the principal coolant to 80°K. However, even at 25°K, the coil has a large thermal capacity (2.3×10^{6} J) and requires about 250 watts to cool at 8°K per hour. This implies that the refrigerator must have an additional rated capacity of 60 watts at 4.3°K to cover the cooldown load.

(b) Filling. The volume of liquid required to immerse the coils and to fill the dewar is approximately 1200 liters. With a maximum liquefaction rate of 75 liters per hour, the refrigerator alone could be used to fill the dewar. However, during the cooldown period of the chamber and magnet, about 25 liters of liquid helium per hour could be produced and stored in the auxiliary reservoir of 2000 liter capacity, for later dewar-filling use. Alternatively, bulk liquid helium could be purchased from one of several commercial sources, the boil-off used to

charge the refrigerator circuits, and the liquid remaining transferred to the cold magnet.

(c) Static heat load at 4.3°K.

Supports (80°K warm ends)	18 watts
Current leads (including instrumentation lines)	60 watts
Transfer line losses	80 watts
Radiation load (80°K radiation shields)	10 watts
Conductor and joint loss (80°K ends)	5 watts
Total	173 watts

(d) Magnet charging load. During the charging and discharging periods, some energy dissipation in the magnet takes place (ac losses). It is estimated that these will not amount to more than 30 watts over a period of five hours.

(e) Maximum load at 4.3°K.

End of cooldown 173 + 60 = 233 watts

(Charging is less: 173 + 30)

To provide adequate spare capacity for liquefaction we specify the refrigerator to provide 300 watts at 4.3°K.

(f) 80°K heat load.

He cooled radiation shields	40 watts
Supports (300°K warm ends)	210 watts
Conductors (current and conduction max.)	525 watts
Total	775 watts

(g) He mass flow.

80°K He load, 775 watt, 80° in - 90° out:	15 g/sec
25°K He load, 1200 watt, 18° in - 24° out:	30 g/sec
4.3°K He load, 300 watt:	30 g/sec
Expander flow ~:	60 g/sec
Total	135 g/sec

C. Helium Refrigeration System

The refrigeration will be based on the Claude cycle, with liquid nitrogen pre-cooling at $80^{\circ}K$. Schematic flow diagrams and the thermodynamic cycles are shown in Figs. 6.2 and 6.3, and details of the system are as follows:

300 Watt, $4.3^{\circ}K$ Claude Cycle Refrigerator
(with simultaneous cooling at $80^{\circ}K$, $25^{\circ}K$ and $4.3^{\circ}K$)

Operating temperature	$4.3^{\circ}K$
High pressure	11 atm
Low pressure	1.10 atm
Mass flow	135 g/sec
Compressor power	400 hp
$80^{\circ}K$ load (equivalent to 170 liters LN_2/hr)	16,300 watts
$25^{\circ}K$ load (maximum)	1,200 watts
$4.3^{\circ}K$ load (maximum)	300 watts

D. Hydrogen Compressor

High pressure	8 atm
Low pressure	1.2 atm
Mass flow	2.9 g/sec
Compressor power	35 hp

E. Temperature and Pressure Control of Chamber

The chamber temperature should be controlled to within about $\pm$ 0.05 $^{\circ}K$ in order to maintain bubble density constant within 0.5 bubble/cm (at an optimum condition of ten 500 μm bubbles per cm). It should be possible to achieve this with the existing temperature control system following normal operational development, plus the possible addition of certain new features.

Pressure control of the system is discussed in Section IX, Expansion System.

In order to improve the pressure control upstream of the chamber fill valve, a 25 liter independently controlled liquid hydrogen, deuterium or neon system has recently been added to the existing chamber.

F. Cryogenic Safety

For safety purposes the following vessels will be permanently installed and connected to the systems with transfer lines for liquid dump.

(a) 2000 liter liquid helium dewar connected to the coil dewar and to the refrigerator (for liquefaction).

(b) 2000 liter existing liquid hydrogen trailer vessel connected to the chamber.

(c) Existing liquid hydrogen cooled storage tank for deuterium or neon. This tank will be connected to the chamber each time the rare gases are being used.

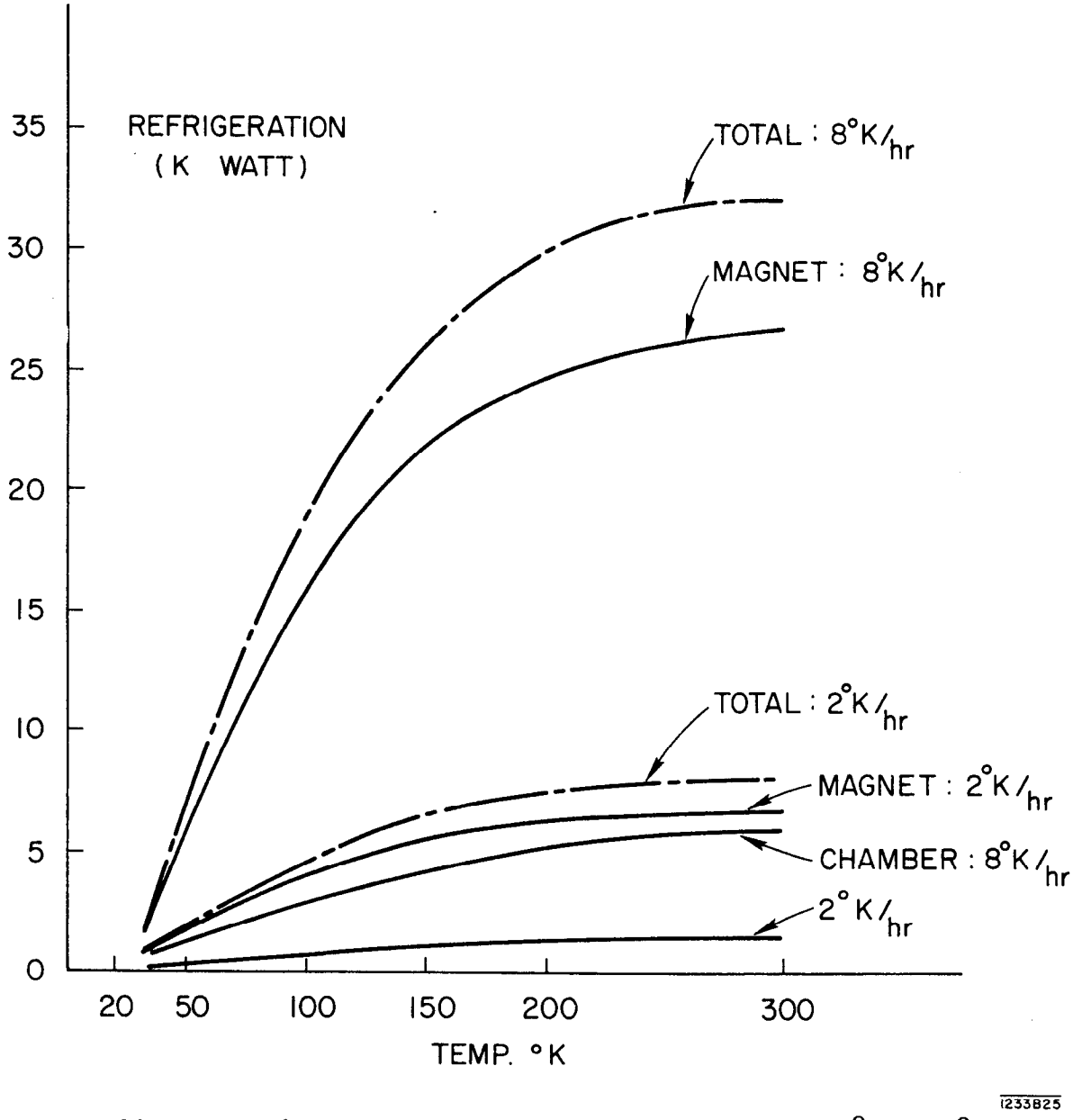

FIG. 6.1--Refrigeration-cooldown requirements from 300°K to 30°K.

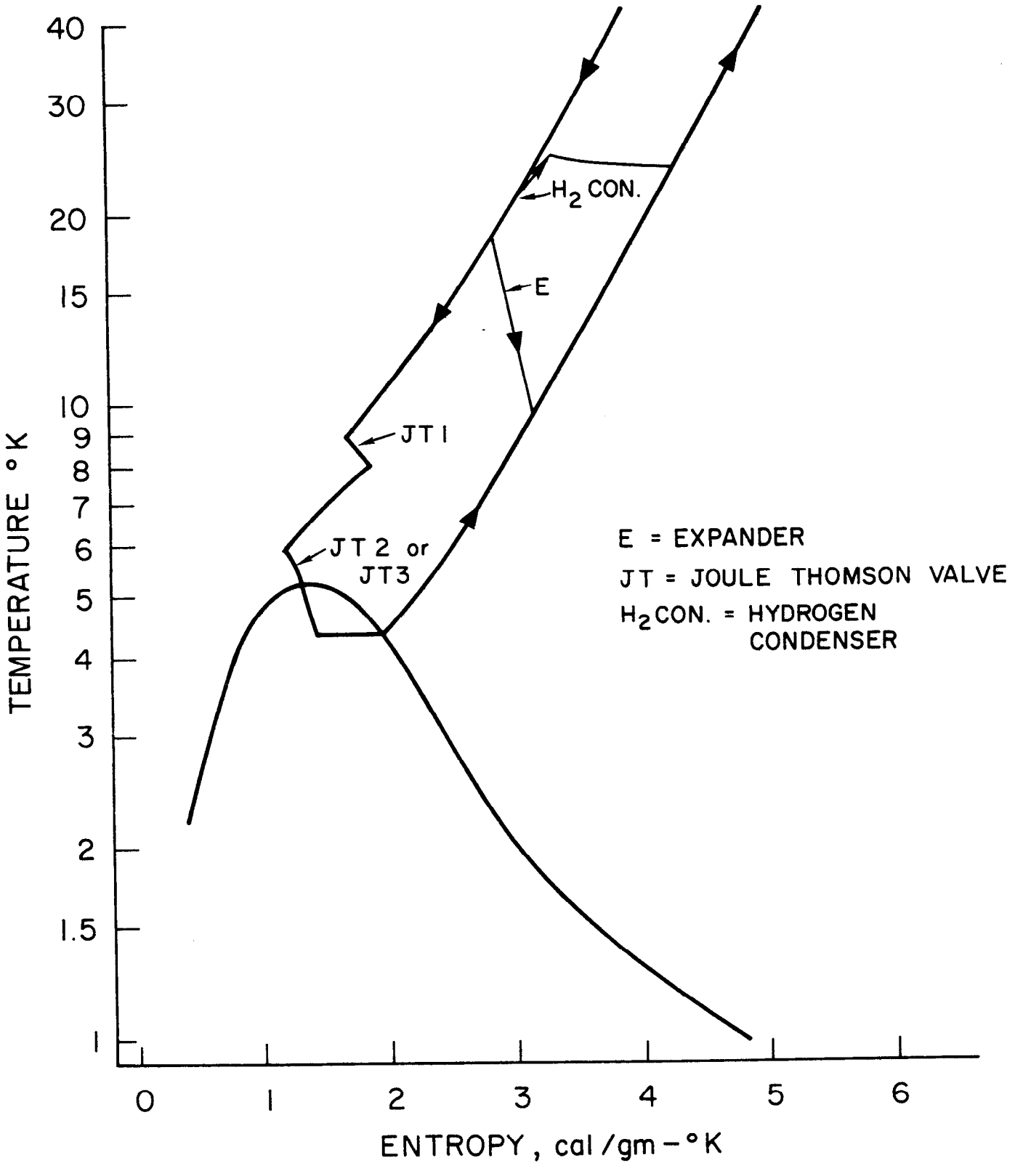

FIG. 6.2--Helium refrigerator cooling cycle.

123324

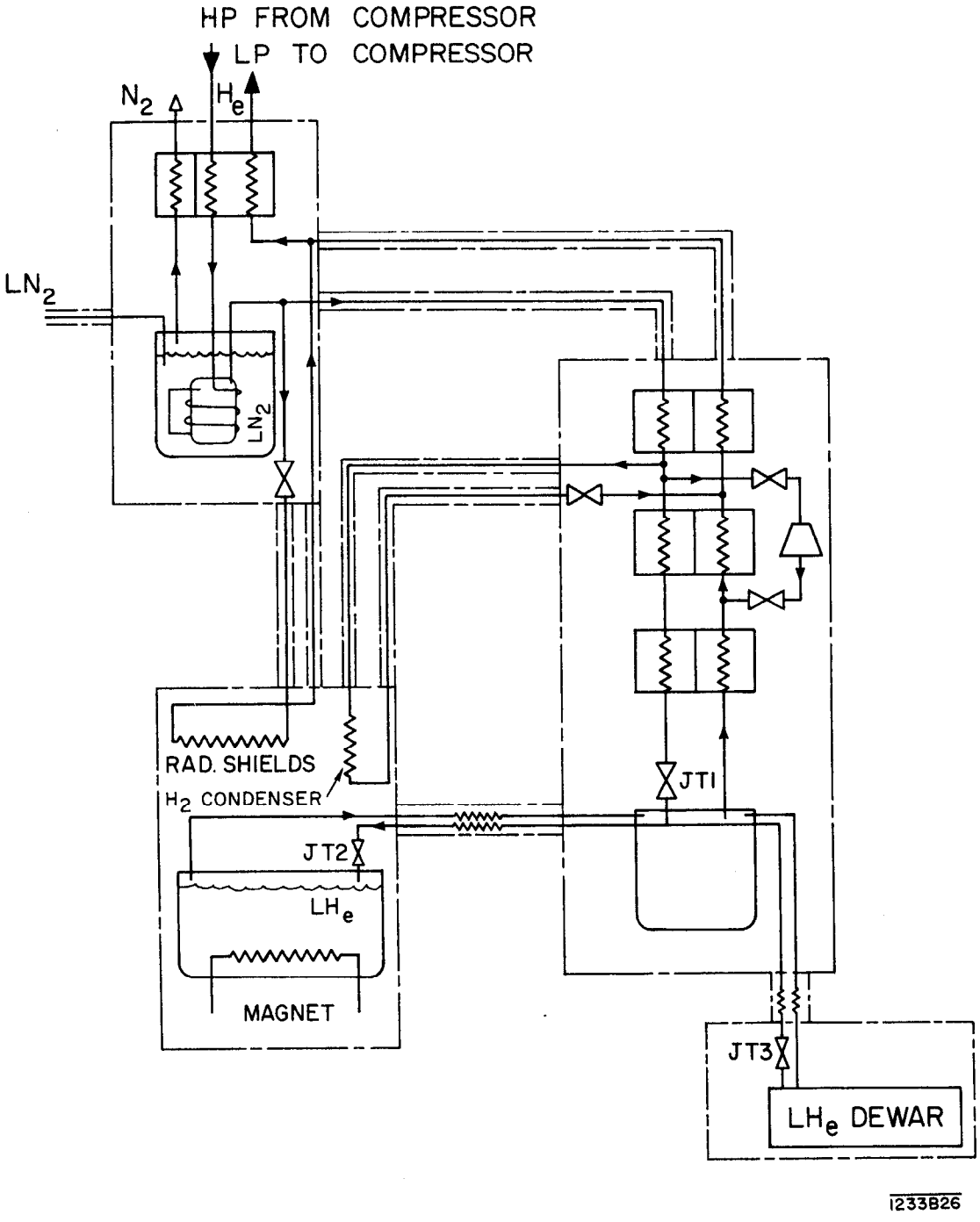

FIG. 6.3--Helium refrigerator flow diagram.

VII. CHAMBER MODIFICATIONS

A. Chamber Body

The existing chamber body, with a 6-5/8" × 28" beam entrance window, will be replaced by a new Kromare 55 alloy body casting having 4" × 13" entrance and 4" × 24" exit windows. The window for the latter will be stainless steel welded directly to the inside of the chamber body. The reduced window width affords a considerable magnet conductor cost saving (> $200,000) and the relatively smooth, projection-free, profile helps to provide the 3" annular space for particle detectors (Fig. 7.1).

The existing metal piston will be replaced by one of fiberglass-epoxy composition (Fig. 7.1). Although a metal omega bellows is shown in the drawings, a fiberglass-epoxy design may be used, based upon investigations being made at Rutherford Laboratory.

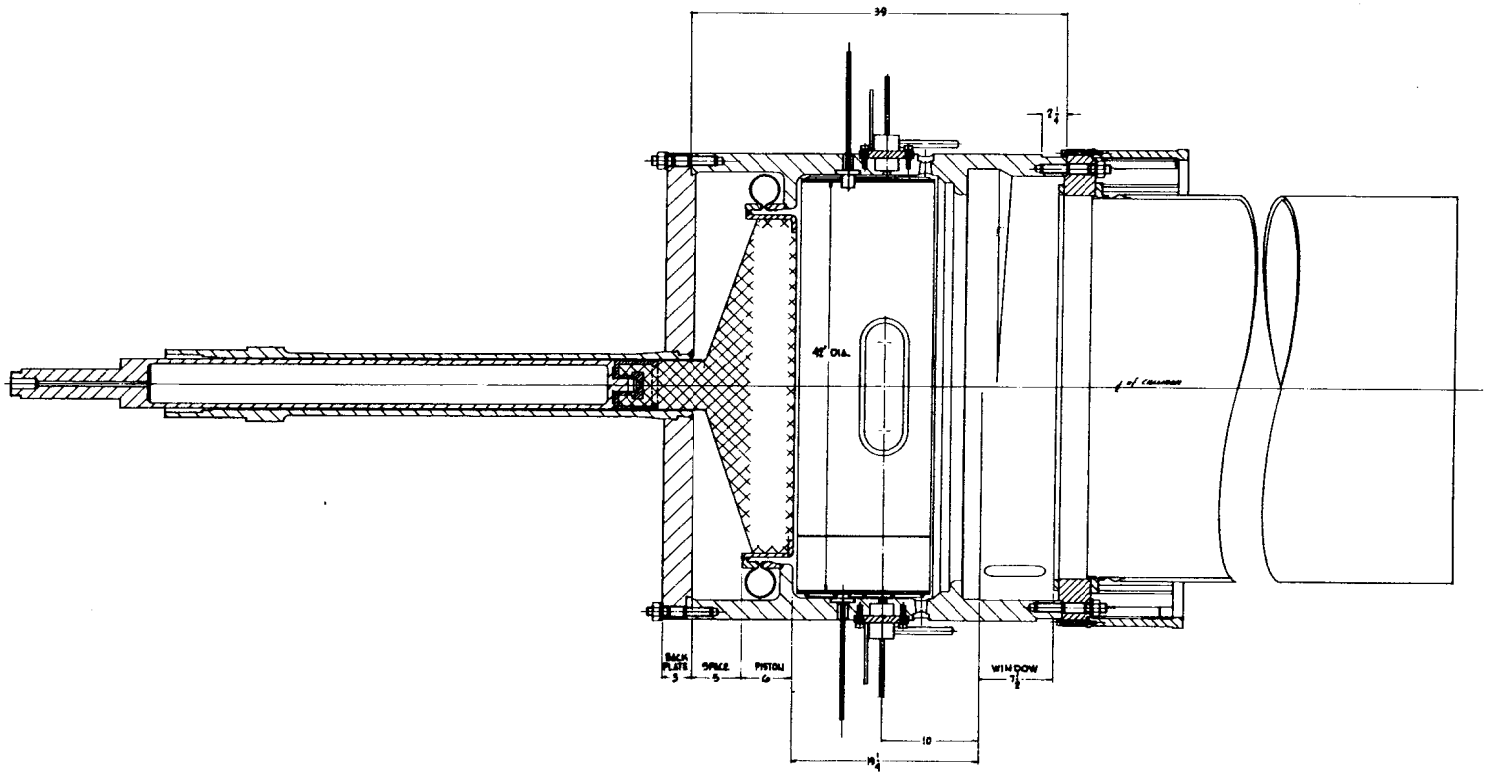

1233B46

FIG. 7.1--Chamber section.

VIII. OPTICS

A. Precision Optics

In order to be consistent with the mass resolution calculations of Section II ($\Delta m = \pm$ 1-2 MeV for 4-c events), the optics must limit the measurement error, $\epsilon \leqslant 50$ microns.

In this section we give what is essentially a set of specifications which, if met, will achieve this goal or better. The primary effort will be to tie together the chamber, glass, magnet and lens positions with maximum precision.

The basic camera will not be modified as part of this proposal. Thus the stereo angle and film format will be unchanged from the present 40" HBC design.

1. Philosophy

All optically relevant parameters will be measured with maximum precision relative to the camera mounting plate. The mounting plate in turn will be aligned parallel to the fiducial plane which is located on the hydrogen side of the main optics window. The position of the plate relative to the magnet iron (hence the field) will also be measured.

2. Goals

We expect to provide the following in the optical system:

(a) Camera mounting plate adjusted parallel to window fiducial (X, Y) plane (under operating conditions) to 1.5×10^{-4} rad.

(b) Distance (Z) between window fiducial plane and camera mounting plate to ± 50 microns (in operating position).

(c) Distance (Z) between first nodal point of lens and camera mounting plate to ± 100 microns.

(d) Distance (Z) between film plane and camera mounting plate to ± 50 microns.

(e) Warm mapping (X, Y) of window fiducials to within ± 12 microns.

(f) Warm mapping (X, Y, Z) of relative position of fiducials on opposite sides of glass to ± 25 microns.

(g) Distance (Z) between pairs of chamber body fiducials to ± 12 microns.

(h) Distance (Z) between chamber body fiducials and window fiducials to ± 50 microns.

(i) Distance (X, Y) between minimum of four window fiducials (cold) to ± 25 microns.

(j) Distance (X, Y) between chamber body fiducials, window fiducials and possibly vacuum side window fiducials (cold) to ± 25 microns.

(k) Lens bore axis relative to camera mounting plate to ± 25 microns.

(l) Magnet iron relative to camera mounting plate to ± 25 microns.

Under cold conditions we will thus know the relative three dimensional position of fiducials to ± 25 microns (except Z between chamber and body fiducials to ± 50 microns) and their distance to film plane to ± 75 microns).

B. Specific Modifications

1. Camera Mounting Plate

This is a 4" thick stress relieved steel plate used to provide stability to the camera. The plate shall be mounted so it can pivot about two perpendicular axes and be locked in position. Thus after the chamber is cold, at operating pressure, and with window gasket inflated, the plate can be adjusted and locked parallel to the window fiducial plane by autocollimation or similar technique. The plate will be checked for flatness and provided with telescope mounts, tooling holes, etc., so the position of fiducials, etc., can be quickly surveyed relative to it. Such mounts will be provided at each of the seven vacuum tank points.

2. Magnet Fiducials

Fiducials will be provided on the magnet iron, so that using a telescope on the camera mounting plate the position of the plate (and hence fiducial volume) relative to the magnet can be easily determined. One or more Hall probes may be provided at the magnet fiducials to verify stability of the magnetic field.

3. Special Surveying Tools

An autocollimator or similar device and a telescope with X, Y measuring capability will be obtained and provided with special mounts for rapid resurveying of fiducials, etc., relative to camera mounting plate.

4. Determination of Fiducial to Camera Distance

A permanently mounted invar depth stick or similar device will be provided in the vacuum tank to physically measure fiducial plane to camera mounting plate separation. It will penetrate the vacuum chamber wall through a bellows seal and can be brought in contact, at known pressure, with the vacuum side of the glass. The distance from the end of stick to the surface of the mounting plate will be measured with a micrometer.

5. Lens Axis Location

Lenses are located in closely fitting bores in a 0.5" aluminum plate (lens mounting plate) which is clamped (at three points around each lens) exactly parallel to the camera mounting plate. The relative positions of the bores are measured to 12 micron accuracy and could be improved. The lens mounting plate is doweled relative to the camera mounting plate. The position of the lens bores relative to the camera mounting plate will be measured and the position repeatability verified.

6. Film Plane Location

The effective tilt of the film plane is determined by the mounting of a 45^{o} mirror. The effective parallelism of the film plane and camera mounting plate is achieved

by the following procedure: The platen is clamped to a surface plate, a parallel mirror placed on the platen base and an autocollimator aligned perpendicular to it. The parallel mirror is now placed on the platen face and the 45^{o} mirror adjusted for autocollimation to within one minute. The effective film plane is thus adjusted parallel to platen base (and hence lens mounting plate) to within 30 seconds of arc ($\sim 1.5 \times 10^{-4}$ rad). We shall refine this method somewhat, by procurring better tooling, sealing the 45^{o} mirror in position, and most important, checking that the calibration is maintained during run. Parallelism of $.5 \times 10^{-4}$ rad should probably be achieved.

7. Window Fiducials

Window fiducial pattern and size will be revised (see Fig. 8.1). A few vacuum side fiducials will be incorporated, but they will be of paste on or evaporated type. The fiducials will be mapped to ± 12 microns on each side and to ± 25 microns relative separation between the two sides. A minimum of four fiducials will be under the vacuum tank ports for cold survey. The window will be independently photographed with the bubble chamber camera from both sides, to check fiducial reconstruction (effect of glass and lens induced distortions) before mounting in chamber.

8. Chamber Body Fiducials

Three pairs of chamber body fiducials will be provided, each pair consisting of a bar with front fiducial about 2" and back about 15" from the glass. The Z separation between the fiducials in each pair will be measured to ± 12 microns. The bars will be mounted on stiff flextures to chamber walls free to move in Z. In operation they will be pressed to the chamber window by a helium bellows, bi-metallic strip or similar device. Thus the Z distance between the body fiducials

and window fiducials will be known to ± 25 microns. The position of the body fiducials will be such that they can be surveyed, cold, from the camera mounting plate.

C. Camera Pneumatic Conversion

The existing camera operates in a magnetic field of 50 mT and this is expected to rise to 300 mT or more in the proposed conversion.

The camera is basically of nonmagnetic construction. The only modification required for this high field operation will involve replacement of existing electromagnetic valves, clutches and brakes, as well as the drive motor, by air-operated units.

Only commercial components or those of proven design need to be employed. Thus, this conversion will be a straightforward project.

No problem with databoard lights is anticipated, but the CRT display will be removed. Preliminary flash tube tests at Argonne in fields up to 2 T have revealed no problems.

D. Tempered Optical

The 8^{o}K/hr. cooldown rate discussed above is based upon replacement of the existing glass by one which is tempered. The existing spare window is being retempered and polished. The new fiducial pattern per para B6 above will be applied to it.

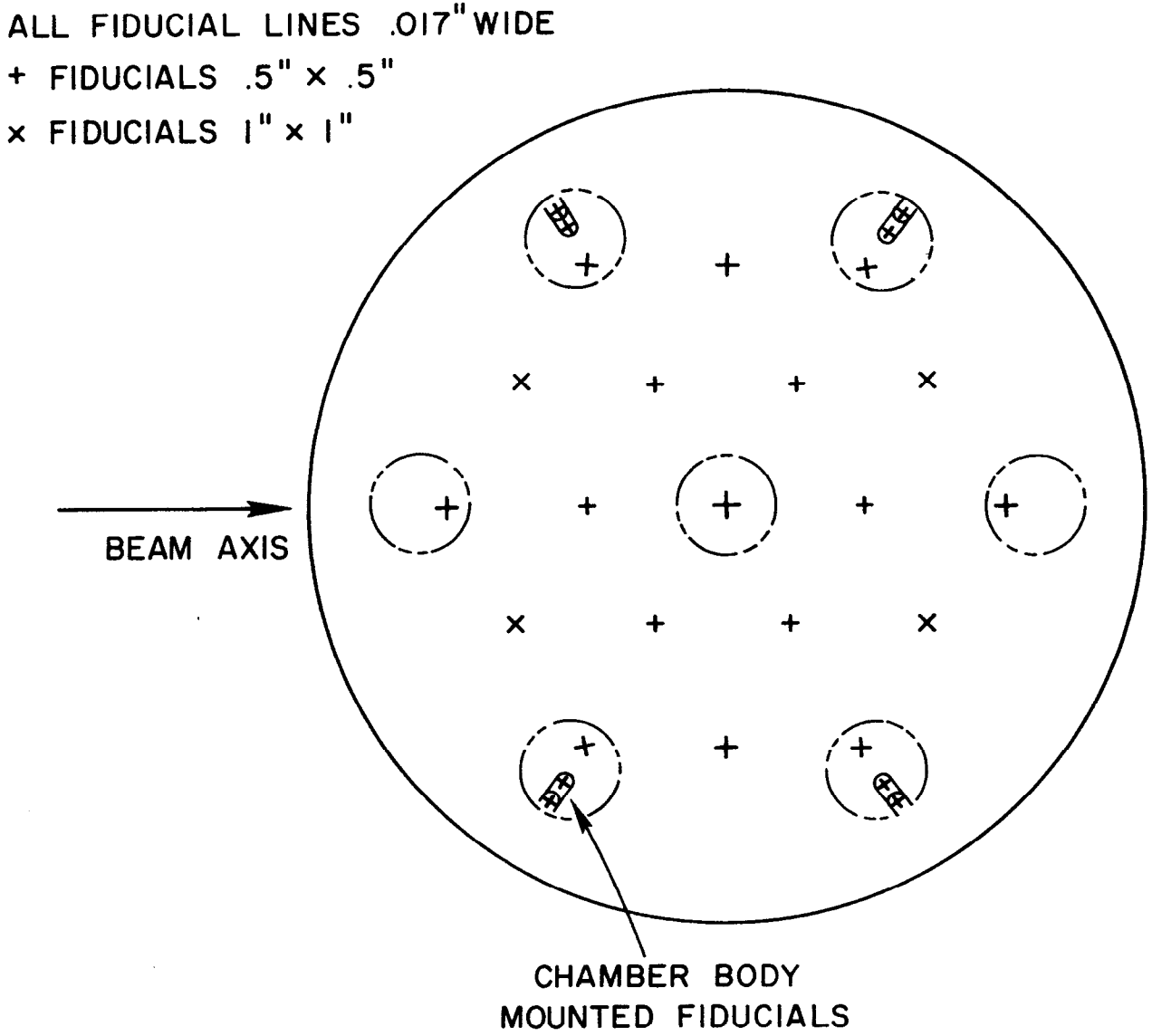

FIG. 8.1--Fiducial locations.

IX. EXPANSION SYSTEM

Three cycles per second is the target expansion rate for the proposed chamber. It is hoped that this can be achieved by normal operational development of the existing system including a larger and more extensively cooled hydraulic pump, aided by the introduction of a fiberglass piston, (Fig. 7.1).

In order to maintain chamber pressure within ± 0.1 psi, it will be necessary to develop a feedback system (electronic or hydraulic) for accurate position control of the piston. In addition, it will probably be necessary to insure that no gas volume exists at the top of the expansion bellows.

Due to the relatively high magnetic fringing field, the fast valves and Ross valves will be relocated about five feet further away from the magnet, which requires a certain amount of redesign.

X. BUDGET, SCHEDULE, AND MANPOWER

A. Schedule

The schedule (Fig. 10.1) is optimistic. The critical path is determined by superconductor procurement, testing, and coil-winding. It assumes procurement money and SLAC manpower is available as required. It is obvious that any stretch out of money or manpower would necessitate a revision of the schedule.

B. Costs

The cost of this program as outlined in Table 10.1 is estimated to be $1,700,000.

The biggest unknown is the cost of the composite superconducting material, and the present estimate, based upon replies from a SLAC inquiry to prospective suppliers and bids for a single length of material is $6.00 per foot.

The estimated costs are based on the current prices of materials and the estimated cost of SLAC shops in FY71. Cost in outside shops would tend to be higher, particularly where heavy machine tools must be used. For example, it has not been established that the vacuum tank or helium dewar can be completely fabricated in house.

The flags on the schedule (Fig. 10.1) represent the required timing of major infusions of money.

The cost figures do not include SLAC engineers, designers, and technicians that are presently assigned to bubble chamber work. The Bubble Chamber Development Group currently has 2 people working on the project. The first year of the project as presently scheduled requires 6 engineers, 4 designers and 2 technicians. The next six months requires 6 engineers, 2 designers and an average of 10 technicians.

The laboratory has a group with cryogenics and superconducting expertise which will support the program.

When the 40" chamber is shut off, the entire 40" crew and much of the bubble chamber shop effort will participate in the conversion.

For this schedule, only incidental effort has been made to smooth the manpower curves. Considerable planning effort will be needed when we know more about rate of money and labor availability to smooth manpower effort and minimize 40" HBC downtime.

Table 10.1

7-T Superconducting Magnet Conversion Costs

Item	Material	Labor	Total cost
1. Magnet Coils			
(a) Conductor			
108,000 feet at $6.00/foot	$648,000		
(b) Coil Fabrication			
Winding equipment	20,000	$17,500	
30 cm ID test magnet conversion, transfer lines	18,000		
Conductor testing & equipment	10,000	11,600	
Pancake winding and coil assembly (20 MC/pancake) × (20 pancakes)	5,000	94,200	
			$824,300
2. Power Supply			
(a) 700 A, 25 V (10^{-3} regulation)	16,000		
Safety circuit	14,000		
Control circuit	10,000	11,500	
(b) Leads	12,000		
(c) Water shunt	8,000		
(d) Vacuum switch	11,000		
			82,500
3. Magnet Iron			
(a) Additional iron (20 tons ASTM A273)	25,000		
(b) Iron modifications (6 man-months)		8,400	
(c) Modify Support System	8,800		
(d) Tie bolts (four)	1,700		
(e) Magnetic Shielding, 57 tons of iron	18,500	25,000	
(f) Platforms, miscellaneous and paint (2 man-months)	900	2,600	
			90,400

Item	Material	Labor	Total cost
4. Vacuum tank			
(a) Materials	$ 23,500		
(b) Fabrication		$53,100	
(c) Stress relief	500	500	
(d) Special tooling, etc. (tests and miscellaneous labor)	1,500	1,600	
			$ 80,700
5. Dewar and Supports			
(a) Materials	48,000		
(b) Fabrication		15,800	
(c) Stress relief	500	500	
(d) Welding		7,500	
(e) Miscellaneous materials and tests	2,500		
			74,800
6. Refrigeration System			
(a) 4.3^{o} K, 300-W helium refrigerator: compressor, intermediate coolers and purifiers, and cold box	230,000		
LN_2 precool system	7,500		
Transfer lines (70')	7,500		
(b) 2000-liter liquid He storage vessel	24,000		
(c) Radiation shields	13,500		
Superinsulation and super-insulating cages	3,500	1,500	
(d) Platforms for cold-box and purifier	1,000	400	
(e) 1000 sq. ft. compressor building	15,000		
(f) Utilities and gas storage	4,000		
(g) Interconnecting piping	1,000	1,100	
(h) Hydrogen compressor	12,000		
(i) Installation (3 man-months)		4,400	
			326,400

Item	Material	Labor	Total cost
7. Chamber Body			
(a) Casting	$ 23,000		
(b) Fabrication		$ 9,400	
(c) Heat exchangers	500		
(d) Plumbing and controls	1,000	2,600	
(e) Back plate and support	4,000	800	
(f) Piston drive shaft	1,500		
(g) Pistons	30,000		
(h) Piston liners (6)	4,200		
(i) Bellows	20,000		
(j) Bellows test fixture		5,000	
(k) Retaining rings (6)	5,900		
(l) Chamber liners (4)	3,700		
(m) Test fixtures, etc.	1,200		
(n) Test program (4 man-months)		5,800	
			$119,500
8. Camera			
(a) Modifications for high field operation	9,000	4,400	
(b) Improvement of optical precision	8,000	4,800	
			26,200
9. Expansion System	6,000	5,900	11,900
10. Magnet Measurement Device	20,000	4,400	24,400
11. Shop labor during assembly		21,100	21,100
		GRAND TOTAL	$1,682,700

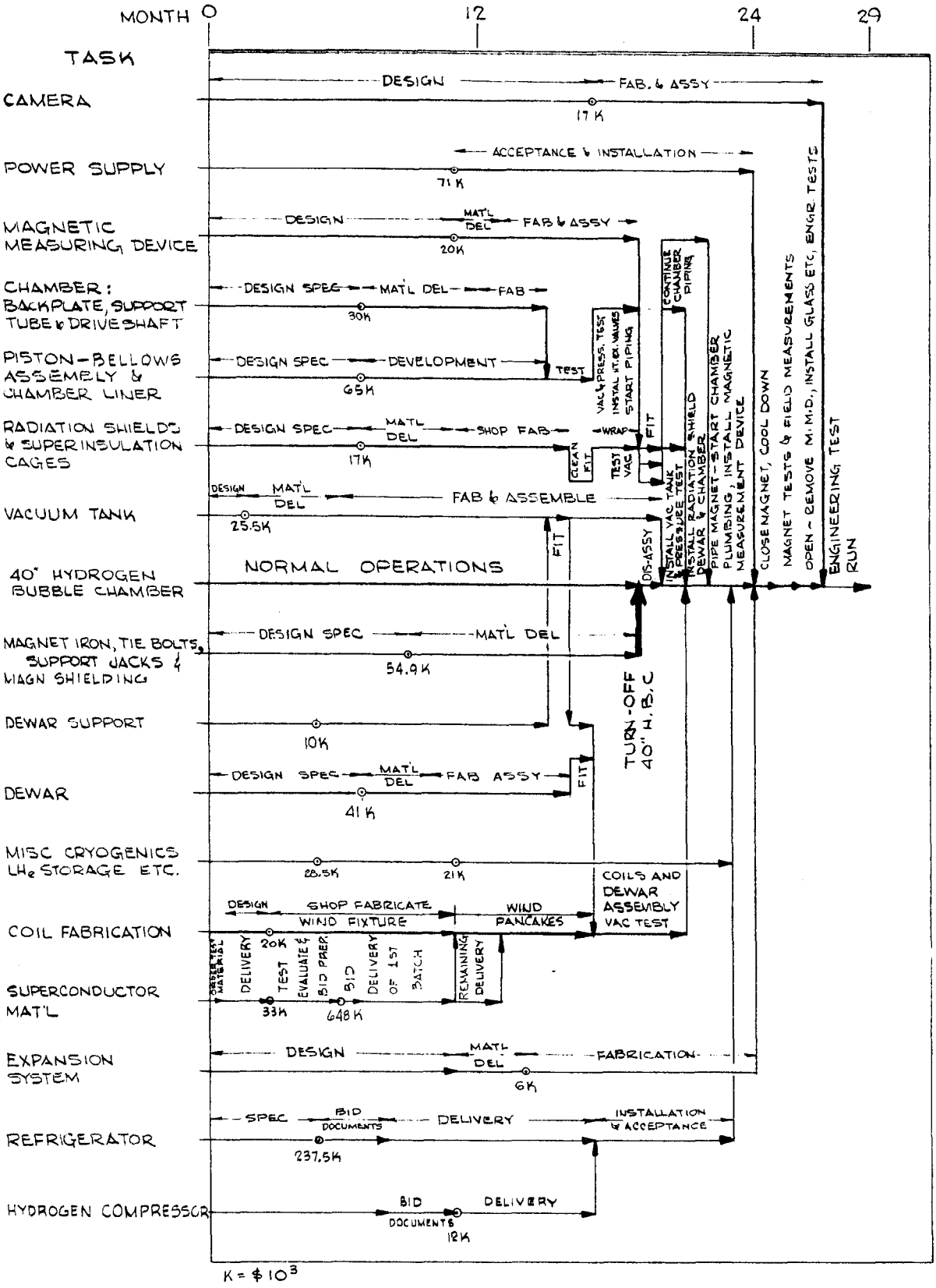

FIG. 10.1--Schedule.